Feedback control and modal structures in transitional shear flows

by

Onofrio Semeraro

February 2011
Technical Reports
Royal Institute of Technology
Department of Mechanics
SE-100 44 Stockholm, Sweden

Akademisk avhandling som med tillstånd av Kungliga Tekniska Högskolan i Stockholm framlägges till offentlig granskning för avläggande av teknologie licentiatsexamen fridag den 18 februari 2011 kl 10.00 i sal E3, Kungliga Tekniska Högskolan, Osquars Backe 14, Stockholm.

Universitetsservice US–AB, Stockholm 2011

Feedback control and modal structures in transitional shear flows

Onofrio Semeraro
Linné Flow Centre, KTH Mechanics, Royal Institute of Technology
SE-100 44 Stockholm, Sweden

Abstract

Two types of shear flows are investigated in this thesis; numerical simulations are performed for the analysis and control of the perturbation arising in a boundary layer over a flat plate, whereas PIV measurements are analysed for the investigation of a confined turbulent jet. Modal structures of the flows are identified: the aim is to understand the flow phenomena and to identify reduced-order models for the feedback control design.

The attenuation of three-dimensional wavepackets of streaks and Tollmien-Schlichting (TS) waves in the boundary layer is obtained using feedback control based on arrays of spatially localized sensors and actuators distributed near the rigid wall. In order to tackle the difficulties arising due to the dimension of the discretized Navier-Stokes operator, a reduced-order model is identified, preserving the dynamics between the inputs and the outputs; to this end, approximate balanced truncation is used. Thus, control theory tools can be easily handled using the low-order model. We demonstrate that the energy growth of both TS wavepackets and streak-packets is substantially and efficiently mitigated, using relatively few sensors and actuators. The robustness of the controller is investigated by varying the number of actuators and sensors, the Reynolds number and the pressure gradient. The configuration can be possibly reproduced in experiments, due to the localization of sensing and actuation devices.

A complete analysis of a confined turbulent jet is carried out using time-resolved PIV measurements. Proper orthogonal decomposition (POD) modes and Koopman modes are computed and analysed for understanding the main features of the flow. The frequencies related to the dominating mechanisms are identified; the most energetic structures show temporal periodicity.

Descriptors: Flow control, flat-plate boundary layer, laminar-turbulent transition, model reduction, balanced truncation, Koopman modes, POD modes, turbulent co-flowing jet

Preface

This thesis deals with feedback control via model reduction in flows over flat-plate boundary layers and flow analysis using global modes. A brief introduction on the basic concepts and methods is presented in the first part. The second part contains three articles. The papers are adjusted to comply with the present thesis format for consistency, but their contents have not been altered as compared with their original counterparts.

Paper 1. O. Semeraro, S. Bagheri, L. Brandt & D. S. Henningson, 2010
Feedback control of three-dimensional optimal disturbances using reduced-order models. Under revision - Journal of Fluid Mechanics

Paper 2. O. Semeraro, S. Bagheri, L. Brandt & D. S. Henningson, 2010
Transition delay in boundary layer flow using feedback control. To be submitted - Journal of Fluid Mechanics

Paper 3. O. Semeraro, G. Bellani & F. Lundell, 2011
Analysis of time-resolved PIV measurements of a confined co-flowing jet using POD and Koopman modes. Internal Report

Division of work among authors

The main advisor for the project is Prof. Dan S. Henningson (DH). Dr. Luca Brandt (LB) has acted as co-advisor.

Paper 1

The code development and the set-up of flow configurations were done by Onofrio Semeraro (OS) in collaboration with Shervin Bagheri (SB) and LB. Numerical simulations were performed by OS. The paper was written by OS with the help of SB and LB. The introduction and the feedback control theory section were written by SB. DH provided comments on the article.

Paper 2

The development of the code, the simulations and the analysis of the results were performed by OS. The paper was written by OS in collaboration with LB. SB and DH provided suggestions on the work and comments on the manuscript.

Paper 3

The experimental setup was performed by Gabriele Bellani (GB). Dynamic modal decomposition (DMD) and proper orthogonal decomposition (POD) were performed by OS; the analysis of the results was performed by GB and OS in close collaboration. The paper was written by OS and GB. Fredrik Lundell provided comments on the manuscript.

Contents

Abstract iii

Preface iv

Part I 1

Chapter 1. Introduction 3

Chapter 2. Governing equations 6
- 2.1. Navier-Stokes equations and linearization 6
- 2.2. Introducing inputs and outputs 7

Chapter 3. A portrait of the flows: linear and nonlinear decompositions 10
- 3.1. Proper orthogonal decomposition 10
- 3.2. Koopman modes and dynamic mode decomposition 13

Chapter 4. Model reduction and flow control 18
- 4.1. Model reduction using balanced truncation 18
- 4.2. Feedback control design 22
- 4.3. Towards laminar-turbulent transition delay 25

Chapter 5. Summary of the papers 27
- Paper 1 27
- Paper 2 27
- Paper 3 28

Chapter 6. Conclusions and outlook 29

Acknowledgments 31

Bibliography 32

Part II 35

Paper 1. Feedback control of three-dimensional optimal disturbances using reduced-order models 37

Paper 2. Transition delay in boundary layer flow using feedback control 89

Paper 3. Analysis of time-resolved PIV measurements of a confined co-flowing jet using POD and Koopman modes 107

Part I

Introduction

CHAPTER 1

Introduction

Control of wall-bounded transitional flows might lead to high potential benefits and outcomes, e.g. a reduction of fuel consumption. As reported by Kim & Bewley (2007), ocean shipping consumes about 2.1 billion barrels of oil per year, whereas the airline industry consumes about 1.5 billion barrels of jet fuel per year. Thus, any reduction of aerodynamic drag can positively influence the operational cost of cargo ships or commercial aircraft. In recent years, research efforts have been devoted to the manipulation of fluids, using both passive and active means; passive control can be implemented – for instance – using riblets (Choi *et al.* 1993) or discrete roughness elements (White & Saric 2000). Examples for active control are given by active wave cancellation (Sturzebecher & Nitsche 2003), opposition control (Hammond *et al.* 1998), wall-motion techniques (Quadrio & Ricco 2004) or by linear and nonlinear control theoretical approaches, using spatially localized convolution kernels (Högberg *et al.* 2003) or adjoint-based optimization methods (Bewley *et al.* 2001).

In this thesis, feedback control is applied using localized sensors and actuators for the mitigation of the perturbations arising in a boundary layer spatially evolving on a flat plate. The configuration is fully three dimensional (3D) and resembles experimental setups – see for instance Lundell (2007). The main aim of our investigation is the delay of transition from laminar to turbulent flow. Indeed, it is well established that under certain conditions the initial phase of the laminar-turbulent transition in wall-bounded flows is largely governed by linear mechanisms (Schmid & Henningson 2001). Thus, the tools of linear control theory may provide efficient, robust and feasible controllers to delay transition to turbulence.

Transition from laminar to turbulent flow can be promoted by the growth of Tollmien-Schlichting (TS) wavepackets; this scenario - often referred to as classical transition - is usually observed in clean environments characterized by low levels of free stream turbulence (smaller than 1%). In figure 1.1, the linear propagation of a localized Tollmien-Schlichting wavepacket is depicted. Iso-contours of the streamwise velocity component of the disturbance are visualized at three different instances in time, viewed from above. The direction of the propagation is from left to right; the perturbation grows in size along the streamwise-direction and spreads in the spanwise direction, as it propagates. The structure is 3D, as it can be observed by the bending of the perturbation along the spanwise direction. In the right panels, the effects of the controller

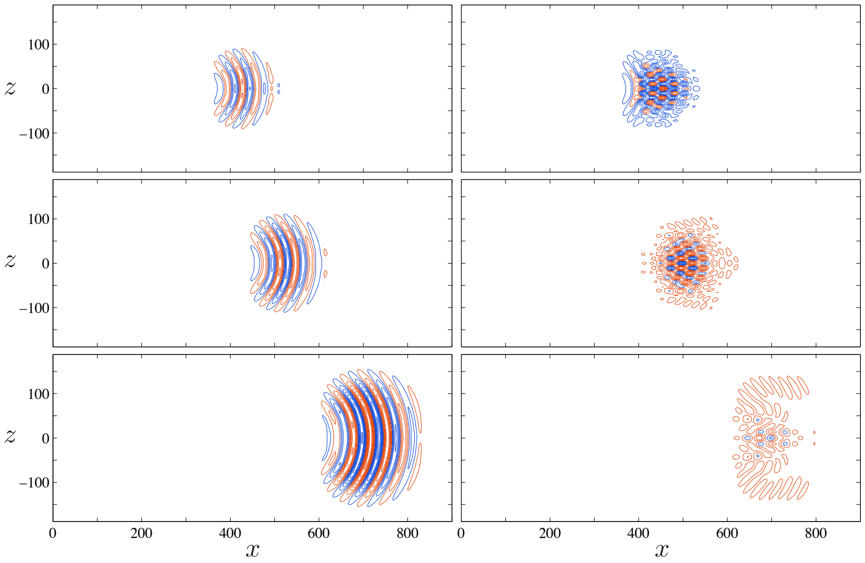

FIGURE 1.1. Evolution of a TS wavepacket at three instants of time, without control (left column) and with control (right column). The iso-contours of the streamwise component are shown in the xz-plane; the same iso-levels are used: red isolines indicate positive velocity, while the negative one is indicated with blue.

are shown. The original structure is distorted into a more complicated three-dimensional pattern, where traces of the localized actuation are recognizable. When the perturbation is further convected downstream, a significant damping of the energy is observed; indeed, the contour levels are barely visible, while the perturbation for the uncontrolled case attains its maximum energy. When finite-amplitude disturbances are considered, such a drastic energy reduction results in a delay of the initial stages of the transition process.

The long-term aim of this research project is to develop numerically reliable and fast controllers that are suitable for the use in laboratory experiments. From this point of view, numerical investigations can be useful for wind-tunnel experiments and provide guidelines for the spatial distribution and shape of the actuators and sensors.

These investigations, however, pose a significant challenge for the systems under analysis. Indeed, the complexity of the flows leads to large systems. For instance, the flat plate case involves about $n \approx 10^7$ degrees of freedom; the control theory tools cannot easily be applied in this case. An alternative is provided by *model reduction*: a low-order model is computed, capturing the essential dynamics of the flow, and used for the control design. This strategy allows to easily apply standard tools of control theory and design a fast controller running on-line simultaneously with the main simulation. Moreover, the analysis of modal structures of the flow provides valuable information. For instance, the algorithm used in this thesis for the model reduction of the system makes use of a basis consisting of *balanced modes*; the information given by the spatial support of these modes can be used for actuator/sensor placement. Thus, the analysis of a complex flow can take advantage of modal decompositions.

A second shear flow is analysed in this thesis; proper orthogonal decomposition (POD) and Koopman modes are computed using PIV measurements of a turbulent confined jet with co-flow. POD is a common method for extracting coherent spatial structures from a flow, ranked according to the energy content; the temporal counterpart is provided by the temporal coefficients associated to the spatial structures. However, the most energetic structures of a flow are not necessarily the most relevant for the flow analysis; the Koopman modes method is a novel technique providing an alternative way for analysing the flow. Both techniques are employed and compared to classical spectral analysis.

The first part of the thesis is organized as follows. In chapter 2, the governing equation of the flow are introduced. Inputs and outputs are introduced in the system and briefly described. The modal decompositions used for the flow analysis are summarized in chapter 3; as an example, the analysis of a confined turbulent jet is used. Control design and model reduction for the boundary layer flows are described in chapter 4. Finally, the first part of the thesis finalizes with a short summary of the papers (chapter 5) and the outlook in the conclusive chapter 6.

CHAPTER 2

Governing equations

In this chapter the equations used to describe the flow are introduced. In section 2.1, the incompressible Navier-Stokes equations and the linearized Navier-Stokes are briefly described. The design of the linear control requires the introduction of inputs and outputs in the system (section 2.2); the setup described here, combined with a low-order model of the system and a linear quadratic controller (LQG), allows to mitigate the perturbation as shown in figure 1.1.

2.1. Navier-Stokes equations and linearization

The Navier-Stokes equations governing the viscous, incompressible flow are given by

$$\frac{\partial \mathbf{u}}{\partial t} = -\mathbf{u} \cdot \nabla \mathbf{u} - \nabla p + \frac{1}{Re} \Delta \mathbf{u} \tag{2.1a}$$

$$0 = \nabla \cdot \mathbf{u} \tag{2.1b}$$

The velocity field $\mathbf{u}(\mathbf{x}, t) = (u, v, w)^T$ is a solution of the equation and $p(\mathbf{x}, t)$ indicates the pressure field, both depending on space $\mathbf{x} = (x, y, z)^T$ and on time $t \in [0, T_f]$; the differential operators appearing in the equations are the gradient, defined as $\nabla = (\partial/\partial x, \partial/\partial y, \partial/\partial z)$, and the laplacian $\Delta = \left(\partial^2/\partial x^2, \partial^2/\partial y^2, \partial^2/\partial z^2\right)$. The equations are written in non-dimensional form; the velocity is normalized by the reference velocity U_∞, the pressure by the dynamic pressure and the lengths by the displacement thickness at the inflow position, hereafter indicated with δ_0^*. Thus, the Reynolds number is defined as

$$Re = \frac{U_\infty \delta_0^*}{\nu}, \tag{2.2}$$

where ν is the kinematic viscosity. A second definition of the Reynolds number used in this thesis is based on the distance from the leading edge, x

$$Re_x = \frac{U_\infty x}{\nu}. \tag{2.3}$$

The solution of this set of non-linear partial differential equations is provided by numerical simulations and is dependent on the initial condition $\mathbf{u}_0 = \mathbf{u}(\mathbf{x}, 0)$ and the imposed boundary conditions; no-slip conditions are imposed on the wall, whereas in the far field Neumann conditions or Dirichlet conditions can be imposed. More details on the numerical procedure are included in Chevalier *et al.* (2007), where the fully spectral code used for this work is introduced.

Both direct numerical simulations (DNS) and large eddy simulations (LES) were performed.

Stability analysis and control design are based on the characterization of the small-amplitude perturbations evolution; to this end, the decomposition

$$\mathbf{u}(\mathbf{x},t) = \mathbf{U}(\mathbf{x}) + \varepsilon\tilde{\mathbf{u}}(\mathbf{x},t) \tag{2.4a}$$

$$p(\mathbf{x},t) = P(\mathbf{x}) + \varepsilon\tilde{p}(\mathbf{x},t) \tag{2.4b}$$

is inserted in the (2.1). P is the mean pressure and $\tilde{p}$ the pressure perturbation, whereas $\mathbf{U}(\mathbf{x})$ is a steady solution of the Navier-Stokes equations. The linearization is performed neglecting the terms of order ε^2; the resulting system, governing the perturbation velocity $\tilde{\mathbf{u}}\,(\mathbf{x},t)$ reads

$$\frac{\partial\tilde{\mathbf{u}}}{\partial t} = -\left(\mathbf{U}\cdot\nabla\right)\tilde{\mathbf{u}} - \left(\tilde{\mathbf{u}}\cdot\nabla\right)\mathbf{U} - \nabla\tilde{p} + \frac{1}{Re}\nabla^2\tilde{\mathbf{u}} \tag{2.5a}$$

$$0 = \nabla\cdot\tilde{\mathbf{u}} \tag{2.5b}$$

The linearized Navier–Stokes equations set can be discretized in space, resulting in an initial-value problem

$$\dot{\tilde{\mathbf{u}}}(t) = \mathbf{A}\tilde{\mathbf{u}}(t) \tag{2.6a}$$

$$\tilde{\mathbf{u}}(0) = \tilde{\mathbf{u}}_0 \tag{2.6b}$$

The action of $\mathbf{A} \in \mathbb{R}^{n\times n}$ on $\tilde{\mathbf{u}} \in \mathbb{R}^n$ corresponds to evaluating the right-hand side of the linearized Navier–Stokes equations and enforcing the boundary conditions.

2.2. Introducing inputs and outputs

As suggested by Bewley (2001), the only requirement to achieve the desired flow behavior is that suitable control signals are determined based on filtered information delivered from the sensors. Thus, the relation among the inputs and the outputs is crucial for an efficient control design. The input-output dynamics of the system can be described defining a *linear state-space system* as

$$\dot{\mathbf{u}}(t) = \mathbf{A}\mathbf{u}(t) + \mathbf{B}\mathsf{f}(t) \tag{2.7a}$$

$$\mathsf{y}(t) = \mathbf{C}\mathbf{u}(t) + \mathbf{D}\mathsf{f}(t), \tag{2.7b}$$

where the tilde has been omitted for brevity. The quantity $\mathsf{f}(t) \in \mathbb{R}^m$ denotes the input and $\mathsf{y}(t) \in \mathbb{R}^p$ is the output the system. The matrix $\mathbf{A} \in \mathbb{R}^{n\times n}$ represents the action of the Navier-Stokes operator, as already introduced. The matrices $\mathbf{B} \in \mathbb{R}^{n\times m}$ and $\mathbf{C} \in \mathbb{R}^{p\times n}$ are usually low-rank (*i.e.* $m, p \ll n$) and describe the spatial distribution of the actuators and sensors, respectively. Finally, the matrix $\mathbf{D} \in \mathbb{R}^{p\times m}$ is defined as

$$\mathbf{D} = \begin{pmatrix} 0 & 0 & I_l \\ 0 & I_\alpha & 0 \end{pmatrix}, \tag{2.8}$$

where the vectors $I_\alpha \in \mathbb{R}^p$ simulates the noisy corruption of the measurements and the matrix $I_l \in \mathbb{R}^{k\times m}$ represents the control penalty; indeed the energy

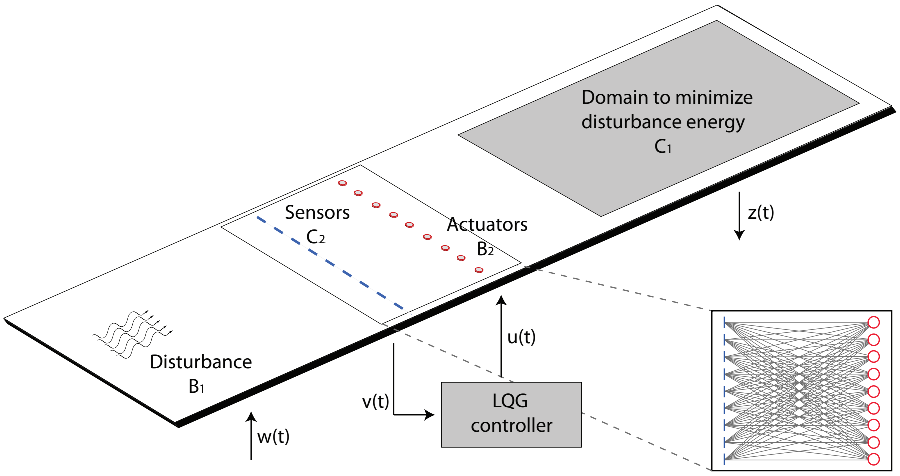

Figure 2.1. Input-output configurations. The input $\mathbf{B}_1$ is an optimal initial condition. The control action is provided by the input $\mathbf{B}_2$, which consists of a row of actuators located. The output $\mathbf{C}_2$ contains an array of sensors used for flow estimation. The effect of the controller is quantified by $\mathbf{C}_1$; all the estimation sensors are connected to all the actuators (*centralized control*).

expended by the actuator has to be limited in order to design an efficient controller. The formal solution of the stable system (2.7) is given by

$$\mathsf{y}(t) = \mathbf{C}\int_{-\infty}^{t} e^{\mathbf{A}(t-s)}\mathbf{B}\mathsf{f}(s)ds, \tag{2.9}$$

assuming both the initial condition $\mathbf{u}_0$ and the term $\mathbf{D}$ to be zero. Note that the solution given in (2.9) provides a linear mapping from the input signals to the output signals.

A sketch of the configuration is depicted in figure 2.1, where the actuators and sensors are schematically indicated. This setup is used for the control of three-dimensional disturbances in the boundary layer shown in figure 1.1.

The first input $\mathbf{B}_1$ is located upstream and models an incoming external perturbation. In this thesis, the optimal initial conditions leading to the largest energy growth for a final time are used; a streaky packet is obtained for short time of optimization, whereas long time leads to a localized initial condition triggering packets of TS-waves, as shown by Monokrousos *et al.* (2010). The second input $\mathbf{B}_2$ is the actuator; it consists of an array of elements distributed along the spanwise direction. Each element of the actuator $\mathbf{B}_2$ is represented by a volume forcing, localized in a region close to the wall. Two sensors are used, $\mathbf{C}_1$ and $\mathbf{C}_2$. The first sensor is located downstream and quantifies the action of the controller. The second sensor $\mathbf{C}_2$ consists of a number of localized elements, located a short distance upstream of the actuators; the configuration of the sensors array is the same as that characterizing the actuators line. With this definitions, (2.7) reads

$$\begin{aligned} \dot{\mathbf{u}}(t) &= \mathbf{A}\mathbf{u}(t) + \mathbf{B}_1\mathsf{w}(t) + \mathbf{B}_2\phi(t), && (2.10a)\\ \mathsf{z}(t) &= \mathbf{C}_1\mathbf{u}(t) + I_l\phi(t), && (2.10b)\\ \mathsf{v}(t) &= \mathbf{C}_2\mathbf{u}(t) + I_\alpha\mathsf{g}(t), && (2.10c) \end{aligned}$$

where the physical shape of the inputs/outputs is given by the matrices $\mathbf{B} = (\mathbf{B}_1, 0, \mathbf{B}_2)$ and $\mathbf{C} = (\mathbf{C}_1, \mathbf{C}_2)^T$. The temporal behaviour of the system is described by the input vector $\mathsf{f}(t) = (\mathsf{w}, \mathsf{g}, \phi)^T$ and the output vector $\mathsf{y}(t) = (\mathsf{z}, \mathsf{v})^T$, respectively. In more detail, the signals ϕ feed the actuators with a control signal based on the noisy measurement signals contained in the vectors v and extracted by the sensors $\mathbf{C}_2$; the noise corruption is introduced by the unit-variance white noise g. The aim is to minimize the perturbation energy in the region defined by $\mathbf{C}_1$; thus the output z can be regarded as the objective function of the controller. For more details about the configuration, we refer to Semeraro *et al.* (2010).

CHAPTER 3

A portrait of the flow: linear and nonlinear decompositions

In this chapter, two different approaches are introduced for the analysis of complex flows: the proper orthogonal decomposition (POD) and the Koopman modes analysis. For both cases, time-resolved PIV measurements of a confined co-flowing turbulent jet are considered; a snapshot from the experimental measurements is shown in figure 3.1. The two decompositions extract information from datasets, obtained either by numerical simulations or experiments. POD modes represent the most energetic structures of the flow, not related – in general – to a specific frequency. Conversely, the Koopman modes analysis allows the identification of flow structures related to a certain frequency; the associated modes, in this case, can be regarded as harmonic averages.

POD modes are briefly introduced in section 3.1. Koopman modes are described in section 3.2. A detailed introduction of the Koopman modes is beyond the scope of this thesis; however the definition is provided and the numerical procedure - the dynamic mode decomposition (DMD) - is briefly outlined.

3.1. Proper orthogonal decomposition

Given a set of flow-field snapshots $\{\mathbf{u}_1, \mathbf{u}_2, \ldots, \mathbf{u}_m\}$, taken from a time interval $[0, T_f]$, proper orthogonal decomposition determines the most energetic structures of the flow by diagonalizing the correlation matrix

$$\mathbf{R} = \int_0^{T_f} \mathbf{u}\mathbf{u}^T dt \tag{3.1}$$

The eigenfunctions are orthogonal and real-valued and the eigenvalues are real and positive; thus, it is possible to rank them in descending order. The energy related to each function is contained in the corresponding eigenvalue. A projection onto the subspace spanned by m POD modes provides an optimal finite-dimensional representation of the initial data-set of dimension m (Holmes *et al.* 1996).

The temporal information can be recovered projecting back the entire sequence of snapshots on the obtained basis or using the bi-orthogonal decomposition (BOD), where a second set of temporal modes is computed by diagonalizing the spatial-average cross-correlation (see Aubry 1991). In literature, the

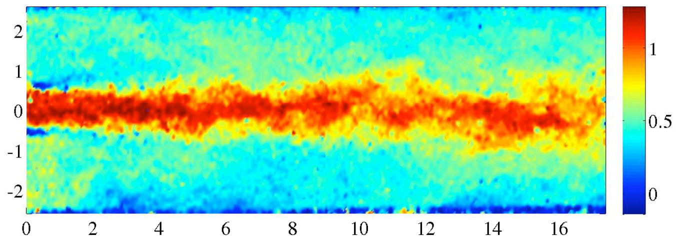

FIGURE 3.1. Snapshot of the turbulent jet from the PIV measurements; the streamwise component is shown at $t \approx 1.4$. The color-bar indicates the velocity values.

spatial modes are usually referred as *topo*-modes, while the temporal modes are referred as *chrono*-modes.

The first three POD modes obtained from the analysis of the jet are shown in figure 3.2; the modes are computed using the snapshot method (Sirovich 1987). The first mode (figure 3.2*a*) represents the mean flow and is associated to the largest eigenvalue; the corresponding *chrono*-mode is constant. The second and third *topo*-modes - figure 3.2($b - c$) - come in pairs: this is not surprising. Indeed, the POD modes are real-valued functions and two real-valued functions are required to describe flow structures traveling as a wavepacket (see, e.g, Rempfer & Fasel 1994). This is also clear from the analysis of the corresponding *chrono*-modes in time domain (figure 3.2*d*), and spectral domain (figure 3.2*e*). Indeed, the frequencies characterizing the time-behaviour are the same for both the modes. In the latter figure, the frequency is reported in dimensionless form as St, the Strouhal number, defined as $St = f(d/2)/U_c$, where f is the frequency, d is the diameter of the internal jet and U_c a characteristic velocity of the flow. From the physical point, these modes are related to the flapping of the turbulent jet.

Thus, POD allows to identify spatial coherent structures and rank them in descendent order according to the energy contents. Unfortunately, this criterion is not always a meaningful measure: low-energy structures can sometimes be more relevant for the flow analysis than high-energy ones.

3.1.1. *POD and controllability: an alternative perspective for linear systems*

Before describing the Koopman modes analysis, we step back and consider again (2.10) with inputs and outputs. In particular, when the actuators and sensors are localized in a small region close to the wall as sketched in figure 2.1, the actuators can manipulate only certain structures of the flow, whereas the sensors can detect only a limited region of the system. Thus, it is crucial to identify the states that can be controlled or observed for control design. In particular, *controllability* is a property of a state-space realization and measures of the response of states to control inputs; a controllability test is provided by

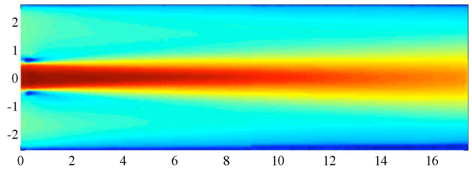

(a) *Topo*-mode 0, mean-flow

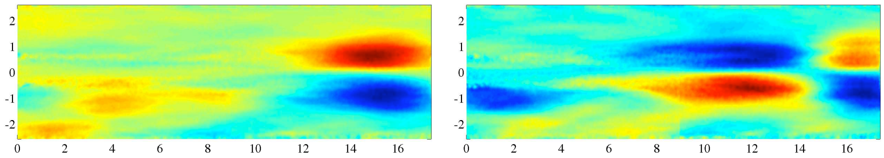

(b) First *topo*-mode

(c) Second *topo*-mode

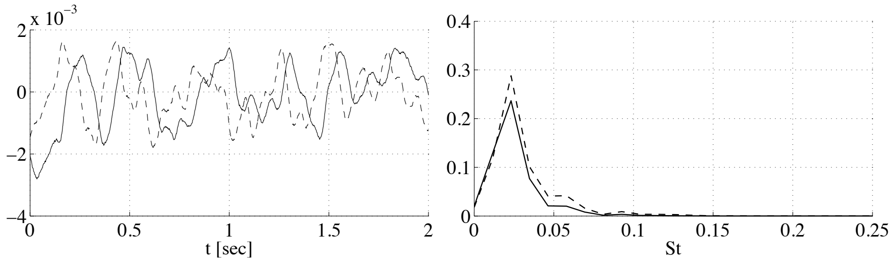

(d) *Chrono*-modes in time domain

(e) *Chrono*-modes in frequency domain

FIGURE 3.2. In $(a-c)$, the streamwise component is depicted; in (d) and (e), the solid line indicates the first *chrono*-mode, while the dashed dotted line indicate the second *chrono*-mode.

the *controllability Gramian*, defined as

$$\mathbf{P} = \int_0^\infty e^{\mathbf{A}t}\mathbf{B}\mathbf{B}^T e^{\mathbf{A}^T t} \mathrm{d}t, \tag{3.2}$$

and obtained as the solution of an optimal control problem, (see, e.g., Lewis & Syrmos 1995). Since the impulse response for the linear system (2.10) is given by $\mathbf{u} = e^{\mathbf{A}t}\mathbf{B}$, it is easy to recognize that the Gramian equals the correlation function (3.1). Thus, the eigenvectors obtained from the diagonalization of (3.2) can be regarded as POD modes and are characterized by the same properties listed above. In this context, these modes represent the most controllable structures of a flow. In control theory, POD analysis is usually referred to as principal component analysis (PCA).

For sake of completeness, note that an analogous analysis can be undertaken when *observability* is considered; like controllability, observability is a property of the state-space realization and describes the ability to reconstruct the states from available measurements. Both concepts are essential for the identification of the input-output behaviour of a system including sensors and actuators, as discussed in section 4.1.

3.2. Koopman modes and dynamic mode decomposition

A drawback of POD is related to the temporal description; although frequencies are captured by the *chrono*-modes, we cannot identify structures related to only one frequency. Moreover, the correlation function provides second-order statistics ranked according to the energy content; in general, low-energy structures can be relevant for a detailed flow analysis. Koopman modes analysis was recently proposed by Rowley *et al.* (2009); this method is also available for experimental measurements.

In order to describe this technique, we need to introduce the definition of *observable*. An observable is a function that associates a scalar to a flow field; in general, we do not have access to the full flow field in experiments: the velocity – or the other physical quantities – are probed at a point, using hot wires, or in a plane, using PIV. However, considering a fully nonlinear flow, the analysis of the observable for a statistically long interval of time is sufficient to reconstruct the phase space and investigate the flow behaviour. By definition, the Koopman operator U is a linear mapping that propagates the observable $a\left(\mathbf{u}\right)$ forward in time

$$Ua\left(\mathbf{u}\right) = a\left(\mathbf{g}\left(\mathbf{u}\right)\right) \tag{3.3}$$

and is associated to the nonlinear operator $\mathbf{g}$. It can be shown that the operator is linear and unitary as $t \to \infty$; in this case, the eigenfunctions basis constitutes an orthonormal expansion basis

$$U\psi_j\left(\mathbf{u}\right) = \mu_j \psi_j\left(\mathbf{u}\right), \qquad j = 0, 1, 2 \ldots \tag{3.4}$$

where μ_j denotes the eigenvalues. If a sequence of observables is considered, starting from an initial condition $\mathbf{u}_0$

$$\mathbf{X} = \left[\mathbf{a}\left(\mathbf{u}_0\right), \mathbf{a}\left(\mathbf{u}_1\right), \mathbf{a}\left(\mathbf{u}_2\right), \ldots\right], \tag{3.5}$$

an orthogonal projection of the k^{th} sample onto the space spanned by the Koopman eigenfunctions yields the expression

$$\mathbf{a}\left(\mathbf{u}_k\right) = U^k \mathbf{a}\left(\mathbf{u}_0\right) = U^k \left(\sum_{j=0}^{\infty} \psi_j\left(\mathbf{u}_0\right)\phi_j\right) = \sum_{j=0}^{\infty} \mu_j^k \psi_j\left(\mathbf{u}_0\right)\phi_j \tag{3.6}$$

The expansion coefficients ϕ_j, given by the integral

$$\phi_j = \int \mathbf{a}\left(\mathbf{u}_0\right)\psi_j^*\left(\mathbf{u}_0\right) \mathrm{d}\mathbf{u}_0, \tag{3.7}$$

are defined as the j^{th} Koopman mode associated to the map $\mathbf{g}$. Some interesting properties characterize these modes:

1. Each Koopman mode is associated with an amplitude that indicates its significance.

2. The temporal behaviour is given by the associated Koopman eigenvalues; the phase $\arg(\mu_i)$ determines its frequency and the magnitude $|\mu_i|$ determines the growth rate of the mode.

From the physical point of view, the computed modes are harmonic components of the flow, oscillating at certain frequencies given by the eigenvalues of the operator. For a periodic case, these modes are Fourier modes; when a linearized flow is considered, these modes are global modes. For a detailed introduction to the properties of this decomposition we refer to Mezić & Banaszuk (2004); Mezić (2005); Rowley *et al.* (2009); Bagheri (2010).

3.2.1. *Dynamic mode decomposition (DMD)*

The dynamic mode decomposition (DMD) is an algorithm proposed by Schmid (2010). Essentially, the DMD algorithm belongs to the category of Arnoldi methods for the computation of the eigenvalues and the related eigenvectors of a system: a low-order model of the system is identified, whose eigenvalues - referred to as *Ritz values* - approximate the *most important* eigenvalues of the true system. In the classical Arnoldi method the basis is computed via a Gram-Schmidt orthogonalization (Arnoldi 1951; Saad 1980), that requires a model of the system. An alternative is given by a projection basis defined using a collection of samples or snapshots (Ruhe 1984). Given a snapshot (observable) at time t_j, the successive snapshot (observable) at a later time t_{j+1} is given by

$$\mathbf{u}_{j+1} = \mathbf{A}\mathbf{u}_j. \tag{3.8}$$

The defined sequence

$$\mathbf{X}_{r+1} = [\mathbf{u}_1 \quad \mathbf{A}\mathbf{u}_1 \quad \mathbf{A}\mathbf{u}_2 \quad \ldots \quad \mathbf{A}\mathbf{u}_r] \tag{3.9}$$

will gradually become ill-conditioned. Indeed, the columns of the sequence align progressively to the dominant direction of the operator $\mathbf{A}$. On the other hand, the last snapshot can be written as

$$\mathbf{u}_{r+1} = c_1\mathbf{u}_1 + c_2\mathbf{u}_2 + \ldots + c_r\mathbf{u}_r + \tilde{\mathbf{u}}_{r+1}, \tag{3.10}$$

expanding it on a basis constituted by the previous r snapshots. Here, $\tilde{\mathbf{u}}_{r+1}$ indicates the residual error. Defining the sequence $\mathbf{X}_r$ as

$$\mathbf{X}_r = [\mathbf{u}_1 \quad \mathbf{A}\mathbf{u}_1 \quad \mathbf{A}\mathbf{u}_2 \quad \ldots \quad \mathbf{A}\mathbf{u}_{r-1}], \tag{3.11}$$

the aim is to minimize the residual such that $\tilde{\mathbf{u}}_{r+1} \perp \mathbf{X}_r$. This can be cast into the form of a least-square problem, such that the elements c_j are given as a solution of it. Introducing the companion matrix

$$\mathbf{M} = \begin{pmatrix} 0 & 0 & \cdots & 0 & c_1 \\ 1 & 0 & \cdots & 0 & c_2 \\ 0 & 1 & \cdots & 0 & c_3 \\ \vdots & & \ddots & & \vdots \\ 0 & 0 & \cdots & 1 & c_r \end{pmatrix} \tag{3.12}$$

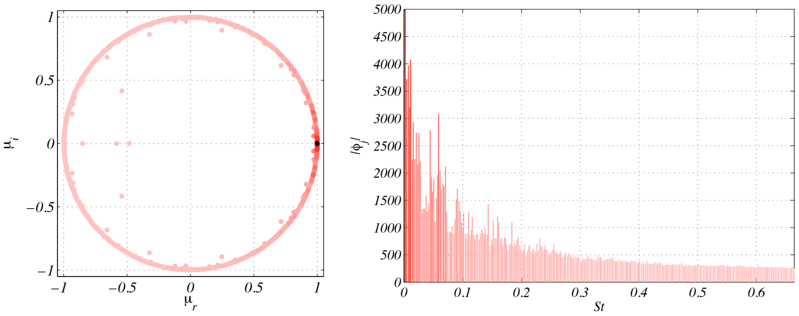

(a) Discrete spectrum (μ)

(b) Amplitude vs St

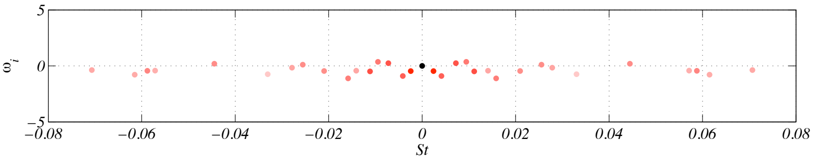

(c) Continuous spectrum; the real frequencies are reported as St

FIGURE 3.3. In (a), the black dot indicates the mean flow and is associated to the highest amplitude; all the amplitudes associated to each frequency are reported in (b). In (c) the most important eigenvalues are shown.

(3.10) is finally re-written as

$$\mathbf{A}\mathbf{X}_r = \mathbf{X}_r\mathbf{M} + \tilde{\mathbf{u}}_{r+1}\mathbf{e}_r^T \tag{3.13}$$

Thus, the companion matrix propagates forward in time the entire sequence of snapshots, whereas the last one is reconstructed using the coefficients c_j. The eigenvalues of $\mathbf{M}$ approximate the eigenvalues of the real system; the related eigenvectors are given by $\tilde{\mathbf{\Phi}} = \mathbf{X}_r\mathbf{T}$, where $\mathbf{T}$ are the eigenvectors of the companion matrix $\mathbf{M}$. Hence, this algorithm can be used to extract Ritz values and the related vectors from experimental data or sequence of snapshots of nonlinear simulations; moreover, as observed by Rowley *et al.* (2009), it approximates the Koopman modes.

A drawback of the method is the linear dependency of the dataset. An improvement of the algorithm is proposed by Schmid (2010), where a self-similarly transformed companion matrix $\mathbf{M}$ is used, resulting in a better-conditioned eigenvalue problem.

3.2.2. *Brief overview of the results*

In figure 3.3(a) the discrete spectrum associated to the Koopman/DMD analysis of a confined co-flowing turbulent jet is shown; as previously noticed, when the flow is fully developed, the eigenvalues tends to lie on an unitary circle. The

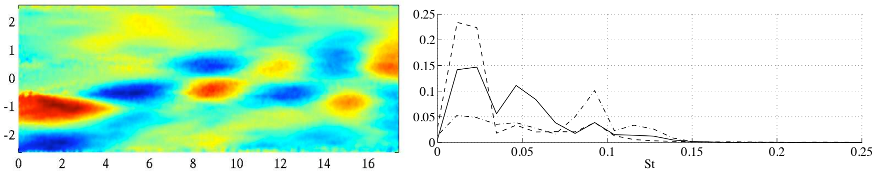

(a) *Topo*-mode (b) *Chrono*-mode

FIGURE 3.4. Fifth POD mode; the streamwise component, (*a*), and the spectral analysis, (*b*), are shown.

black dot indicates the mean flow and is associated to the highest amplitude mode; it corresponds to the first POD mode. The spectrum resulting from the DMD is discrete; the continuous spectrum is obtained applying the relation $\omega = log(\mu)/dt$, where dt is the sampling time. In figure 3.3(*b*), the amplitudes of the modes are represented as function of St. As shown by Rowley *et al.* (2009) and Bagheri (2010), the amplitudes allow to select only the modes that are significant from the physical point of view. Thus, the most relevant frequencies of the flow correspond to the peaks in figure 3.3(*b*); these are reported in the spectrum in 3.3(*c*)

The DMD is able to isolate structures associate to harmonics of the flow. An interesting example is reported in figure 3.4 and 3.5, where a comparison between the two techniques is proposed. The fifth POD mode (figure 3.4) show the simultaneous presence of shear layer phenomena, far downstream in the domain, and oscillation on the side of the inlet-jet, in the lower-upstream part of the domain; the resulting spectral analysis confirms the contemporary presence of lower and higher frequencies, related to the recirculation and shear flow structures, respectively. Using Koopman modes, it is possible to distinguish these physical phenomena (figure 3.5). In figure 3.5(*a*) an elongated lobe appears in the lower-upstream region of the domain; the structure is associated to a low frequency, $St = 0.01$, in agreement with the spectral analysis of the PIV measurements and POD modes. The shear flow structures are shown in figure 3.5($b-d$); the finer structures located downstream in the domain are associated to higher frequencies and closely resemble the structure already observed.

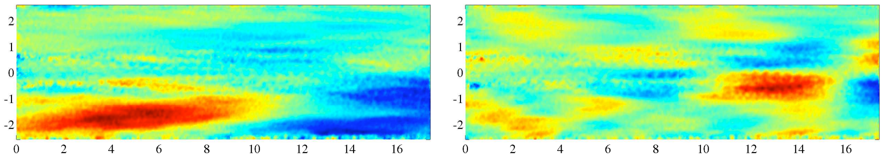

(a) $St = 0.01$ (b) $St = 0.04$

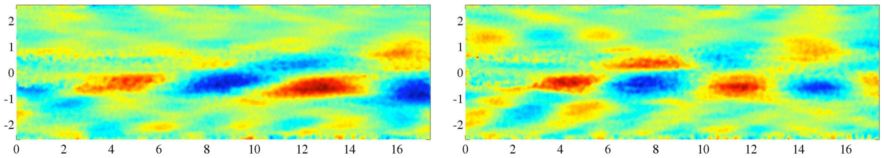

(c) $St = 0.06$ (d) $St = 0.07$

FIGURE 3.5. The streamwise component of four Koopman modes is shown. The associated Strohual number is reported in each label.

CHAPTER 4

Model reduction and flow control

In this section, the linear feedback controller is introduced; the aim is to quench the perturbations growing in the boundary layer, using a set of localized actuators close to the wall. Unfortunately, standard tools of linear control theory cannot be applied to large systems; in order to tackle this difficulty, reduced-order models are identified. The model reduction problem is introduced in section 4.1, where approximate balanced truncation is briefly outlined. The design of feedback control is summarized in section 4.2. Finally, a brief review of the main results is reported in section 4.3. The control of TS-wavepacket is used as an example; more details about streaks control are included in Semeraro *et al.* (2010).

4.1. Model Reduction using balanced truncation

The tools of linear control theory cannot be easily applied to large systems; in control theory, two different strategies are usually employed: i) Compute a high dimensional controller, reduce its dimensions and then apply it to the system you wish to control; ii) Identify a reduced-order model with proper techniques and build a small controller. In our case the number of degrees of freedom, $n \approx 10^7$, makes the first approach unfeasible, since the controller would be of the same dimension as the system. Moreover, from the experimental point of view, it is more relevant to compute a model of the flow directly from the measurements and design the control based on it. Thus, the second approach is applied; the procedure can be briefly outlined as follows:

1. Introduction of inputs and outputs in the linearized Navier-Stokes model.
2. Identification of a reduced-order model.
3. Design of a small controller, running in parallel with the main simulation.

Reduced-order models can be identified via a projection of the system onto a low-dimensional subspace, spanned by $r \ll n$ basis functions, $\mathbf{\Phi} = (\boldsymbol{\phi}_1, \boldsymbol{\phi}_2, \ldots, \boldsymbol{\phi}_r) \in \mathbb{R}^{n\times r}$. Thus, the flow field - or, in general, the state variable - is approximated as

$$\tilde{\mathbf{u}} = \sum_{j=1}^{r} q_j \boldsymbol{\phi}_j = \mathbf{\Phi} q \qquad (4.1)$$

where $q = (q_1, q_2, \ldots, q_r)^T \in \mathbb{R}^r$ are the scalar expansion coefficients. The coefficients are computed as

$$q = \mathbf{\Psi}^* \mathbf{u} \tag{4.2}$$

where $\mathbf{\Psi} = (\boldsymbol{\psi}_1, \boldsymbol{\psi}_2, \ldots, \boldsymbol{\psi}_r) \in \mathbb{R}^{n \times r}$ are adjoint modes, bi-orthogonal to the expansion basis $\mathbf{\Phi}$. Plugging (4.1) in the input-output system (2.10) and using the adjoint modes, the resulting reduced model of order r is computed, with $A = \mathbf{\Psi}^* \mathbf{A} \mathbf{\Phi}$, $B_i = \mathbf{\Psi}^* \mathbf{B}_i$ and $C_i = \mathbf{C}_i \mathbf{\Phi}$.

Clearly, the choice of the projection basis is crucial for the performance of the reduced-order system; for instance, the modal decomposition of the system and the projection onto a basis containing the least stable modes is a classical way to proceed when unstable systems are considered. However, we aim to build a model that preserves the dynamics between the actuators and sensors. Among all the possible flow disturbances, only a portion can be excited by the inputs and observed by the outputs; in literature, these states are referred as *controllable* and *observable* (see e.g. Glad & Ljung 2001; Bagheri *et al.* 2009). With a limited number of inputs and outputs, most of the states are weakly controllable and observable. Since the control design is based on the dynamics coupling the actuators and sensors, one way to proceed is to disregard uncontrollable/unobservable states. In such a way, the entire input-output behaviour of the system can be accurately reproduced by a reduced number of states.

Balanced truncation, first proposed by Moore (1981), represents a systematic way to perform this reduction. The procedure makes use of the Hankel operator to define the relation among the inputs and the outputs (Glover 1984); this operator is defined as

$$\mathsf{y}(t) = \mathbf{H}\mathsf{f}(t) = \int_{-\infty}^{0} \mathbf{C} e^{\mathbf{A}(t-s)} \mathbf{B} \mathsf{f}(s) ds. \tag{4.3}$$

and maps past inputs signals $\mathsf{f}(t)$ to future outputs $\mathsf{y}(t)$. As already noticed in section 2.2, the formal solution of (2.10) also provides a mapping between inputs and outputs of the system. Unfortunately, the mapping given by this solution is not a finite rank operator; conversely, it can be shown that the operator $\mathbf{H}$ has at most rank n for a state space of order n, resulting in an easier mapping to be handled, see Glover (1984).

Using the Hankel operator and the related adjoint operator $\mathbf{H}^*$, we can quantify the output energy obtained from a past input $\mathsf{f}(t)$, by

$$\|\mathsf{y}\|^2_{L^2} = \langle \mathbf{H}\mathsf{f}, \mathbf{H}\mathsf{f} \rangle_{L^2} = \langle \mathsf{f}, \mathbf{H}^* \mathbf{H} \mathsf{f} \rangle_{L^2}. \tag{4.4}$$

If a given input forcing $\mathsf{f}_i(t)$ is a unit-norm eigenvector of $\mathbf{H}^* \mathbf{H}$, then the output energy will be given by the square of the corresponding Hankel Singular Value (HSV) σ_i

$$\mathbf{H}^* \mathbf{H} \mathsf{f}_i(t) = \sigma_i^2 \mathsf{f}_i(t). \tag{4.5}$$

The HSVs are real and positive; thus, they can be ranked according to the associated energy amplification. The *balanced modes* ϕ_i associated with σ_i is

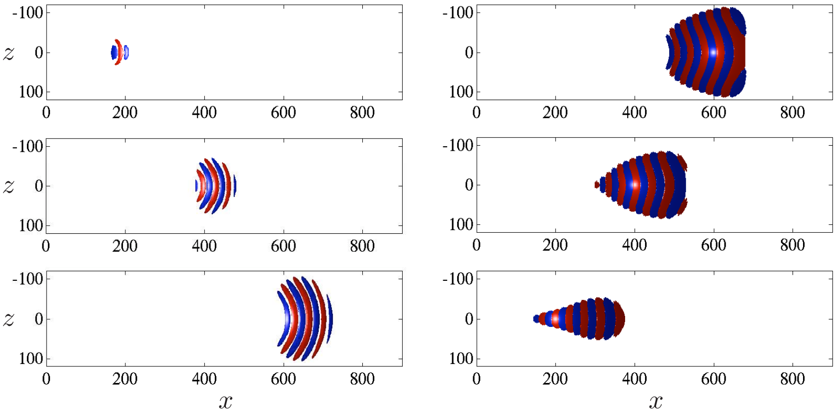

FIGURE 4.1. Snapshots used for balanced truncation; the streamwise component is depicted in all the insets. Left panels: snapshots from simulations at $t = 400, 1000, 1600$; an initial condition triggering packet of TS-waves is used. Right panels: snapshots from the adjoint simulations at $t = -400, -1000, -1600$.

defined as

$$\phi_i = \frac{1}{\sigma_i}\mathbf{L}_c \mathsf{f}_i \tag{4.6}$$

where $\mathbf{L}_c$ is the *controllability* operator (see Bagheri *et al.* 2009*a*; Semeraro *et al.* 2010). In an analogous way, the *adjoint balanced modes* are defined using the *observability* operator. The two sets of modes provide a suitable projection basis for computing the reduced-order model; moreover, their spatial support reveals peculiarities of the flow from the input-output point of view and provides physical insight for sensor/actuator placement. In fact, the resulting balanced mode ϕ_j is the global structure in the flow that is "influenced" by the input $\mathbf{B}_i$ by an amount given by its Hankel Singular Value (HSV). The corresponding adjoint mode ψ_j is a flow structure that – if used as an initial condition – will result in an output energy given by its corresponding HSV. For our application, an approximate basis of balanced modes - and the associated adjoint set - is computed using a snapshot-based method (Rowley 2005).

4.1.1. *Snapshot method*

An essential ingredient in the computation of the balanced modes is the identification of the *controllability* Gramian,

$$\mathbf{P} = \int_0^\infty e^{\mathbf{A}t}\mathbf{B}\mathbf{B}^* e^{\mathbf{A}^* t}\mathrm{d}t \tag{4.7}$$

and the *observability* Gramian,

$$\mathbf{Q} = \int_0^\infty e^{\mathbf{A}^* t}\mathbf{C}^*\mathbf{C}e^{\mathbf{A}t}\mathrm{d}t. \tag{4.8}$$

Both the Gramians are semi-positive definite; thus, the eigenvalues are real and positive and can be easily ranked. The analysis of the controllability Gramian allows to identify and rank the states that are more influenced by an input, as already introduced in the previous section. The observability Gramian identifies the states that produce the largest output energy; the rank is provided by the eigenvalue-decomposition of the Gramian $\mathbf{Q}$. The definitions are strictly connected to the controllability and observability operators (see Bagheri *et al.* 2009*a*; Semeraro *et al.* 2010). Using these operators, it is shown that balanced modes are equivalently obtained as

$$\mathbf{PQ}\phi_i = \sigma_i^2\phi_i, \qquad i = 1, \ldots, n \tag{4.9}$$

The adjoint set is represented by the set of left eigenvectors. Following Laub *et al.* (1987), a Cholesky decomposition can be performed, such that

$$\mathbf{P} = \mathbf{XX}^*, \qquad \mathbf{Q} = \mathbf{Y}^*\mathbf{Y}. \tag{4.10}$$

The Gramians can be computed as solutions of Lyapunov equations, (Green & Limebeer 1995). The following singular value decomposition (SVD) is performed

$$\mathbf{Y}^*\mathbf{X} = \mathbf{U\Sigma V}^*. \tag{4.11}$$

The diagonal matrix $\mathbf{\Sigma}$ contains the HSVs. The direct and adjoint balanced modes are then given by

$$\mathbf{\Phi}_r = \mathbf{XV\Sigma}^{-1/2} \qquad \mathbf{\Psi}_r = \mathbf{Y}^*\mathbf{U\Sigma}^{-1/2}. \tag{4.12}$$

Unfortunately, the solution of the Lyapunov equations involves a computational complexity $O(n^3)$ and a storage requirement $O(n^2)$ making it prohibitive for high-dimensional systems. The snapshot method is based on the identification of empirical Gramians (Rowley 2005). Low-rank Cholesky factors are formed using snapshots collected from the numerical simulations; in particular, snapshots are collected marching the simulations forward in time with the inputs introduced as initial condition, in order to obtain low-order Cholesky factor $\tilde{\mathbf{X}} \in \mathbf{R}^{n\times n_t p}$; similarly, the Cholesky factor $\tilde{\mathbf{Y}}$ can be obtained by sampling snapshots computed by marching backward in time the adjoint system. Snapshots samples are shown in figure 4.1. Using a localized packet triggering TS-waves as initial condition, three different instants of time are shown in the left panel, while three snapshots from the adjoint simulation are shown in the right panel. The number of simulations equal the total number of inputs and outputs. As long as the number of degrees of freedom n is much larger than the number of collected snapshots, the method is cheaper than the standard method.

Using the low-rank Cholesky factors, the approximate direct and adjoint balanced modes are computed following the procedure previously outlined. In

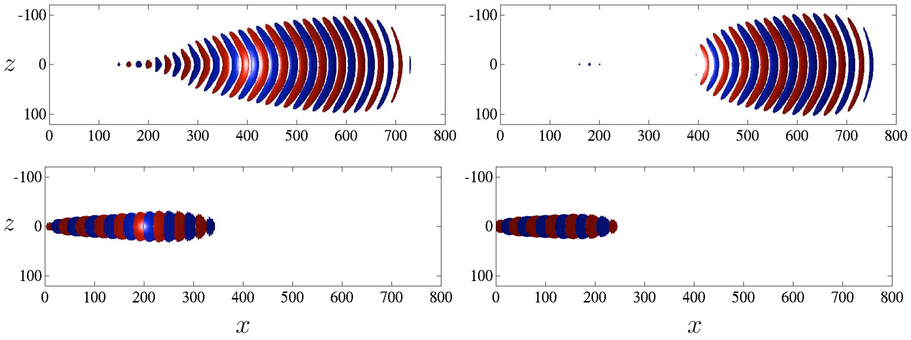

FIGURE 4.2. Balanced modes and related adjoint modes for the TS waves. Left column: streamwise component of the first couple of balanced/adjoint balanced modes. Right column: streamwise component of the third couple of balanced/adjoint balanced modes.

figure 4.2, the first and third balanced modes, and the associated adjoint modes are shown for the TS-wavepacket case. In similar way, a set of balanced modes is computed when considering streaks (see Semeraro *et al.* 2010). Numerical tests have shown that the approximate balanced modes are a good approximation to exact balancing modes and that Σ_r are close to the true HSVs (Ilak & Rowley 2008; Ahuja 2009; Bagheri *et al.* 2009*a*).

In conclusion, note that an equivalent reduced-order model can be identified directly from the input/output signal analysis using system identification algorithms. An example is given by the Eigensystem Realization Algorithm (ERA); it represents an approach formally equivalent to the balanced truncation as shown by Ma *et al.* (2009), although it is computationally cheaper. Identification algorithms are particularly suited to experimental setups; indeed, the model is built on measurements extracted locally and full knowledge of the flow-field is not necessary.

4.2. Feedback control design

The reduced-order model allows us to easily access the tools of linear control for the compensator design. The controller is designed using the linear quadratic Gaussian (LQG) approach; within this approach, the control signal ϕ has to be determined, such that an objective function is minimized. In our case, this criterion reads as follows

$$\mathcal{E}\left(\|\mathsf{z}\|_{L^2}\right) = \mathcal{E}\left(\int_0^\infty q^T C_1^T C_1 q + \phi^T I_l^T I_l \phi \;\mathrm{d}t\right). \tag{4.13}$$

Thus, the controller provides a control signal $\phi(t)$ for the actuators $\mathbf{B}_2$, based on the noisy measurements $\mathsf{v}(t)$ extracted from the sensors $\mathbf{C}_2$, such that the mean of the output energy of z is minimized. Moreover, the second term of the right-hand side allows to penalize the control effort. The *separation principle* states that the problem can be split in two steps, performed independently:

1. The estimation problem consists of an optimization, which can be solved without any reference to the control problem.
2. It is assumed that the control signal $\phi(t)$ can be computed using the relation
$$\phi(t) = Kq(t), \tag{4.14}$$
where K is referred to as the control gain.

The so-called *compensator* consists of an *estimator*, that provides an estimation of the flow, and a controller that computes the control input and feeds the actuators. If each of the two separate problems is stable, the final compensator, obtained from the optimal estimator and the optimal controller, will be stable. Moreover, the closed-loop system will be optimal (Anderson & Moore 1990). For a derivation of the LQG solution, we refer to e.g. Lewis & Syrmos (1995), Doyle *et al.* (1989) or Dullerud & Paganini (1999); in the following the two problems are briefly stated.

4.2.1. *Estimation problem*

The first step in constructing a controller is to estimate the full state $\mathbf{u}$ given only the noisy measurements $\mathsf{v}(t)$. The estimator is defined as
$$\dot{\hat{q}}(t) = A\hat{q}(t) + B_2\phi(t) - L(\mathsf{v}(t) - \hat{\mathsf{v}}(t)). \tag{4.15}$$
The reconstructed state is denoted by $\hat{q}(t) \in \mathbb{R}^r$ and is of the same dimensions as the reduced model. In the last term of the right-hand side of (4.15), the noisy measurements v extracted from the sensors $\mathbf{C}_2$ are compared with the measurements $\hat{\mathsf{v}} = C_2\hat{q}$ computed from the estimated state. The estimation gain L is computed casting an optimization problem, where the estimation error $\|q - \hat{q}\|$ has to be minimized. It can be shown (Kalman 1960) that the estimation gain is given by
$$L = -\frac{1}{\alpha^2}YC_2^T, \tag{4.16}$$
where $Y \in \mathbb{R}^{r\times r}$ is a solution to the algebraic Riccati equation
$$AY + YA^T - YC_2^TC_2Y + B_1B_1^T = 0 \tag{4.17}$$
Note that the solution to the Riccati equation for a problem of order n requires a computational cost of order $O(n^3)$, which is intractable for a large system with $n > 10^5$.

4.2.2. *Optimal Control*

A second optimization problem is formulated in order to compute the control gain K. We assume that the full state is given by q at all times. Inserting the feedback relation into (2.10) and neglecting the output v, we get
$$\dot{q}(t) = (A + B_2K)q(t) + B_1\mathsf{w}(t) \tag{4.18a}$$
$$\mathsf{z}(t) = C_1q(t) + I_l\phi(t). \tag{4.18b}$$

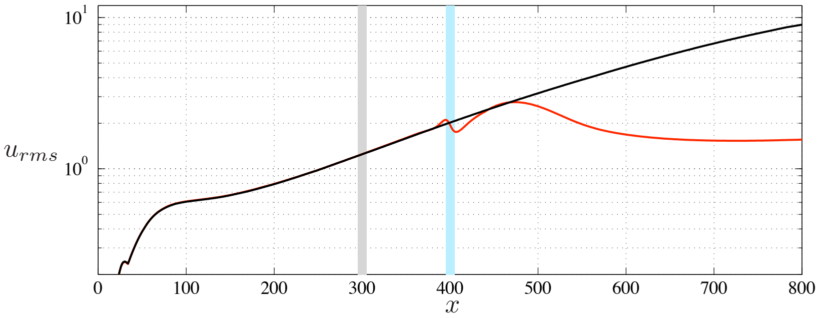

(a) Control of TS-waves

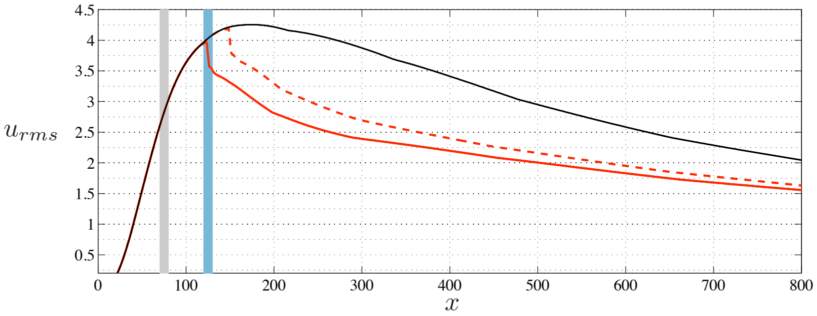

(b) Control of streaks

FIGURE 4.3. The r.m.s. values of the controlled systems (red line) are compared with the uncontrolled system (black line). The location of the actuators and sensors is indicated with a blue and grey region, respectively.

The gain K is chosen such that the system is stable and the control signal $\phi(t)$ satisfies the objective function (4.13). The solution is provided by a optimal control state-feedback problem, (see e.g. Anderson & Moore 1990), where the control signal is given by

$$K = -\frac{1}{2}\left(I_l^T I_l\right)^{-1} B_2^T X, \tag{4.19}$$

and X is a solution of the Riccati equation

$$AX^T + XA + XB_2B_2^TX + C_1^TC_1 = 0. \tag{4.20}$$

It can be shown that the optimal control signal is given by $\phi(t) = K\hat{q}(t)$, where K is the control gain computed for the full state and $\hat{q}$ is the estimated state. Finally, the LQG compensator is obtained combining the estimator (4.15) and

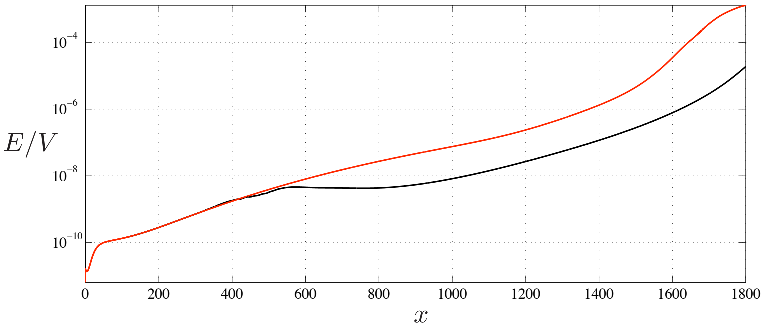

FIGURE 4.4. Energy-density evolution as function of x; the uncontrolled case (red line) is compared with the respective controlled case (black line).

the controller

$$\begin{aligned} \dot{\hat{q}}(t) &= (A + B_2K + LC_2)\hat{q}(t) - L\mathsf{v}(t) && (4.21a) \\ \phi(t) &= K\hat{q}(t). && (4.21b) \end{aligned}$$

The main disadvantage of LQG is its limited robustness; indeed, uncertainties of the underlying system are not accounted for within the framework. The robustness check can be performed *a posteriori*, testing the controller at off-design conditions.

4.2.3. *Centralized vs. decentralized approach*

The spatial localization of the actuators and the sensors requires a proper multi-variable approach for the controller design. In the simplest approach each actuator is connected to only one sensor (in our case, the corresponding upstream sensor). In such a case, an equal number of actuators and sensors is required and each loop can be regarded as a single-input-single-output (SISO) setting; thus, the compensator consists of a number of closed-loops that equals the number of actuators/sensors. In this case, the controller is called *decentralized*; if the decentralized controller is stable in each SISO loop and the inputs and outputs are decoupled or only weakly coupled, then the closed-loop is also stable. Conversely, when the system is characterized by strong cross-coupling, the closed-loop is not guaranteed to be stable. Preliminary tests performed using DNS show that this approach cannot be applied to our system. Thus, a *centralized control* is adopted, where all actuators are connected to all sensors, as sketched in the inset of figure 2.1.

4.3. Towards laminar-turbulent transition delay

The designed controller is included in the numerical simulations; we analysed the dynamics of the controlled perturbation within the linear framework, for both streaks and TS-waves. The u_{rms} as function of the streamwise direction is shown in figure 4.3. The energy is damped by about one order of magnitude after the actuation when TS-waves are considered, see figure 4.3(*a*); the location of the sensors and the actuators is marked with a grey and a blue line, respectively. The controller quenches the propagating disturbance similarly to opposition controller, transforming the original structure into more complex 3D structure as shown in the introduction, figure 1.1. For the streaks case (figure 4.3*b*), a second low-dimensional model is built, using the same typology of actuators and sensors. A sudden drop of the u_{rms} is observed at the actuator location. The effect of the actuator location is also shown: moving the array further upstream leads to an improvement of the u_{rms} reduction.

When three dimensional TS wavepackets with realistic amplitudes of the initial perturbation are considered, the energy reduction obtained using the controller results in a delay of the initial stages of the transition process. As shown in figure 4.4, the original uncontrolled undergoes a rapid energy amplification, which is delayed when turning on the control. Indeed, mitigation of the energy is observed soon after the actuation, when the controller is active. Later, a renewed TS-wavepacket appears and a second energy growth is observed; however, the entire transition process is delayed by about $\Delta Re_x \approx 3 \times 10^5$.

CHAPTER 5

Summary of the papers

Paper 1

Feedback control of three-dimensional optimal disturbances using reduced-order models

We apply feedback control to mitigate the growth of small-amplitude three-dimensional disturbances in boundary layer flows. Numerical simulations are performed at $Re_{\delta_0^*} = 1000$, corresponding to $Re_x \approx 3 \times 10^5$ at the computational inlet. Low dimension models capture the input-output behavior of the flat-plate boundary layer; optimal feedback control is designed, based on a reduced-order model, in combination with localized sensors/actuators (10 to 20 elements). It is shown that with only $n = 60$ degrees of freedom the entire input-output behaviour of the full linearized Navier-Stokes, $n \approx 10^7$ system is captured.

The localized initial conditions introduced provide the maximum energy growth for a given final time. We demonstrate that the energy of three dimensional Tollmien-Schlichting wavepacket – obtained for long-time optimization – is damped by two order of magnitude using 9 sensors for the estimation and 9 actuators. The control performance is investigated when reducing the number of sensors and actuators in the configuration: it was found that a controller based on a reduced number of actuators affects significantly the performance of the device. When streaky wavepackets – associated with short time of optimization – are considered, the perturbation energy is damped using 8 sensors for the estimation and 8 sensor for the actuation.

The influence of the controller effort, the noise contamination of the measurements and the position of the arrays are analysed. Moreover, a robustness study is carried out. The designed controller schemes are robust also when strong deviations of the Reynolds number are considered, whereas a less satisfactory behaviour was found when uncertainties of the pressure gradient are considered.

Paper 2

Transition delay in boundary layer flow using feedback control

Delay of the transition process using a feedback controller based on localized sensors/actuators is shown. Three dimensional Tollmien-Schlichting wavepackets with realistic initial amplitudes are considered. The controller is designed using a reduced-order model; the disturbances are mitigated during the early stage of the propagation, when the flow is still laminar. The action of the controller resulted in a significant reduction of the perturbation energy of the disturbance and - later - in a delay of the transition process; a parametric analysis is carried out, adjusting the controller effort and using different finite-amplitudes for the initial conditions. The streamwise delay of transition is estimated in terms of Reynolds number as $\Delta Re_x \approx 3 \times 10^5$.

The analysis of the actuation clearly reveals the excitation of higher order harmonics; the excitation is related to the three-dimensionality of the controller action, combined with the non-linearities of the uncontrolled flow. Starting from this knowledge, a further improvement of the device can be achieved, including - for instance - the non-linear effects during the modeling process.

Paper 3

Analysis of time-resolved PIV measurements of a confined co-flowing jet using POD and Koopman modes

Modal analysis by proper orthogonal decomposition (POD) and dynamic mode decomposition (DMD) of experimental data from a fully turbulent flow is presented. The flow case is a turbulent confined jet with co-flow, with Reynolds number based on the jet thickness of Re=10700. Experiments are performed with time-resolved PIV. The jet is fully turbulent; however the results from the spectral analysis shows the presence of periodic features, arising from the flapping of the jet induced by a recirculation zone on the side of the inner jet.

Jet flapping appears as two large structures located downstream on the first two POD modes. These two modes appear to be coupled to each other; frequency analysis shows a clear peak at ($St = 0.02$), in line with previous experimental results. POD-modes 3, 4 and 5 show the coupling between the recirculation zone near the inlet and shear-layer oscillation, which is believed to be the leading sustaining mechanism for the jet flapping. The DMD analysis clearly isolates these structures, appearing in separate modes; thus, the method efficiently identifies structures with a single frequency. The peaks found by spectral analysis of the POD time coefficient are in good agreement with the frequencies found by DMD. A selection procedure able to retain only the modes physically relevant is proposed within the DMD framework.

CHAPTER 6

Conclusions and outlook

This chapter contains an overview of the results and few outlines for the future developments of this work.

Feedback control in boundary layer flows

Numerical simulations of a flat-plate boundary layer have been performed. We have applied feedback optimal control to quench the arising perturbation; to this end inputs and outputs have been included in the system. The first input is represented by initial conditions providing a disturbance exploiting the maximum energy growth for a given final time; the second input is represented by an array of localized actuators, that act on the the flow. The outputs allow us to detect the flow: a set of localized sensors is introduced upstream of the actuators; the measurements extracted from the flow allow to compute the control signal which is then fed to the actuators. A second set of sensors quantifies the action of the controller downstream of the actuators. However, the complexity of the flow and the number of degrees of freedom arising from the discretization of the Navier-Stokes equation prohibit the application of the control theory tools; to tackle these difficulties, the controllers are based on low-order models, built via a projection onto a suitable expansion basis. Since modern and robust control is based on the input-output formulation, a successful controller can be designed using a model able to reproduce the dynamics between the sensors and actuators. To this end, balanced truncation is used.

Within the linear framework, we demonstrate that the energy of three dimensional Tollmien-Schlichting wavepacket, obtained for long-time optimization, is damped by two orders of magnitude. It was found that a smaller number of actuators decreases the effectiveness of the controller significantly, whereas a reduced number of sensors has a smaller impact on the performance. When an initial condition triggering a streaky wavepacket is considered, the controller is able to damp by half the perturbation energy.

The drastic reduction of the perturbation energy results in a delay of transition to turbulence when three dimensional TS wavepacket with realistic amplitudes are considered. The controller quenches the disturbances during the early stage of propagation, when the flow is still laminar, reducing the perturbation energy of the disturbance; this action results - later - in a delay of the transition process.

The performance of the control is degraded by the 3D nature of the controller action, combined with the non-linearities of the uncontrolled flow. Thus, an improvement of the performance can be achieved if the non-linear effects are explicitly accounted with during the modeling process or a more robust controller is used. More in general, the techniques of flow analysis tested for the confined turbulent jet, can provide physical insight on the flow and help us to improve the controllers.

These approaches can improve the controller performance even in more realistic cases; in particular, control of bypass transition due to free-stream turbulence (FST) or natural transition can be undertaken. Note that also within the linear modeling further improvements can be achieved; novel techniques for the model reduction, less computationally demanding than the balanced truncation, allow for more detailed parametric analysis of the optimal actuators/sensors placement. This aspect can result essential for the design of realistic actuators and sensors; indeed, numerical tests can help determining the most efficient form of actuation, provided these are correctly modeled in the simulations, and valuable information about th experimental set-up beforehand. Although flat-plate geometry was considered, this framework can also be applied to more complex geometries, for example an elliptic leading edge.

Analysis of experimental data

POD and DMD have been applied to experimental data from PIV measurements of a turbulent confined jet with co-flow. The jet is fully turbulent, however the results from the spectral analysis have shown the presence of periodic features, arising from the flapping of the jet induced by a recirculation zone on the side of the inner jet.

Spectral analysis of the PIV measurements, modal analysis by POD and DMD were used and compared. Jet flapping is identified by the first couple of POD modes. These two modes appear to be coupled to each other, as highlighted by the eye-inspection of the spatial structure and the temporal-analysis of the corresponding temporal modes. A recirculation zone appears on the side of the jet, which is believed to be the leading sustaining mechanism for the jet flapping; this mechanism is clearly identified by the DMD analysis together with the associated frequency.

DMD and POD are snapshot-based methods; thus, the same analysis framework can be easily applied for more detailed investigations of specific region of the flow using the same dataset (e.g., the inlet of the jet). Moreover, the analysis of the same flow with polymers can be undertaken.

Acknowledgments

I would like to thank Prof. Dan Henningson, for his guidance, inspiration and for giving me this opportunity. Dr. Luca Brandt is acknowledged for his bottomless inspiration, enthusiasm and patience with me. Many thanks to Dr. Shervin Bagheri, for teaching me the basics I needed for this project, and Gabriele Bellani, for the nice and fruitful cooperation. I learnt a lot from all of them and I am grateful for this.

Dr. Philipp Schlatter, Dr. Ardeshir Hanifi and Dr. Mattias Chevalier were always available to answer any question, thanks. Dr. Stefan Wallin, Dr. Miloš Ilak and Dr. Lars-Uve Schrader are gratefully acknowledged for the suggestions and comments on the manuscript. Thanks to Prof. Luigi de Luca and Dr. Gennaro Coppola, who advocated the PhD path.

My office-mates Antonios Monokrousos, Qiang Li and Johan Malm are acknowledged for sharing coffee-breaks, discussions (scientific and not) and jokes: $\epsilon\upsilon\chi\alpha\rho\iota\sigma\tau\acute{\omega}$, $xi\grave{e}-xi\grave{e}$, *tack* (respectively!).

Many thanks to the people of the group[1]: David Tempelmann, Lailai Zhu, Sasan Sarmast, Reza Dadfar, Mohammad (Armin) Hosseini, Dr. Ruth Lambert, Joy Klinkenberg, Dr. Yohann Duguet, Dr. Espen Åkervik, Dr. Gaetano Sardina and Dr. Carlo Cossu. Among the people from Mechanics, I like to thank Dr. Andreas Vallgren, Enrico Deusebio, Amin Rasam and Zeinab Pouransari, Andreas Carlson, Dr. Antonio Segalini, Prof. Alessandro Talamelli, Dr. Fredrik Lundell and all the people involved in the social activities at OB18 for the nice atmosphere they create.

Last - and not the least - *ringrazio la mia famiglia e tutte le persone care che non hanno mai fatto mancare il loro supporto.*

---

[1] including fresh, visiting and former members - I hope I remembered everybody!

Bibliography

Ahuja, S. 2009 Reduction methods for feedback stabilization of fluid flows. PhD thesis, Princeton University, New Jersey.

Anderson, B. & Moore, J. 1990 *Optimal control: Linear Quadratic Methods*. Prentice Hall, New York.

Arnoldi, W. E. 1951 The principle of minimized iterations in the solution of the matrix eigenvalue problem. *Quart. Appl. Math.* **9**, 17–29.

Aubry, N. 1991 On the hidden beauty of the Proper Orthogonal Decompositon. *Theoret. Comput. Fluid Dyn.* **2**, 339–352.

Bagheri, S. 2010 Analysis and control of transitional shear layers using global modes. PhD thesis, KTH Mechanics, Sweden.

Bagheri, S., Åkervik, E., Brandt, L. & Henningson, D. S. 2009*a* Matrix-free methods for the stability and control of boundary layers. *AIAA J.* **47**, 1057–1068.

Bagheri, S., Brandt, L. & Henningson, D. S. 2009*b* Input-output analysis, model reduction and control design of the flat-plate boundary layer. *J. Fluid Mech.* **620**, 263–298.

Bagheri, S., Hœpffner, J., Schmid, P. J. & Henningson, D. S. 2009*c* Input-output analysis and control design applied to a linear model of spatially developing flows. *Appl. Mech. Rev.* **62** (2).

Bewley, T. R. 2001 Flow control: New challenges for a new renaissance. *Progr. Aerospace. Sci.* **37**, 21–58.

Bewley, T. R., Moin, P. & Temam, R. 2001 Dns-based predictive control of turbulence: An optimal benchmark for feedback algorithms. *J. Fluid Mech.* **447**, 179–225.

Chevalier, M., Schlatter, P., Lundbladh, A. & Henningson, D. S. 2007 A pseudo spectral solver for incompressible boundary layer flows. Trita-Mek 7. KTH Mechanics, Stockholm, Sweden.

Choi, H., Moin, P. & Kim, J. 1993 Direct numerical simulation of turbulent flow over riblets. *J. Fluid Mech.* **255**, 503–539.

Doyle, J. C., Glover, K., Khargonekar, P. P. & Francis, B. A. 1989 State-space solutions to standard H_2 and H_∞ control problems. *IEEE Trans. Automat. Control* **34**, 831–847.

Dullerud, E. G. & Paganini, F. 1999 *A course in robust control theory. A convex approach*. Springer Verlag, New York.

Glad, T. & Ljung, L. 2001 *Control Theory - Multivariable and Nonlinear Methods*. Taylor and Francis, London, U.K.

Glover, K. 1984 All optimal Hankel-norm approximations of linear multivariable systems and the l^{∞}-error bounds. *Int. J. Control* **39**, 1115–1193.

Green, M. & Limebeer, J. N. 1995 *Linear Robust Control*. Prentice Hall, New Jersey.

Hammond, E. P., Bewley, T. R. & Moin, P. 1998 Observed mechanisms for turbulence attenuation and enhancement in opposition-controlled wall-bounded flows. *Phys. Fluids* **10** (9), 2421–2423.

Högberg, M., Bewley, T. R. & Henningson, D. S. 2003 Linear feedback control and estimation of transition in plane channel flow. *J. Fluid Mech.* **481**, 149–175.

Ilak, M. & Rowley, C. W. 2008 Modeling of transitional channel flow using balanced proper orthogonal decomposition. *Phys. Fluids* **20**, 034103.

Kalman, R. E. 1960 A new approach to linear filtering and prediction problems. *Trans. ASME, Ser. D. J. Basic Eng.* **82**, 24–45.

Kim, J. & Bewley, T. R. 2007 A linear systems approach to flow control. *Ann. Rev. Fluid Mech.* **39**, 383–417.

Laub, A., Heath, M., Paige, C. & Ward, R. 1987 Computation of system balancing transformations and other applications of simultaneous diagonalization algorithms. *IEEE Trans. Automat. Control* **32** (2), 115–122.

Lewis, F. L. & Syrmos, L. V. 1995 *Optimal Control*. John Wiley & Sons, New York.

Lundell, F. 2007 Reactive control of transition induced by free-stream turbulence: an experimental demonstration. *J. Fluid Mech.* **585**, 41–71.

Ma, Z., Ahuja, S. & Rowley, C. W. 2009 Reduced order models for control of fluids using the Eigensystem Realization Algorithm. *Theoret. Comput. Fluid Dyn.* In press.

Mezić, I. 2005 Spectral properties of dynamical systems, model reduction and decompositions. *Nonlinear Dynamics* **41** (1), 309–325.

Mezić, I. & Banaszuk, A. 2004 Comparision of systems with complex behavior. *Physica D: Nonlinear Phenomena* **197** (1-2), 101–133.

Monokrousos, A., Åkervik, E., Brandt, L. & Henningson, D. S. 2010 Global optimal disturbances in the blasius boundary-layer flow using time-steppers. *J. Fluid Mech.* **650**, 181–214.

Moore, B. 1981 Principal component analysis in linear systems: Controllability, observability, and model reduction. *IEEE Trans. Automat. Control* **26** (1), 17–32.

Quadrio, M. & Ricco, P. 2004 Critical assessment of turbulent drag reduction through spanwise wall oscillations. *J. Fluid Mech.* **521**, 251–271.

Rempfer, D. & Fasel, H. 1994 Evolution of three-dimensional coheren structures in a flat-plate boundary layer. *J. Fluid. Mech.* **260**, 351–375.

Rowley, C. W. 2005 Model reduction for fluids using balanced proper orthogonal decomposition. *Int. J. Bifurc. Chaos* **15** (3), 997–1013.

Rowley, C. W., Mezic, I., Bagheri, S., Schlatter, P. & Henningson, D. S. 2009 Spectral analysis of nonlinear flows. *J. Fluid Mech.* **641**, 115–127.

Ruhe, A. 1984 Rational Krylov sequence methods for eigenvalue computation. *Lin. Alg. Appl.* **58**, 391 – 405.

Saad, Y. 1980 Variations on Arnoldi's method for computing eigenelements of large unsymmetric matrices. *Lin. Alg. Appl.* **34**, 269–295.

Schmid, P. J. 2010 Dynamic Mode Decomposition. *J. Fluid Mech.* **656**, 5–28.

Schmid, P. J. & Henningson, D. S. 2001 *Stability and Transition in Shear Flows*. Springer Verlag, New York.

Semeraro, O., Bagheri, S., Brandt, L. & Henningson, D. S. 2010 Feedback control of three-dimensional optimal disturbances using reduced-order models. Submitted.

Sirovich, L. 1987 Turbulence and the dynamics of coherent structures i-iii. *Quart. Appl. Math.* **45**, 561–590.

Sturzebecher, D. & Nitsche, W. 2003 Active cancellation of tollmien–schlichting waves instabilities on a wing using multi-channel sensor actuator systems. *Int. J. Heat Fluid Flow* **24**, 572–583.

White, E. & Saric, W. 2000 Application of variable leading-edge roughness for transition control on swept wings. *AIAA Paper 2000-283, 38th AIAA Aerospace Sciences Meeting and Exhibit* .

Part II

Papers

Paper 1

Feedback control of three-dimensional optimal disturbances using reduced-order models

By Onofrio Semeraro, Shervin Bagheri, Luca Brandt & Dan S. Henningson

Linné Flow Centre, KTH Mechanics
SE-100 44 Stockholm, Sweden

Under revision - Journal of Fluid Mechanics

The attenuation of three-dimensional wavepackets of streaks and Tollmien-Schlichting (TS) waves in a transitional boundary layer using feedback control is investigated numerically. Arrays of localized sensors and actuators (about 10–20) with compact spatial support are distributed near the rigid wall equidistantly along the spanwise direction and connected to a low-dimensional ($r = 60$) LQG controller. The control objective is to minimize the disturbance energy in a domain spanned by a number of proper orthogonal decomposition (POD) modes. The feedback controller is based on a reduced-order model of the linearized Navier-Stokes equations including the inputs and outputs, computed using a snapshot-based balanced truncation method. To account for the different temporal and spatial behaviour of the two main instabilities of boundary layer flows, we design two controllers. We demonstrate that the two controller reduce the energy growth of both TS wavepackets and streak-packets substantially and efficiently, using relatively few sensors and actuators. The robustness of the controller is investigated by varying the number of actuators and sensors, the Reynolds number and the pressure gradient. This work constitutes the first experimentally feasible simulation-based control design using localized sensing and acting devices in conjunction with linear control theory in a three-dimensional setting.

1. Introduction

In recent years, industrial, economical and environmental needs have reinvigorated the interest in practical methods for control of transitional and fully turbulent wall-bounded shear flows. Currently, research efforts are devoted to the manipulation of fluids by passive means, for example by riblets (Choi *et al.* 1993) or discrete roughness elements (White & Saric 2000), by ad-hoc active means, for example via wave cancellation (Sturzebecher & Nitsche 2003), opposition control (Hammond *et al.* 1998) or wall-motion techniques (Quadrio & Ricco 2004) and with linear and nonlinear control theoretical approaches, for example using spatially localized convolution kernels (Högberg *et al.* 2003) or adjoint-based optimization methods (Bewley *et al.* 2001). Significant efforts are also devoted to the development of acting and sensing devices, such as synthetic jets (Smith & Glezer 1998), electro-magnetic actuators (Pang & Choi 2004), plasma actuators (Grundmann & Tropea 2008) or various micro-electro-mechanical systems (MEMS) actuators (Ho & Tai 1998) constructed using micro-machining techniques.

1.1. *Linear control of transition*

It is now well established that under certain conditions the initial phase of the laminar-turbulent transition in wall-bounded flows is largely governed by linear mechanisms. We therefore believe that tools of linear control theory may provide efficient, robust and feasible controllers to delay transition to turbulence. The combination of linear systems and control theoretical tools and transition control dates back to the seminal works by Joshi *et al.* (1997), Cortelezzi *et al.* (1998) and Bewley & Liu (1998) who paved the way for future researchers. These investigations applied feedback control to the problem of linearized plane Poiseuille flow, taking into account unknown and variable disturbances in imprecise flow conditions, mathematical modelling of boundary actuation (blowing and suction at the wall), optimality and robustness (LQG/H_∞ methods), minimal realizations (controllability and observability) and so on.

However, the tools in linear control theory are developed for systems with number of degrees of freedom of the order 10^2; controllers with 10^5 of states or more are of no interest in engineering applications due to the amount of hardware and computer resources required to compute a real-time control law. As a consequence, all model-based control designs involve the problem of reducing the order of the controller. In fact, this issue was already addressed by Cortelezzi *et al.* (1998); they analyzed distributed measurements and actuators and designed the linear controllers in Fourier space, since for spatially invariant systems such as channel flow, the 3D system becomes completely decoupled into a set of 2D subsystems. The approach requires an on-line 2D (for each xy-plane) FFT of the measurement vector and an online 2D iFFT of the control vector, in addition to assuming that the disturbances are spatially periodic in the spanwise direction. However, the main drawback besides the periodicity assumption, is that the cost of the online 2D FFTs grows rapidly with the number of actuators and sensors.

A different approach in physical space was adopted by Högberg & Bewley (2000) and Högberg *et al.* (2003), after the theoretical predictions by Bamieh *et al.* (2002). There, it was shown that for spatially invariant systems with distributed control and measurements, optimal and robust controllers, obtained by solving a set or family of smaller problems in the Fourier space, are spatially localized with compact support. This means that controllers designed in Fourier space for each wavenumber pair independently (considering for example the channel flow) result in realizable and practicable controllers (or kernels) in *physical space*, that can at least hypothetically be implemented using microelectromechanical systems (MEMS). Several successful projects were initiated to extend this approach to weakly spatially developing flows (Chevalier *et al.* 2007*a*; Monokrousos *et al.* 2008) and even to fully turbulent flows (Högberg *et al.* 2003*b*; Chevalier *et al.* 2006). However, there are several shortcomings of this approach which have rendered it difficult to implement it experimentally: (i) it introduces a controller with the same order as the plant; (ii) it is only applicable to spatially invariant systems; (iii) it assumes distributed sensors and actuators.

As we mentioned earlier, controllers of very high-order are useless in applications; today we lack methods to reduce the order of very high-dimensional controllers in a systematic way, since the methods developed in the control community are only applicable to moderate size controllers. The limitation to spatially invariant flows is a severe restriction; even if the approach can be extended to weakly spatially developing flows, more complex flows such as flows in ducts, corners, diffusers and around leading edges are out of reach. Finally, the assumption of distributed sensors and actuators restricts the approach to acting and sensing devices that can be manufactured in very large numbers such as MEMS devices; in many applications this is not cost-efficient and, moreover, only a few localized sensors and actuators suffice to manipulate the flow in a desired way.

1.2. *Model reduction of the Navier–Stokes equations*

This paper addresses the limitations – with no assumptions made about the geometry or about the shape and distribution of actuators and sensors – of previous methods in a direct and efficient way by reducing the complexity of the Navier–Stokes equations before designing the controller. For this model reduction step to be meaningful, the complexity of the governing system must be reduced by several orders of magnitude, that is, from several million degrees of freedom to less than a hundred, while preserving the essential dynamics. It has not been clear how to define “essential dynamics” in the context of transition control and once defined, if such an enormous order reduction can be performed in a systematic and efficient manner. The method used in this paper is balanced truncation. An approximation of this approach for large-scale systems, like those typical in fluid mechanics, was proposed by Rowley (2005) and recently applied for channel flow instabilities by Ilak & Rowley (2008).

As recognized by Bewley (2001), the only requirement to achieve the desired flow behavior is that suitable control signals are determined based only on filtered information delivered from the sensor measurement. Thus, of utmost importance for control design is to extract the components necessary to describe the relation among *time signals* from the full dynamics governed by Navier–Stokes equations. A general input-output framework was developed in Bagheri *et al.* (2009*a*), where the disturbance and actuators were considered as inputs, whereas the objective function and sensors were considered as outputs. It was shown that the input-output behavior is the "essential dynamics" and it could be represented equally well with a reduced-order model of 60 degrees of freedom as with the Navier–Stokes equations of order 10^5. This proof-of-concept work showed for the first time that this significant order reduction can be combined with control theoretical tools to attenuate disturbances in spatially developing flows. The work presented in this paper extends previous research on reduced-order models and linear feedback control of two-dimensional disturbances to a fully three-dimensional (3D) setting. This is not a trivial extension, since the third spatial direction introduces several new challenges; the disturbance dynamics is significantly more complex due to the presence and competition of different instability mechanisms.

When the background disturbance level is very low (order of 0.05%) packet of traveling waves, Tollmien-Schlichting (TS) waves, are typically observed in boundary layers. These waves are characterized by small streamwise scales and large spanwise extent. However, in the presence of moderate levels of vortical perturbations in the free stream, streaky streamwise elongated structures emerge in the boundary layer; these streaks have a dominant spanwise length scale on the order of the boundary layer thickness.

In addition to having completely different spatial structures, of these two disturbances types also evolve on different time scales. The TS wavepackets grow exponentially on a viscous time scale and break down when they reach amplitudes on the order of a few percent of the free stream velocity, whereas the streaks grow at an algebraic rate, quickly reaching their peak energy and triggering turbulence at amplitudes one order of magnitude larger than TS wavepackets. The two types of disturbances span a wide range of temporal and spatial scales, making the control design and in particular the choice of actuators and sensors and their placement a disturbance-dependent task. Indeed, previous work on flow control has targeted either streaks or TS wavepackets; however, in realistic conditions, it is likely that both instability mechanisms co-exist. In order to be able to control both types of disturbances we build two controllers: each aimed at one of the two types of instabilities. However, it is the intention of this work to control both type of disturbances using the same spatial shape of actuators and sensors.

1.3. *Scope of investigation*

The present study is based on a fully 3D configuration that resembles actual experimental setups – see for instance Lundell (2007) or Sturzebecher & Nitsche (2003) – with a set of localized actuators and sensors distributed near the wall. The long-term aim of this research project is to develop numerically reliable and fast controllers that are possible to use in laboratory experiments. For example, measurements from hot film sensors or wall wires could, after being processed by analog to digital converters (A/D) and digital signal processors (DSP), be fed to a computer that quickly computes the control signals using the numerically obtained low-order controller developed in this work. The control signal would then be converted to analog signal using D/A converter and fed to plasma actuators. Numerical investigations can also be useful for wind-tunnel experiments, by providing guidelines for the shape and spatial distribution of actuators and sensors. The design and placement of actuators and sensors can be studied through extensive numerical parametric studies, reducing the number of experiments required to obtain a satisfactory controller. Thus, we believe that the numerical study presented here takes us one step closer to incorporating theoretical tools into the practical (experimental) flow control community.

The objective of this work is to investigate whether three-dimensional streaks and TS wavepackets can be attenuated by specific controllers based on a few localized sensors and actuators. The controllers are designed using reduced-order models in conjunction with linear optimal feedback control. In addition, the efficiency and robustness of the linear controller will be investigated to assess the control performance when the system is operating at off-design conditions.

This paper is organized as follows. In sections 2 and 3, the control problem is formulated with a description of the configuration, disturbances, actuators, sensors and objective functions. The model reduction problem is briefly introduced. The characterization of the leading balanced modes and the validation of the reduced-order models of the Navier–Stokes system are provided in section 4. In this section, we start to discuss separately the results for streaks and TS-waves, while the previous theoretical formulation is independent of the specific disturbance considered. Section 5 provides a short introduction to the Linear Quadratic Gaussian (LQG) framework. Sections 6 and 7 contain the main results of the paper: the performance of the control is evaluated for 11 different configurations of sensors and actuators for the TS wavepackets case and 4 configurations for the streaks. The paper ends with a discussion in section 8 and a summary of the main conclusions (section 9).

2. Governing equations and flow parameters

We study the dynamics and control of small-amplitude perturbations in a viscous, incompressible flow over a flat plate, using numerical simulations. The three-dimensional input-output configuration, shown in figure 1, is an extension of the two-dimensional case studied in Bagheri *et al.* (2009*a*,*a*). The disturbance velocity field is governed by the Navier–Stokes equations linearized around a spatially evolving zero-pressure-gradient boundary layer flow $\mathbf{U}(\mathbf{x},t) = (U(x,y), V(x,y), 0)^T$,

$$\frac{\partial \mathbf{u}}{\partial t} = -\left(\mathbf{U}\cdot\nabla\right)\mathbf{u} - \left(\mathbf{u}\cdot\nabla\right)\mathbf{U} - \nabla p + Re^{-1}\nabla^2\mathbf{u} + \lambda_f(x)\mathbf{u} \qquad (1a)$$

$$0 = \nabla\cdot\mathbf{u} \qquad (1b)$$

$$\mathbf{u} = \mathbf{u}_0 \qquad at \quad t = 0. \qquad (1c)$$

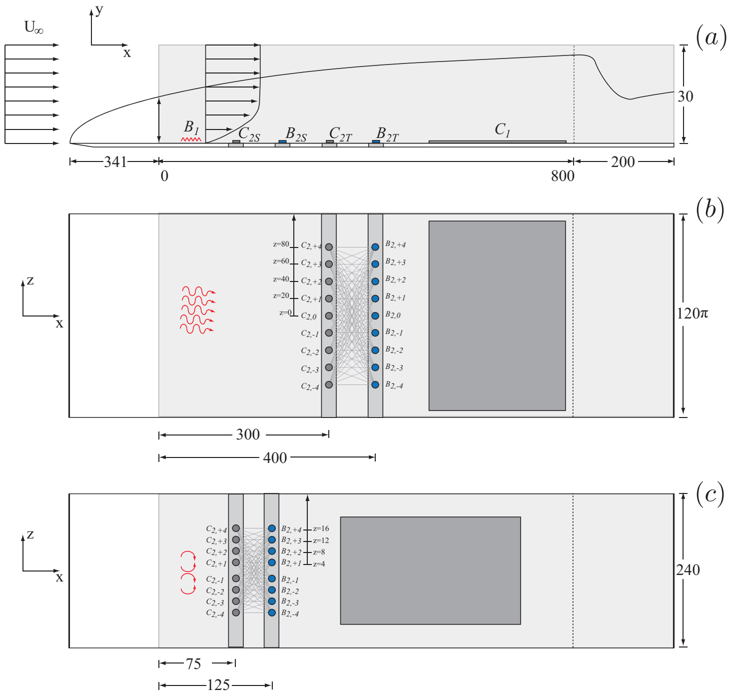

FIGURE 1. Input-output configurations. For a complete list of the cases, see table 1 and table 2; here, the reference cases for the TS case *(b)* and the streak case *(c)* are depicted. The input $\mathbf{B}_1$ in (b) is an optimal initial condition that triggers TS-waves, located at $(30, 1, 0)$. The control action is provided by the input $\mathbf{B}_2$, which consists of a row of actuators located at $x = 400$. The output $\mathbf{C}_2$ at $x = 300$ contains an array of sensors used for flow estimation. For the streak case (c), $\mathbf{B}_1$ is located at $(30, 1, 0)$, $\mathbf{B}_2$ at $x = 125$, and the estimation sensor row $\mathbf{C}_2$ is placed at $x = 75$. The effect of the controller is quantified by $\mathbf{C}_1$, defined in a region spanned by 10 proper orthogonal decomposition (POD) modes (here indicated with a darker gray region); for each case, one set of modes is generated. In both cases, all the estimation sensors are connected to all the actuators (*centralized control*).

The disturbance velocity field and the pressure field are $\mathbf{u}(\mathbf{x}, t) = (u, v, w)^T$ and $p(\mathbf{x}, t)$, respectively. The flow evolves in the spatial domain Ω defined by,

$$\Omega = \{\mathbf{x} \in \mathbb{R}^3 | x \in [0, L_x], y \in [0, L_y], z \in [-L_z/2, L_z/2]\},$$

where the streamwise, wall-normal and spanwise directions are denoted by x,y and z, respectively. The Reynolds number is defined as $Re = U_\infty \delta_0^*/\nu$, where

δ_0^* is the displacement thickness at the inflow position, U_∞ is the uniform freestream velocity and ν is the kinematic viscosity. The simulations were performed at $Re_{\delta_0^*} = 1000$, corresponding to $Re_x \approx 3 \times 10^5$ at the computational inlet.

The following boundary conditions are imposed in Ω,

$$\mathbf{u}(x, y, -L_z/2) = \mathbf{u}(x, y, L_z/2) \tag{2a}$$
$$\mathbf{u}(0, y, z) = \mathbf{u}(L_x, y, z) \tag{2b}$$
$$\mathbf{u}(x, 0, z) = \mathbf{u}(x, L_y, z) = 0. \tag{2c}$$

A no-slip condition is imposed on the flat plate ($y = 0$). Far away from the wall ($y = L_y$), in the freestream, Dirichlet boundary conditions enforce vanishing perturbations. Periodicity of the solution is assumed in the spanwise direction, whereas in the streamwise direction, an outflow boundary condition is imposed within the Fourier approximation by the term $\lambda_f(x)\mathbf{u}$ in equation (1*a*). This forcing is identically zero inside the physically relevant domain ($x \in [0, 800]$) and raises to order one inside a fringe region, starting at x=800, where it forces the perturbations to zero (Nordström *et al.* 1999).

In this work, our aim is to present the linear systems and control theory in as simple and compact form as possible and put the focus on the control performance and the associated physics. Therefore, we omit entirely any discussion of partial differential equations and the following analysis is presented for finite-dimensional systems – ordinary differential equations – for simplicity. The infinite-dimensional formulation of the theory is presented in Bagheri *et al.* (2009*a*), where the relevant function spaces, inner products and derivations of adjoint operators alongside a more in-depth theoretical discussion are provided. Note, however, that the fundamental difference between the theory for ODEs and PDEs is related to convergence (see e.g. Curtain & Zwart 1995); other than that, the two formulations are analogous.

The results presented in this paper are computed with a pseudo-spectral code (Chevalier *et al.* 2007). The computational domain Ω has the dimensions indicated in the captions of tables 1 and 2; a resolution of $768 \times 101 \times 120$ has been deemed sufficient and used for all the simulations. The spatial discretization requires thus $n \approx 10^7$ degrees of freedom. The discretized and linearized Navier–Stokes equations 1 with the boundary conditions 2 can be written as an initial-value problem

$$\dot{\mathbf{u}}(t) = \mathbf{A}\mathbf{u}(t) \qquad \mathbf{u}(0) = \mathbf{u}_0, \tag{3}$$

where $\mathbf{u} \in \mathbb{U} \subset \mathbb{R}^n$ is the state variable in the state space $\mathbb{U}$ endowed with the inner product $\langle \cdot, \cdot \rangle_\Omega$. For the flat-plate boundary layer, the flow is globally stable (Åkervik *et al.* 2008) – but convectively unstable – resulting in a stable matrix $\mathbf{A}$, *i.e.*, all the eigenvalues of $\mathbf{A}$ have negative real part.

The action of $\mathbf{A} \in \mathbb{R}^{n \times n}$ on $\mathbf{u}$ corresponds to evaluating the right-hand side of the linearized Navier–Stokes equations and enforcing the boundary conditions. Associated with this operator is the evolution operator $\mathbf{T}$, that can be

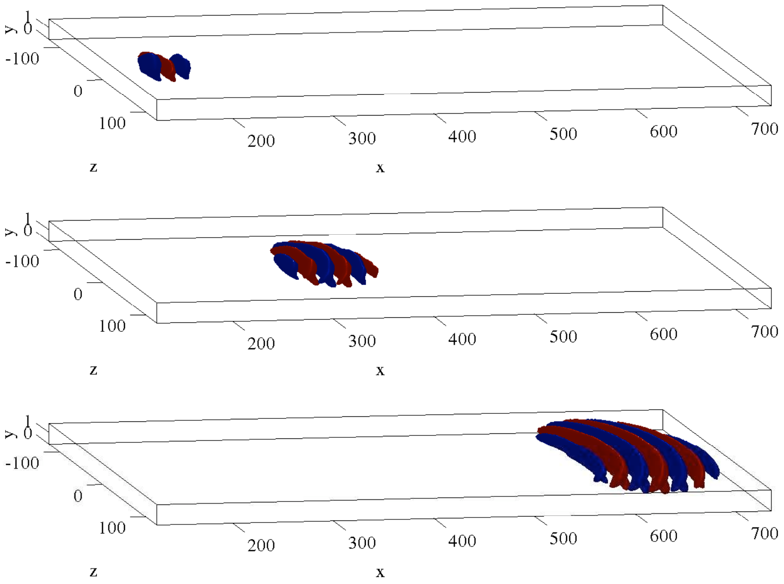

Figure 2. Impulse response of the system to an initial disturbance in $\mathbf{B}_1$, leading to maximum energy growth at time $T = 1820$; the streamwise component of the resulting disturbance is displayed at $t = 400, 800, 1600$. The red and blue colours represent positive and negative velocity, respectively. The spreading of a TS wave-packet is observed.

defined as

$$\mathbf{u}(t) = \mathbf{T}(t)\mathbf{u}(0) = \exp(\mathbf{A}t)\mathbf{u}_0. \tag{4}$$

Given an initial flow field $\mathbf{u}_0$, $\mathbf{T}$ provides the velocity field at a later time t; the action of the operator amounts to integrating the governing equations forward in time. In a similar way, the adjoint evolution operator $\mathbf{T}^*$ provides the solution of the adjoint linearized Navier–Stokes equations at different instants in time. Applying this operator corresponds to integrating the adjoint state backward in time. The continuous and discrete adjoint equations are given in Appendix Appendix B; a detailed derivation of the operators for the corresponding two-dimensional case is provided in Bagheri *et al.* (2009*a*).

3. Input-output system and model reduction

The input-output configuration is schematically depicted in figure 1; formally, the linear system with inputs and outputs is defined as follows:

$$\dot{\mathbf{u}}(t) = \mathbf{A}\mathbf{u}(t) + \mathbf{B}_1\mathsf{w}(t) + \mathbf{B}_2\phi(t), \tag{5a}$$
$$\mathsf{z}(t) = \mathbf{C}_1\mathbf{u}(t) + I_l\phi(t), \tag{5b}$$
$$\mathsf{v}(t) = \mathbf{C}_2\mathbf{u}(t) + I_\alpha\mathsf{g}(t). \tag{5c}$$

The first input $\mathbf{B}_1 \in \mathbb{R}^n$, located far upstream, models an incoming external perturbation, whereas the second input $\mathbf{B}_2 \in \mathbb{R}^{n\times m}$ represents m actuators. The temporal behaviour of the inputs is given by the signals $\mathsf{w} \in \mathbb{R}$, $\mathsf{g} \in \mathbb{R}$ and $\phi \in \mathbb{R}^m$ respectively. The measurement signals, contained in the vectors $\mathsf{v} \in \mathbb{R}^p$ and $\mathsf{z} \in \mathbb{R}^k$, provide information about the perturbation and are extracted by p sensors $\mathbf{C}_2 \in \mathbb{R}^{p\times n}$ and k sensors $\mathbf{C}_1 \in \mathbb{R}^{k\times n}$, respectively. To model measurement noise corrupting the sensors signals, the output equation (5b) is forced with unit-variance white noise $\mathsf{g}(t)$. The vector $I_\alpha \in \mathbb{R}^p$ contains in each entry the scalar value α. A large value of α introduces a high level of noise corruption on the measurement $\mathsf{v}(t)$, whereas a small value indicates high fidelity of the information extracted by the sensors $\mathbf{C}_2$. Finally, the matrix $I_l \in \mathbb{R}^{k\times m}$ contains in each entry the parameter l, which allows penalization of the controller effort, as further discussed in section 3.3.

The energy growth of the TS wavepacket and the streaks is characterized by different growth rates and temporal scales: whereas the TS wavepacket grows at an exponential rate and breaks down quite far downstream of the inflow, the streaks grow at an algebraic rate, quickly reaching the maximum level of energy and resulting in a relatively early breakdown. The different time scales of the disturbances have vital implications for the control design as shown in figure 1; in order to mitigate properly the two types of disturbances, a proper control scheme for each case is designed. The set-up designed for the mitigation of the streaks is located upstream in the domain, before the maximum growth is reached. Conversely, the location of the TS wavepacket controller is chosen in the center of the box, since the maximum growth appears far downstream. In the following sections, the $m+1$ inputs and $p+k$ outputs are introduced in detail.

3.1. $\mathbf{B}_1$ — *Optimal disturbances*

The upstream disturbance $\mathbf{B}_1$ is a localized initial condition that provides the maximum energy of the perturbation at a given final time. As recently shown by Monokrousos *et al.* (2010), different instability mechanisms can be triggered by three-dimensional, localized initial conditions computed for different optimization times. In particular, long optimization time provides an initial condition that triggers a wavepacket of Tollmien-Schlichting waves, whereas streamwise vortices are obtained as an optimal initial condition when large amplification in short time is sought.

Figure 2 shows the impulse response to an initial condition $\mathbf{B}_1$ that provides the maximum growth for a final time $t_{max} \approx 1820$ at three instants in time; the streamwise component is tilted in the upstream direction, leaning against the shear layer. Initially, the evolving disturbance extracts energy from the mean

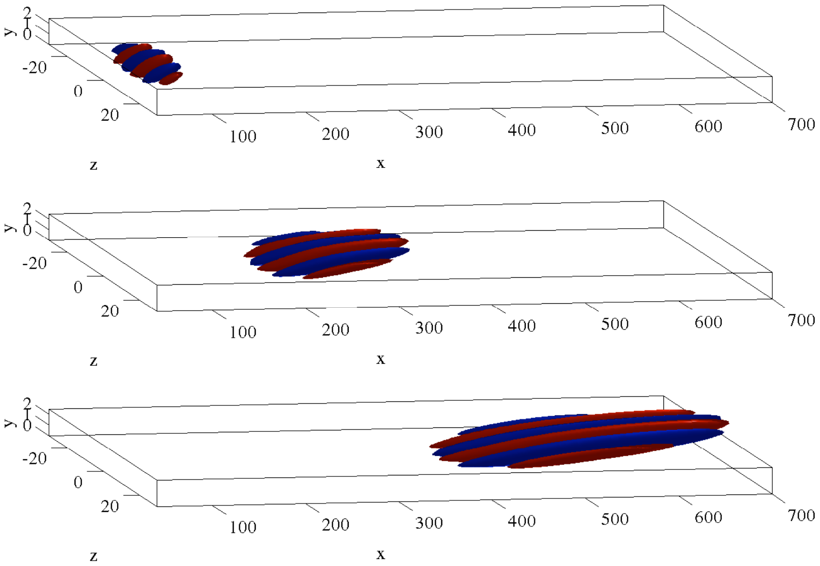

Figure 3. Impulse response to an optimal initial disturbance in $\mathbf{B}_1$ leading to maximum energy growth at $T = 720$. The disturbances is represented by the iso-surfaces of the streamwise velocity at $t = 100, 400, 800$; the red and blue colours represent positive and negative velocity, respectively. The resulting disturbance is characterized by elongated streaky structures.

flow via the Orr-mechanism (see e.g. Butler & Farrell 1992; Åkervik *et al.* 2008); the structure gradually rotates until it aligns with the shear. As the disturbance propagates downstream, the wavepacket grows in size and spreads in the spanwise direction. The evolution of the disturbance energy, defined as,

$$E(t) = \langle \mathbf{u}(t), \mathbf{u}(t) \rangle_\Omega \tag{6}$$

is shown in figure 4(*a*). We observe an exponential growth of the energy and an amplification $E(t_{max})/E(0) \approx 2 \times 10^3$.

The evolution of the optimal initial condition obtained for a shorter time, $t_{max} = 720$, is depicted in figure 3. The initial condition is a packet of streamwise vortices, with most of the energy contained in the wall-normal and spanwise components. The energy growth is related to the lift-up mechanism, characterized by the energy transfer to the streamwise component; this instability mechanism generates long streaky structures, growing in size in the streamwise direction, as shown in figure 3. The energy evolution is shown in figure 4(*b*), where an amplification $E(t_{max})/E(0) \approx 3 \times 10^2$ is found.

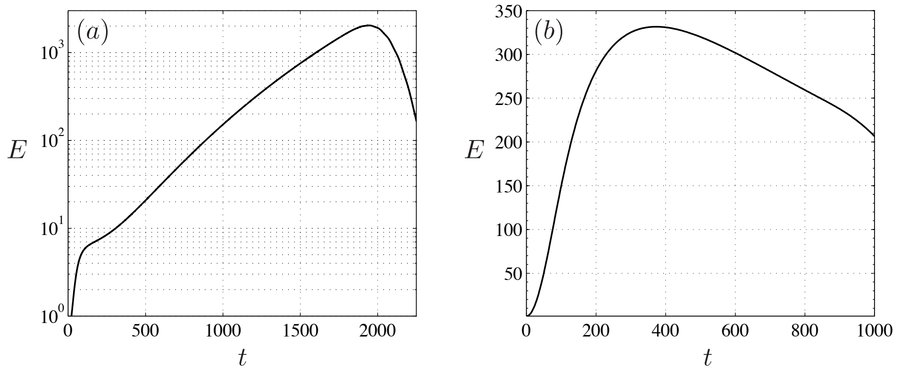

FIGURE 4. Disturbance energy as function of time for the TS-waves (*a*) and streaks (*b*).

3.2. $\mathbf{B}_2$ *and* $\mathbf{C}_2$ – *Actuators and sensors*

Each of the m actuators in $\mathbf{B}_2$ is represented by a volume forcing localized in a region close to the wall. The actuators are placed in a row in the spanwise direction; the p sensors represented by $\mathbf{C}_2$ are also composed by a row of localized elements, located a short distance upstream of the actuators. All the elements in $\mathbf{B}_2$ and $\mathbf{C}_2$ are analytically expressed by a Gaussian function given in Appendix Appendix A. The fact that we have modeled the actuators and sensors as volume forcing does not mean that they are unrealistic or not relevant for practical implementation; it is the effect of an actuator that is important to model, and not the actuator itself. Therefore, the action that the volume forcing has on the flow, could possibly be reproduced for example using plasma actuators (Grundmann & Tropea 2008). The measurement signal $\mathsf{v}(t)$ is the spatial integral of the velocity field $\mathbf{u}$ weighted with the Gaussian function (see equation 22).

The actuator array designed for the mitigation of the TS-wavepackets is located halfway in the downstream direction, while the array designed for the streaks control is placed upstream; it was found by numerical simulations that the performance of the feedback control schemes is dependent on the number of elements used and the streamwise location, as discussed later.

3.3. $\mathbf{C}_1$ – *Objective function*

The aim is to determine a control signal $\phi(t)$ using the noisy measurements $\mathsf{v}(t)$, so that the perturbation energy of the flow is minimized in the region defined by $\mathbf{C}_1$. Moreover, the energy expended by the actuator has to be limited in order to design an efficient controller. Hence, the criterion to be minimized is

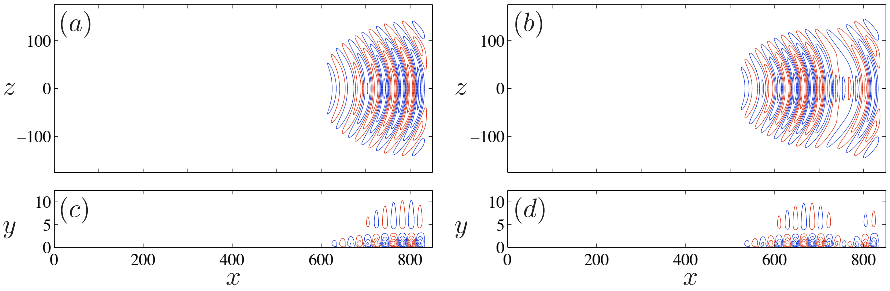

Figure 5. POD modes generated from the impulse response to an initial condition triggering TS-waves. The isocontours of the streamwise velocity component of the first mode ($\mathbf{C}_{1,1}$) are shown in the xz-plane at $y \approx 1.0$, (a), and in the xy-plane at $z = 0$, (c); red contours indicate positive velocity, blue contours the negative one. Analogously, the third POD mode ($\mathbf{C}_{1,3}$) is shown in the right frame.

expressed by the objective function

$$\|\mathsf{z}\|^2_{L^2(0,T)} = \int_0^T \|\mathbf{C}_1\mathbf{u}\|^2_\Omega + \phi^T I_l^T I_l \phi \, \mathrm{d}t \tag{7}$$

where the entries of the matrix I_l, given by the parameter l, define the cost of the control[1]. Low values of l allow strong actuations, as the control input is allowed to have a higher magnitude. On the other hand, high values of l penalize strong actutation. Also, it is worth noting that values of l that are too low may result in unphysical control inputs.

The spatial support for $\mathbf{C}_1$ is localized in a region downstream, where disturbances have high energy, as sketched in figure 1. The subspace of the domain where the controller minimizes the energy is spanned by a basis $\{\mathbf{C}_{1,1}, \ldots, \mathbf{C}_{1,k}\}$, which in the present configurations is a sequence of POD modes (see e.g. Holmes *et al.* 1996), obtained from the impulse response of the initial disturbances. This approach is similar to the so-called "output projection" technique used by Rowley (2005) and Ilak & Rowley (2008). The POD modes are the most energetic structures triggered by the inputs; the corresponding eigenvalues $\{\gamma_1 \geq \gamma_2 \geq \cdots \geq \gamma_k\}$ represent the fraction of the total flow energy captured by each mode.

The POD basis is empirical, *i.e.*, it accurately represents the data that generated it; therefore, two different sets of modes are computed, one for each initial condition considered. The POD modes generated for the TS-wavepacket configuration come in pairs (see e.g Rempfer & Fasel 1994), because

---

[1] It is assumed that the cross-term between the control input and $\mathbf{C}_1\mathbf{u}$ is zero (Zhou *et al.* 2002).

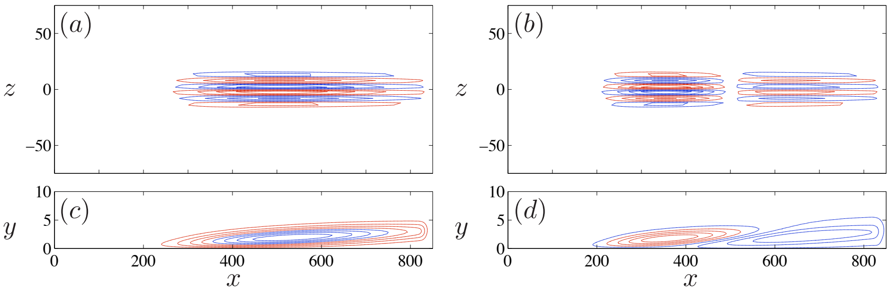

FIGURE 6. POD modes generated from the impulse response to an initial condition triggering streaks. The isocontours of the streamwise velocity component of the first ($\mathbf{C}_{1,1}$) and second ($\mathbf{C}_{1,2}$) POD modes are shown in left and right frame, respectively; the sections in the xz-plane, at $y \approx 1.6$, are shown in (a) and (b), whereas the sections in the xy-plane, at $z = 2$, are shown in (c) and (d). Red contours indicate positive velocity, blue contours indicate negative velocity.

two real-valued functions are required to describe a flow structure travelling as a wavepacket; each pair exhibits the same structure, only shifted in the streamwise direction. In contrast, the corresponding POD eigenvalues associated with the streak disturbance - not shown here - are no longer ordered in pairs, since the disturbance is characterized by low frequency elongated structures in the direction of propagation.

To identify a proper POD basis, we also considered snapshots generated from all the inputs (*i.e.* including the actuators). The comparison between the POD modes generated by all the inputs ($\mathbf{B}_1$ and $\mathbf{B}_2$) and those obtained from the initial condition ($\mathbf{B}_1$), demonstrated that only modes corresponding to small γ, containing less than 1% of the total energy, are affected by the structures related to the actuators. Thus, POD modes generated only by the upstream disturbance were used during the numerical simulation; in particular, the first 10 POD modes capture 93% and 91% of the total flow energy for the TS and streak configurations, respectively, and are used as the basis for C_1. An alternative choice for $\mathbf{C}_1$ is presented in Semeraro *et al.* (2010), where a set of Fourier modes localized in the streamwise and wall-normal directions were introduced to define the objective function.

The leading POD modes capture the relevant spatial characteristics of each disturbance as illustrated in figure 5 and 6, where two modes for each set are shown. For the TS wavepacket (figure 5), one POD mode for each of the two first pairs is shown: it can be seen that the structure is mostly located downstream, indicating where the energy response to the forcing is the largest. For the streaks (figure 6), the first two modes have significant spatial support starting from $x = 250$ and extend all the way to the end of the domain. The streamwise and the wall-normal components are anti-symmetric with the respect of the xy-plane ($z = 0$), whereas the spanwise component is symmetric; opposite symmetry features are observed for the TS wavepackets. The cross section reveals the tilted shape of the modes, with the streak leading edge further away from the wall then the trailing edge.

3.4. *Model Reduction*

In general, a reduced-order model of the input-output system 5 can be obtained via a projection onto a low-dimensional subspace $\mathbb{U}_r \subset \mathbb{U}$, spanned by r basis functions, $\mathbf{\Phi} = (\boldsymbol{\phi}_1, \boldsymbol{\phi}_2, \dots, \boldsymbol{\phi}_r) \in \mathbb{R}^{n\times r}$. Thus, the disturbance field $\mathbf{u} \in \mathbb{U}$ can be approximated by $\tilde{\mathbf{u}} \in \mathbb{U}_r$,

$$\tilde{\mathbf{u}} = \sum_{j=1}^{r} q_j \boldsymbol{\phi}_j = \mathbf{\Phi} q \tag{8}$$

where $q = (q_1, q_2, \dots, q_r)^T \in \mathbb{R}^r$ are the scalar expansion coefficients. The coefficients can be computed from

$$q_j = \langle \mathbf{u}, \boldsymbol{\psi}_j \rangle_\Omega, \quad \text{or} \quad q = \mathbf{\Psi}^* \mathbf{u}$$

where $\mathbf{\Psi} = (\boldsymbol{\psi}_1, \boldsymbol{\psi}_2, \dots, \boldsymbol{\psi}_r) \in \mathbb{R}^{n\times r}$ are adjoint modes; the adjoint modes are bi-orthogonal to the expansion basis $\mathbf{\Phi}$, *i.e.* $\mathbf{\Psi}^*\mathbf{\Phi} = \mathbf{I}$, where $\mathbf{I} \in \mathbb{R}^{r\times r}$ is the identity matrix. The superscript * represents the application of the inner-product $\langle \cdot, \cdot \rangle_\Omega$ between the rows of $\mathbf{\Psi}^*$ and $\mathbf{u}$. The approximation 8 can be inserted in the input-output system 5. Taking the inner product with the adjoint modes results in the reduced-order model of order r,

$$\dot{q}(t) = Aq(t) + B_1 \mathsf{w}(t) + B_2 \phi(t) \tag{9a}$$

$$\mathsf{z}(t) = C_1 q(t) + I_l \phi(t) \tag{9b}$$

$$\mathsf{v}(t) = C_2 q(t) + I_\alpha \mathsf{g}(t), \tag{9c}$$

where $A = \mathbf{\Psi}^*\mathbf{A}\mathbf{\Phi}$, $B_1 = \mathbf{\Psi}^*\mathbf{B}_1$, $B_2 = \mathbf{\Psi}^*\mathbf{B}_2$, $C_1 = \mathbf{C}_1\mathbf{\Phi}$ and $C_2 = \mathbf{C}_2\mathbf{\Phi}$.

The choice of a proper expansion basis is crucial for the performance of the reduced-order model; in our case, we aim to build a model that preserves the dynamics between the actuators and sensors. Indeed, among all the possible divergence-free velocity fields, only certain states can be triggered by the inputs ($\mathbf{B}_1$ and $\mathbf{B}_2$) and observed by the outputs ($\mathbf{C}_1$ and $\mathbf{C}_2$). These states are called *controllable* and *observable* states, respectively. The unobservable/uncontrollable states are redundant for the input-output behaviour of the system; thus, they can be discarded. Moreover, it turns out that, when $m, p \ll n$, with m the number of inputs and p the number of the outputs, the complexity of 5 can be further reduced, while preserving the relation between the inputs and outputs.

A systematic approach of removing these states is called *balanced truncation* (Moore 1981); in appendix Appendix C a summary of this method is given in a simplified space-discrete form. The focus is on the Hankel operator, which provides a direct mapping between the inputs and the outputs. From this operator a set of *balanced modes* and a corresponding adjoint set can be defined, and used as a projection basis. Unfortunately, the necessity to solve Lyapunov equations makes the exact balanced truncation unfeasible for large systems. An approximation based on snapshots of the flow field is introduced in Rowley (2005). In particular, the snapshots are computed by marching in time the linearized NS forced by all inputs, and backward in time the adjoint system forced by the sensors. In appendix Appendix C, the method is briefly outlined for the present notation; note, however, that the original method proposed by Rowley (2005), also referred as *balanced proper orthogonal decomposition* (BPOD), is characterized by the *output projection* of the sensor over a POD basis generated from the inputs dataset.

Further extensions of balanced truncation are available for unstable systems and nonlinear problems. Indeed, a balanced truncation as introduced by Moore (1981) can be applied only to a system linearized about a stable steady state. An extension to unstable cases was proposed by (Zhou *et al.* 1999); the method relies on the identification of the stable and the unstable states, for instance via a modal decomposition, and the application of balancing to those subspaces. Recently, the method was applied using the snapshot-based approximation for the control of unstable flows such as the open cavity case (Barbagallo *et al.* 2009) or the flow past a flat plate (Ahuja & Rowley 2010); in those cases, the unstable dynamics of the system is represented by the unstable modes, while the approximate balance truncation is applied to obtain a reduced-order model of the stable partition of the system. Finally, an interesting application to nonlinear systems is presented in Ilak *et al.* (2010), where reduced-order models for the complex Ginzburg-Landau equation are compared. The best performance is obtained by Galerkin projection of the nonlinear system onto a basis of balanced modes obtained from the corresponding linearized system.

4. Reduced-order models

In this section, we discuss the set of approximate balanced modes - and the related adjoint set - computed for both the TS and streaks cases. The structure of the modes is investigated, pointing out the main structural features. Indeed, an advantage of this technique is the possibility of analysing the spatial distribution of the modes; the spatial support reveals peculiarities of the flow from the input-output point of view and provides physical insight for the sensors/actuators placement. In fact, the resulting balanced mode $\boldsymbol{\phi}_j$ is the global structure in the flow that is "influenced" by the input $\mathbf{B}$ by an amount given by its Hankel Singular Value (HSV) – see appendix Appendix C. The corresponding adjoint mode $\boldsymbol{\psi}_j$ is a flow structure that – if used as an initial condition – will result in an output energy given also by its HSV. Thus, these global modes represent flow fields ranked according to their response behavior (controllability) and output sensitivity (observability).

Case	Act.s m	Sens.s p	Control l	Noise α	Energy E/E_{nc}	System norm $\|\mathbf{G}\|_2^2$
Ts0	-	-	-	-	1.00	324.25
A	9	9	100	0.01	0.070	1.42
B	9	9	250	0.01	0.064	13.23
C	9	9	500	0.01	0.12	55.27
D	9	9	100	10	0.068	1.48
E	9	9	100	50	0.061	8.46
F	9	9	100	150	0.57	209.03
G	9	9	100	250	0.85	318.74
H	3	3	100	0.01	0.55	6.91
I	5	5	100	0.01	0.13	2.25
L	7	7	100	0.01	0.071	1.28
M	9	5	100	0.01	0.068	1.56

TABLE 1. Cases A-M correspond to 11 closed-loop systems for the control of TS-wavepacket, whereas case '$Ts0$' is an uncontrolled configuration. In all the cases the computational box Ω has dimensions $[L_x, L_y, L_z] = (100, 30, 120\pi)$. The number of actuators $\mathbf{B}_2$ (m), the number of sensors $\mathbf{C}_2$ (p), the control penalty (l) and the degree of noise corruption (α) vary for the different configurations. The peak perturbation energy of the controlled cases as a fraction of the uncontrolled peak disturbance energy, together with the 2-norm of the input-output system transfer function are also displayed.

In this section, we first discuss the balanced modes obtained by considering only the upstream disturbance $\mathbf{B}_1 \in \mathbb{R}^n$ and the outputs $\mathbf{C}_1 \in \mathbb{R}^{k\times n}$ (POD modes), for the sake of clarity. Finally, the reduced-order models for the full system, including also the actuators $\mathbf{B}_2 \in \mathbb{R}^{n\times m}$ and sensors $\mathbf{C}_2 \in \mathbb{R}^{p\times n}$, are presented and their performance is analysed. One model is computed for each configurations; in table 1, 11 different configurations (labeled A to M) for the TS mitigation, are listed. In all cases, the elements have an equidistant spacing in the spanwise direction at $\Delta_z = 20$. The relative position of the arrays in the streamwise direction is fixed; the distance among the actuators was chosen after preliminary tests to get a proper actuation. For the streaks, we found that a finer distribution, $\Delta_z = 4$, of the actuator elements in the spanwise direction is necessary. This is mainly due to the smaller spanwise scales of the streaks ($\beta = \frac{2\pi}{L_z} = 0.58$, with a total width of $L_z \approx 11$). In table 2 the configurations for the control of streaks are listed, labeled N to Q. For the largest cases, the linear systems consist of 10 inputs and 19 outputs (case A, table 1), and 9 inputs and 18 outputs (case N, table 2); their complexity n is of order 10 million.

Case	Act.s m	Sens.s p	Control l	Energy Ratio E/E_{nc}	System norm $\|\mathbf{G}\|_2^2$
Sk0	-	-	-	1.00	114.24
N	8	8	50	0.66	38.84
O	8	8	100	0.67	79.85
P	8	8	150	0.81	96.40
Q	8	8	70	0.79	55.96

TABLE 2. Cases N-Q correspond to 4 closed-loop systems for the control of streaks, whereas case '$Sk0$' is an uncontrolled configuration. The control penalty (l) varies for the different configurations; the measurement noise is $\alpha = 0.01$ for all setups. The same number (m) of actuators $\mathbf{B}_2$ (m) and sensors $\mathbf{C}_2$ (p) is considered for all the configurations; in the last configuration, a different layout is considered, where the sensor array and the actuator array are placed in $x = 100$ and $x = 150$, respectively. The dimensions of the computational domain for all the cases are $[L_x, L_y, L_z] = (1000, 30, 240)$. The peak perturbation energy of the controlled cases as a fraction of the uncontrolled peak disturbance and the 2-norm are reported.

The TS case and the streaks are discussed separately in the following sections.

4.1. *TS wavepackets*

Using the snapshot method, the balanced modes and the adjoint balanced modes related to the TS wavepacket were computed; the snapshots were collected with constant time spacing, $\Delta t = 16$, in a time-interval $[0, 3000]$ for the forward simulation and in $[0, -2600]$ for the ten adjoint simulations.

The computed Hankel singular values σ_j are shown in figure 7 (red circles). Similarly to the POD modes discussed previously, the HSVs generated for the TS come in pairs, where the corresponding modes have the same structure, only shifted along the streamwise direction by a quarter of wavelength. The iso-contours of the streamwise components of the first and the third balanced modes ($\boldsymbol{\phi}_1, \boldsymbol{\phi}_3$) and their related adjoint modes ($\boldsymbol{\psi}_1, \boldsymbol{\psi}_3$) are shown in figure 8; the structure is shown in both the xy-plane ($z = 0$) and the xz-plane ($y \approx 1.6$). The leading balanced modes are characterized by a nearly two-dimensional TS-wavepacket structure, located mostly in the downstream region. These modes are strongly controllable flow structures and capture the response behavior of the system to the input $\mathbf{B}_1$.

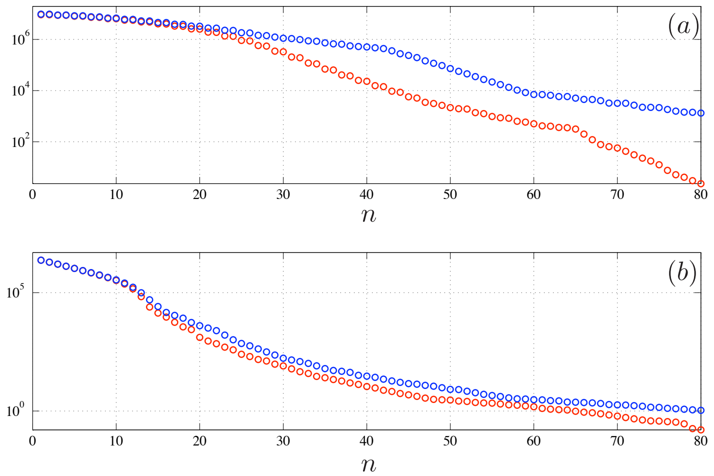

Figure 7. The Hankel singular values of the complete models (blue circles) are compared with the HSVs generated considering the first input $\mathbf{B}_1$ and the output $\mathbf{C}_1$ only (red circles). On top Hankel singular values generated for the models related to TS waves (a), on bottom HSVs for the streaks (b).

The associated adjoint balanced modes are mostly located far upstream and represent flow structures to which the output $\mathbf{C}_1$ is most sensitive. The spatial separation between these structures and the most controllable structures identified by the direct balanced modes is similar to the spatial separation observed between the direct and adjoint global modes of the linearized Navier–Stokes equations, $\mathbf{A}$. This is a sign of the streamwise non-normality of $\mathbf{A}$ (Chomaz 2005). In figure $8(b-d)$, the streamwise component of the modes in the xy-plane $(z = 0)$ is shown. Here one can see a tilted structure leaning against the shear, similarly to the optimal initial condition discussed in section 3.1.

Figure 7 shows the HSVs corresponding to the balanced modes used to compute the reduced-order model using all the inputs $(m + 1)$ and all the outputs $(p + k)$ (blue circles), pertaining to Case A in table 1. It is interesting to note that the associated HSVs decay slower than the HSVs computed using only $\mathbf{B}_1$ and $\mathbf{C}_1$ (open circles). The leading singular values of the two systems are equal, indicating that the input-output dynamics of the system is strongly influenced by the energy triggered by the input $\mathbf{B}_1$ and the observability characteristics of the functions chosen as output $\mathbf{C}_1$.

One way to validate snapshot-based balanced truncation is to check whether the controllability and observability Gramians of the ROM are diagonal and equal to the HSVs. The diagonal elements of the Gramians associated with the reduced-order model and the HSVs were found to be the same for the first 80 modes. Due to numerical discretization errors, higher order modes gradually lose bi-orthogonality, causing the presence of off-diagonal elements in the Gramians.

To test the reduced-order model, we compare impulse responses of the Navier–Stokes system 5 to impulse responses obtained from the low-order model 9. For configuration A, there are in total 10 input signals and 19 output signals, resulting in 190 impulse responses. In figure 9, the following three signals are shown

$$\mathbf{B}_1 \to \mathbf{C}_{2,0}, \qquad \mathbf{B}_{2,0} \to \mathbf{C}_{1,1}, \qquad \mathbf{B}_1 \to \mathbf{C}_{1,1}. \tag{10}$$

The second subscript of $\mathbf{B}_2$ and $\mathbf{C}_2$ indicates the element according to figure 1. In all the figures, the impulse responses of a reduced model of order $r = 60$ are shown with gray dots, while the solid red line provides the DNS results. We observe that the low-order model ($r = 60$) is able to preserve the input-output behaviour of the full Navier–Stokes system ($n \approx 10^7$), albeit the significant model order reduction. The agreement between all the impulse responses of the two systems is as good as the three signals shown here.

4.2. *Streaks*

The approximate Hankel singular values generated for the streak case are shown in figure 7(*b*). In this case, the snapshots were collected with a constant time spacing, $\Delta t = 16$, in a time interval $[0, 3000]$ for the forward simulation and a time interval $[0, 2000]$ for the 10 adjoint simulations. In agreement with the POD results, the HSVs do not come in pairs, due to the low–frequency elongated structure characterizing the modes (see figure 10). The first two balanced modes resemble the POD modes depicted in figure 6 and shows the typical structure aligned with the shear, in the xy section at $z \approx 3.1$. The streamwise velocity component u is one order of magnitude larger than v and w. The corresponding leading adjoint modes shown in the right column of figure 10 are located slightly more upstream and have an order of magnitude large value in v, w compared to u. Note that the spatial support of the balanced modes and the corresponding adjoint modes is nearly the same; the significant difference between the forward and adjoint modes is in the dominant velocity component. This is a sign of component-wise non-normality; the most efficient mechanism of growth of a streak is energy transfer from the wall-normal and spanwise component to the streamwise component.

As shown in figure 7(*b*) – similar to the case of the TS wavepacket – the HSVs of the complete system (including all inputs and outputs) decay slower than the HSVs computed using only $\mathbf{B}_1$ and $\mathbf{C}_1$ (blue circles) and the leading singular values of the two systems are equal.

A low-order model ($r = 60$) computed using balanced modes captures properly the input-output behaviour of the entire system ($n \approx 10^7$). The validation of the snapshot-based balanced truncation method and the properties of the reduced-model were tested following the same steps as for the TS reduced-order

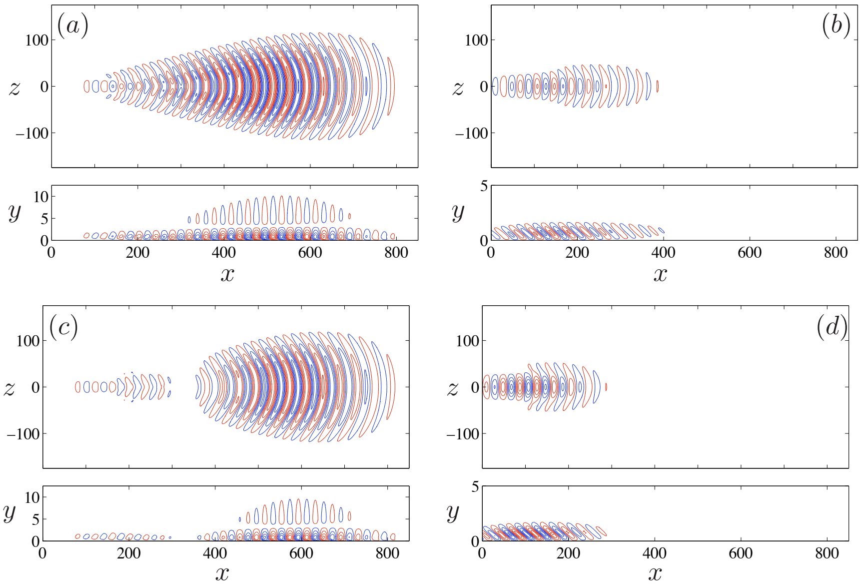

FIGURE 8. Balanced modes and related adjoint modes for the TS waves. Left column: streamwise component of the leading balanced mode $\boldsymbol{\phi}_1$ (*a*) and the third balanced order mode $\boldsymbol{\phi}_3$ (*c*). Right column: corresponding adjoint modes $\boldsymbol{\psi}_1$ (*b*) and $\boldsymbol{\psi}_3$ (*d*). Positive velocity is represented in red, while negative one is in blue; for all the modes depicted here, the top view is shown in the xz-plane at $y \approx 1.6$, the side view is in the section xy at $z = 0$.

model. In figure 11, we compare the input-output behaviour of the full Navier-Stokes system and the reduced-order model, for the following three signals,

$$\mathbf{B}_1 \rightarrow \mathbf{C}_{2,-1}, \qquad \mathbf{B}_{2,-1} \rightarrow \mathbf{C}_{1,1}, \qquad \mathbf{B}_1 \rightarrow \mathbf{C}_{1,1}. \tag{11}$$

The second subscript of $\mathbf{B}_2$ and $\mathbf{C}_2$ indicates the element according to figure 1. A similar good agreement is observed for all the impulse responses, and we can conclude that input-output relation of the signals for the streak configuration can be adequately described with a low-dimensional model.

5. Feedback control

The aim of this section is to use the validated balanced reduced-order models to mitigate the growth of the disturbances. Although the steps taken to design the closed-loop control are the same as for the two-dimensional case studied by Bagheri *et al.* (2009*a*), the control problem is significantly more complex due to the additional spanwise direction.

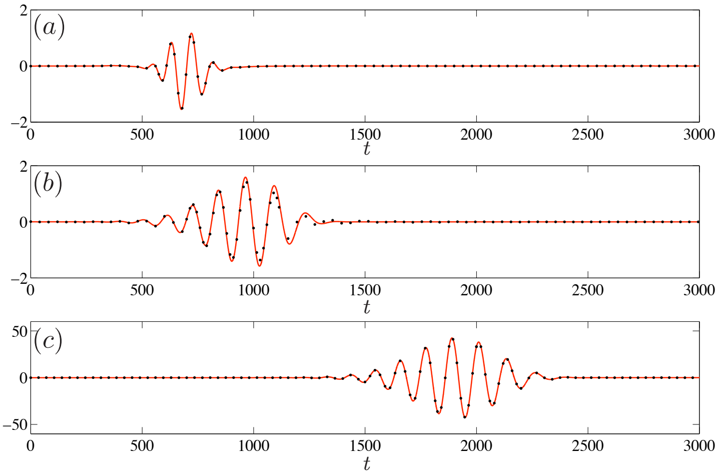

FIGURE 9. Impulse response of the system from the input $\mathbf{B}_1$ to the output $\mathbf{C}_{2,0}$, (*a*), from $\mathbf{B}_{2,0}$ to $\mathbf{C}_{1,1}$, (*b*) and from $\mathbf{B}_1$ to $\mathbf{C}_{1,1}$, (*c*), when a propagating TS wavepacket is considered. The red line shows the DNS results, while the gray dots indicate the impulse response of a reduced model of order 60.

Since the reduced-order models show essentially the same input-output behavior as the original system (but with only 60 degrees of freedom), they are used during the control design. Once the feedback controller is constructed, it can be applied on-line, in parallel to the DNS-simulations.

5.1. *Main steps of LQG design*

Using the tools of control theory, we can determine what action the actuators should take to minimize the disturbance energy in a region defined by $\mathbf{C}_1$, and if the action of an actuator should depend on all sensor measurements or only the sensor located upstream at the same spanwise location. In particular, the controller can be designed using the linear quadratic Gaussian (LQG) approach. Assume that the external disturbance signal $\mathsf{w}(t)$ and the measurement noise $\mathsf{g}(t)$ in 9 are unit-variance white noise processes. Then based on the noisy measurements $\mathsf{v}(t)$ extracted from the sensors $\mathbf{C}_2$, the controller provides a control signal $\phi(t)$ for the actuators $\mathbf{B_2}$, such that the mean of the output energy of z

$$\mathcal{E}\left\{\|\mathsf{z}\|^2_{L^2[0,\infty)}\right\} = \mathcal{E}\left\{\int_0^\infty q^T C_1^T C_1 q + \phi^T I_l^T I_l \phi \ \mathrm{d}t\right\}. \tag{12}$$

is minimized. The first step in constructing a controller is to estimate the full state $\mathbf{u}$ given only the noisy measurements $\mathsf{v}(t)$ - also referred as the *estimation problem*. After the state has been successfully estimated, we assume, in a

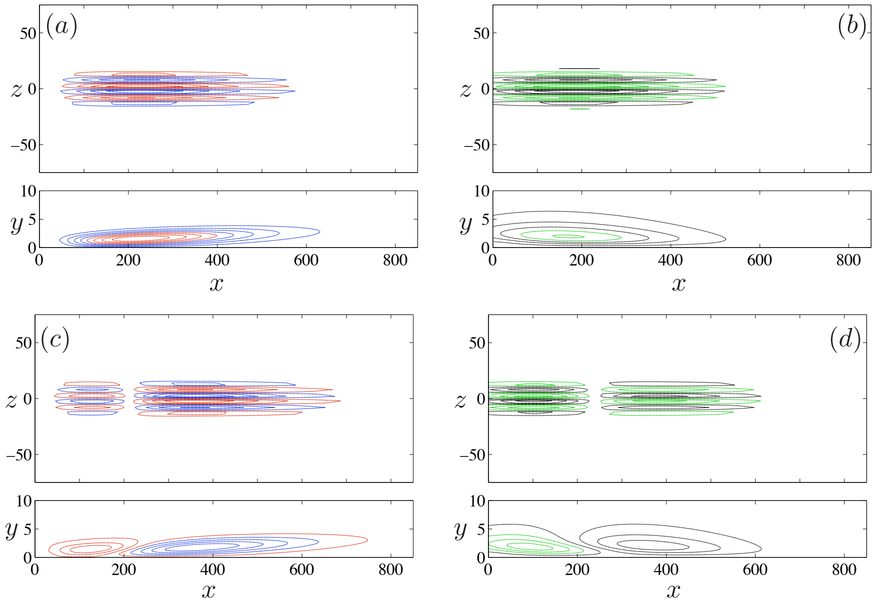

FIGURE 10. Leading balanced modes and related adjoint modes for the streaks. Left column: streamwise component of the leading balanced mode $\boldsymbol{\phi}_1$ (a) and the second balanced order mode $\boldsymbol{\phi}_2$ (c). Positive velocity is represented in red, while negative one is in blue. Right column: wall-normal component of the corresponding adjoint modes $\boldsymbol{\psi}_1$ (b) and $\boldsymbol{\psi}_2$ (d). Positive velocity is represented in black, while negative one is in green. For all the modes depicted here, the top view is shown in the xz-plane at $y \approx 1.6$, the side view is in the section xy at $z = 2$.

second step, that the control $\phi(t)$ and the estimated reduced state $\hat{q}(t) \in \mathbb{R}^r$ satisfy a linear relation involving some yet unknown matrix $K \in \mathbb{R}^{m \times r}$, *i.e.*,

$$\phi(t) = K\hat{q}(t). \tag{13}$$

The goal of this second step is then to find such a matrix K, which is referred to as the control gain. One attractive feature of LQG design is that the two steps (estimation and full-information problem) can be performed independently of each other, (see Anderson & Moore (1990)). Moreover, if both problems are optimal and stable the resulting closed-loop system, composed of the two problems is also optimal and stable. The main disadvantage of LQG is that it does not account for uncertainties of the underlying system $(\mathbf{A}, \mathbf{B}, \mathbf{C})$ (see Doyle

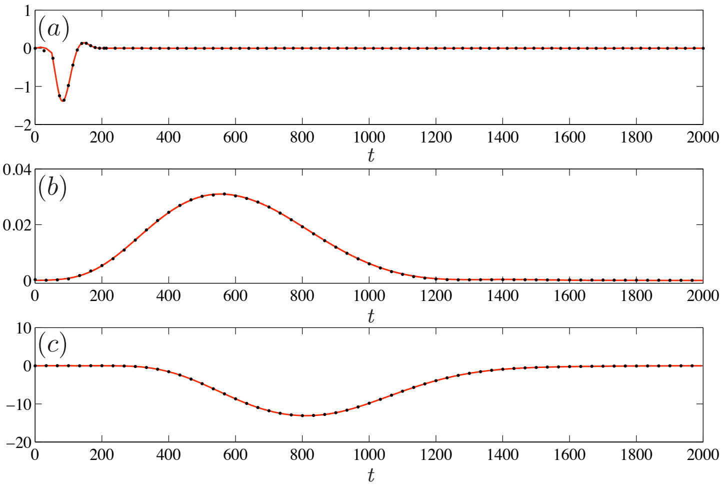

FIGURE 11. Impulse response of the system from the input $\mathbf{B}_1$ to the output $\mathbf{C}_{2,-1}$, (*b*), from $\mathbf{B}_{2,-1}$ to $\mathbf{C}_{1,1}$, (*c*) and from $\mathbf{B}_1$ to $\mathbf{C}_{1,1}$, (*d*) for the streak model. The red line shows the DNS results, while the dotted, the gray dots indicate to the impulse response of a reduced model of order 60.

1978). One can only check the robustness by *ad-hoc* testing the controller for various parameters.

For a derivation of the LQG solution, please refer to e.g. Lewis & Syrmos (1995) and Bagheri *et al.* (2009) for a "classical" optimal control framework or Doyle *et al.* (1989) and Dullerud & Paganini (1999) for a more "modern" robust control framework. Here, we just state the solution of the two separate problems.

To estimate the full state $\mathbf{u}(t)$ given only the noisy measurements $\mathsf{v}(t)$, an estimator that governs the dynamics of an estimated state $\hat{q}$ can be introduced

$$\dot{\hat{q}}(t) = A\hat{q}(t) + B_2\phi(t) + L(\mathsf{v}(t) - \hat{\mathsf{v}}(t)). \tag{14}$$

In the above expression, we compare the measurement from the velocity field $\mathsf{v} = \mathbf{C}_2\mathbf{u}$ and the measurement from the estimated state $\hat{\mathsf{v}} = C_2\hat{q}$ and feed back the mismatch in these two quantities using the estimator gain $L \in \mathbb{R}^{r\times p}$. It can be shown (Kalman 1960) that the estimation gain that minimizes the estimation error $\|q - \hat{q}\|$, and results in a stable system is given by

$$L = -\frac{1}{\alpha^2}YC_2^T, \tag{15}$$

where $Y \in \mathbb{R}^{r\times r}$ is a solution to an algebraic Riccati equation (see e.g. Laub 1991).

In the second step, assume that the full state is given by q at all times and that $\phi(t) = Kq(t)$ (instead of 13). Inserting the feedback relation into 5 and neglecting the output v, we get

$$\begin{aligned} \dot{q}(t) &= (A + B_2 K)q(t) + B_1 \mathsf{w}(t) && (16a)\\ \mathsf{z}(t) &= C_1 q(t) + I_l \phi(t). && (16b) \end{aligned}$$

It remains to choose $K \in \mathbb{R}^{m\times r}$ such that the system is stable and the control signal $\phi(t)$ minimizes output energy, $\|\mathsf{z}\|^2$. The solution is provided by a optimal control state-feedback problem, (see e.g. Anderson & Moore 1990), where the optimal control signal is given by

$$K = -\frac{1}{2}\left(I_l^T I_l\right)^{-1} B_2^T X, \tag{17}$$

and $X \in \mathbb{R}^{r\times r}$ is a solution of a Riccati equation.

Finally, combining the estimator 14 and the full-information controller 16, we obtain the reduced-order controller (also called compensator or observer) of size r,

$$\begin{aligned} \dot{\hat{q}}(t) &= (A + B_2 K + LC_2)\hat{q}(t) - L\mathsf{v}(t) && (18a)\\ \phi(t) &= K\hat{q}(t) && (18b) \end{aligned}$$

At each instant in time, given only the measurements $\mathsf{v}(t)$, the compensator provides the control signal $\phi(t)$. The controller thus connects measurements from sensors to the actuator, that in combination with the Navier–Stokes system 5, results in a feedback closed-loop system, denoted by $\mathbf{G}_c$ hereafter.

When the external disturbances are white noise processes, the 2-norm of the closed-loop system is a convenient measure of the input-output behavior. The 2-norm of the closed-loop system $\mathbf{G}_c$ can be defined (Green & Limebeer 1995) as

$$\|\mathbf{G}_c\|_2^2 = \int_0^\infty |\mathsf{z}|^2 \mathrm{d}t = \|\mathsf{z}\|^2_{L^2(0,\infty)} \tag{19}$$

So, the 2-norm of $\mathbf{G}_c$ equals the control objective 7 defined earlier (for the infinite time horizon) and can be calculated from the signals extracted by the output $\mathbf{C}_1$.

5.2. *Centralized vs. decentralized approach*

The spatial localization of the actuators and the sensors requires a proper multivariable approach for the controller design. A simple approach is a *decentralized control*, where each actuator is connected only with one sensor (in our case, the corresponding upstream sensor); in such a controller, each loop can be regarded as a single-input-single-output (SISO) system and an equal number of actuators and sensors is required. If the decentralized controller is stable in each SISO loop and the inputs and the outputs are decoupled or only weakly coupled, then the closed loop is also stable.

For the TS wavepacket case, the decentralized approach yielded an unstable closed-loop system in numerical tests. A physical explanation is that the

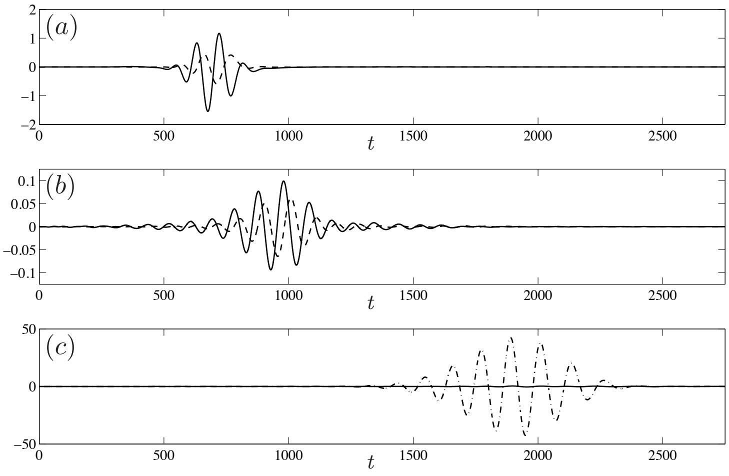

FIGURE 12. Input and output signals of the closed-loop system excited by an impulsive forcing. (*a*) Output signals extracted from $\mathbf{C}_{2,0}$, located in $(x, z) = (300, 0)$ (solid line), and $\mathbf{C}_{2,2}$, placed in $(x, z) = (300, +40)$ (dashed line). (*b*) The controller signals fed in $\mathbf{B}_{2,0}$ and $\mathbf{B}_{2,2}$ are indicated with a solid line and a dashed line, respectively. (*c*) Measurements extracted by the first sensor $\mathbf{C}_{1,1}$ for case A (solid) and the uncontrolled case (dashed-dotted line).

perturbation triggered in the boundary layer by the localized initial condition shown in figure 2 gradually spreads in the spanwise direction while propagating. This results in a dynamic coupling in the spanwise direction; thus, in this particular configuration the decentralized approach is unfeasible since the spanwise coupling is disregarded. A second analysis is given by the *relative gain array* (RGA) matrix (Skogestad & Postlethwaite 2005, pp. 510-514), that provides a measurement of the degree of coupling among the inputs and the outputs of the system. Applying it on the reduced-order model, a strong coupling was found, confirming the presumption carried from the numerical tests.

Conversely, for the streaks case, the numerical tests resulted in a stable closed-loop system with both the approaches, although the closed-loop system built using the centralized design showed best performance. Moreover, the RGA matrix analysis suggested a weak degree of cross-coupling of the I/O system. From a physical point of view, this behaviour can be explained considering the strong elongation in the streamwise direction and the slow spanwise spreading of the streaks; these features result in a weak dynamical coupling in the spanwise direction. Nonetheless, a centralized approach accounts for the spanwise cross-coupling without disregarding it, resulting in more efficient disturbance mitigation.

In this work, we design a *centralized controller* for all cases (A-M, N-Q), *i.e.* all the actuators are connected with all the sensors used for estimation. Using the LQG approach, a centralized controller is guaranteed to result in a stable closed-loop system.

6. Control of TS wavepackets

In this section, the performance of the closed-loop system for the different sensor-actuator configurations listed in table 1 is investigated. In the reference case A, a *full* set-up is considered, where the row of actuators and the row of estimators consist of 9 localized Gaussian elements equally spaced in the spanwise direction. Using this setup, three cases are studied with different control penalty l (cases A-C) and four cases are analysed with different degree of noise contamination α (cases D-G); with $\alpha = 0.01$, case A can be considered to be an inexpensive controller when $l = 100$ (the controller effort is relatively cheap); case B is an intermediate case, with $l = 250$, whereas case C is an expensive case, with $l = 500$. In configurations D-G, the control penalty l is fixed, while the noise contamination parameter α is changed. Finally, for the cases H-M, a reduced number of actuators and/or sensors is used, in order to investigate the dependence of the closed-loop performance on m and p.

We investigate the performance of the controlled closed-loop system and the uncontrolled Navier–Stokes system, when an impulsive forcing $w(t) = \delta(0)$ or a stochastic white-noise forcing is applied. We consider: (i) the impulse response (time signals), which provides a physical and direct measure of the control performance; (ii) the system 2-norm, which represents a total measure of the input-output behavior and (iii) perturbation energy in the full spatial domain Ω.

In table 1, the 2-norm and the ratio between the peak energy and the initial disturbance energy is tabulated for each case. We observe a significant reduction of both measures. In the following section these results are investigated further.

6.1. *Input-output analysis of the closed-loop system*

In figure 12, a few sensor measurements and actuator signals $\phi(t)$ for an impulse in $\mathsf{w}(t)$ pertaining to case A are shown. The location of actuators and sensors are shown schematically in figure 1. Figure 12(a) shows measurement signals used for estimation of the disturbance associated with the sensors $\mathbf{C}_{2,0}$ and $\mathbf{C}_{2,2}$ for an impulse in $\mathbf{B}_1$. The measurement detected by $\mathbf{C}_{2,0}$ (solid line) reveals a wavepacket structure of the evolving disturbance. The travelling disturbance reaches the sensor location at $t \approx 500$, in agreement with the estimated velocity of the wavepacket in a boundary layer ($\approx 0.47U_\infty$). The element $\mathbf{C}_{2,2}$ (dashed line) shows an analogous behaviour, although a delay due to the spanwise

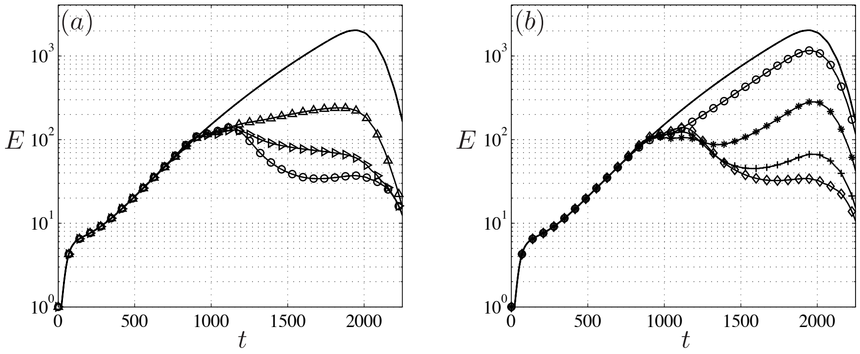

FIGURE 13. Kinetic energy as function of time. In (a) and (b), the solid line shows the energy of $\mathbf{B}_1$. In (a), three closed-loop configurations for three different control penalties l are compared: a cheap case ($-\circ-$), an intermediate case ($-\triangleright-$) and an expensive case ($-\triangle-$). In (b) the influence of noise corruption α on the performance is considered; the curves correspond to case D ($-\diamond-$), E ($-+-$), F ($-\star-$) and G ($-\circ-$).

spreading of the wavepacket is observed; moreover the signal is characterized by a smaller amplitude.

Figure 12(b) shows the control signals feeding the actuators $\mathbf{B}_{2,0}$ and $\mathbf{B}_{2,2}$; they are depicted with a solid line and a dashed line, respectively. In both cases a time lag of 200 time units from the estimation signals is observed, to account for the advection of the waves from the location of the sensors to the location of the actuators array. The shift observed between the two signals is related to the three-dimensional structure of the incoming perturbation. As mentioned previously, the actuator signals are computed using all the measurements extracted from $\mathbf{C}_2$. The control signal corresponds in fact to a cancellation-signal; if the sensors were located at the same location as the actuators, a signal 180 degrees out of phase with the control signal would be measured. Cancellation techniques where a second wave of appropriate amplitude and phase cancel the traveling wave by interference has been investigated for a long time (see e.g. Milling 1981). However, the main feature of the feedback approach adopted here is that no *a priori* knowledge of the functional behavior of the controller is required and the controller is able to react to unexpected systems uncertainties.

In figure 12(c), the output signal extracted from $\mathbf{C}_{1,1}$ (first POD mode) is compared between the controlled case (solid line) and the uncontrolled case (dashed-dotted line). It is clear that the amplitude of the closed-loop output signal is significantly reduced. Computing the system 2-norm, the performance can be evaluated by taking into account all the $k = 10$ signals extracted by $\mathbf{C}_1$. As shown in table 1, for case A $\|\mathbf{G}_c\|_2^2 = 1.42$; this is a reduction of about 99% of the 2-norm of uncontrolled case ($\|\mathbf{G}\|_2^2 = 324.25$). As the controller effort is

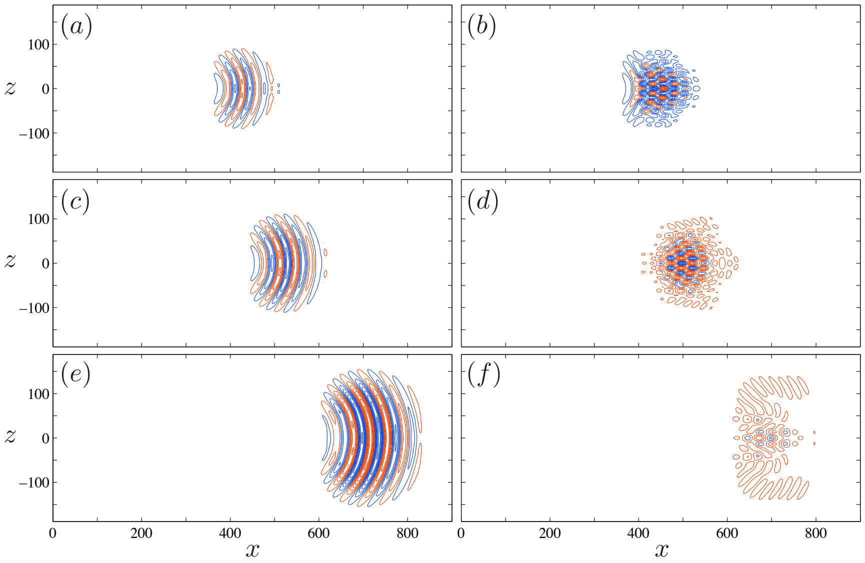

FIGURE 14. Evolution of a TS wavepacket at $t = 1000, 1250, 1750$, without control (left column) and with control (right column). The iso-contours of the streamwise component are shown in the xz-plane at $y \approx 1.9$; red isolines indicate positive velocity, while the negative one is indicated with blue. All the plots are characterized by the same isocontour range $[-1.03, 1.03]$.

reduced, we observe higher values of $\|\mathbf{G}_c\|_2^2$ (case B, $\|\mathbf{G}_c\|_2^2 = 12.23$ and case C, $\|\mathbf{G}_c\|_2^2 = 55.27$). Increasing the degree of noise corruption of the signal leads to a worsening of the performance; in particular, this is evident when rather high values of α are considered; for instance, in case D, a reduction of about 99% is observed ($\|\mathbf{G}\|_2^2 = 1.48$), whereas for cases F and G, $\|\mathbf{G}_c\|_2^2 = 209.03$ and $\|\mathbf{G}_c\|_2^2 = 318.74$, respectively.

6.2. *Perturbation energy and disturbance evolution*

Figure 13(a) shows the kinetic energy (in the full domain Ω) as a function of time for the uncontrolled case (solid line) and the controlled case A ($- \circ -$). The energy peak for the uncontrolled case is reached at $t \approx 1820$, with an energy amplification $E(t_{max})/E(0) = 2 \times 10^3$, whereas the controlled case shows one order of magnitude smaller peak value at $t \approx 1100$. Note that the controller is designed to reduce the norm of $\mathbf{C}_1$ and not the total kinetic energy of the flow. Nonetheless, by demanding the disturbance energy to be small at $\mathbf{C}_1$, the disturbance amplitude has to decrease significantly before it reaches the objective function. Therefore, minimization of disturbance energy in the region defined by $\mathbf{C}_1$ results in an actual reduction of the energy in the entire domain. The streamwise velocity component of the disturbance field at $t = 1000$, 1200, 1750 for case A (left column) and the uncontrolled case (right column) are shown in figure 14. The iso-contours display the flow field in the xz-plane at $y = 2$. At $t = 1000$, the perturbation is convected past the location $x = 400$, where the array of actuators is placed; the original structure is distorted into a more complicated three-dimensional pattern, where traces of localized actuators are recognizable. At $t = 1250$, the perturbation appears to be mostly concentrated in the center ($z \approx [-50, 50]$) of the domain, whereas the spanwise extension of the structures is significantly reduced. The original nearly two-dimensional structure breaks down into a fully three-dimensional structure. Finally, at $t = 1750$, a significant damping of the amplitude results in contour levels that are barely visible for case A, while the perturbation for the uncontrolled case attains its maximum energy. It is interesting to note that similar results were obtained by Sturzebecher & Nitsche (2003). These authors performed an experiment based on an adaptative controller designed to attenuate the TS instabilities; also in this case, the disruption of the original two-dimensional structure resulted in a reduction of the disturbance level.

Figure 13 also shows the performance of the *full* set-up controller for different choices of the penalty l (cases A, B and C). It is interesting to point out that for an intermediate value ($l = 250$, case B) the perturbation is characterized by a peak energy value close to the corresponding configuration with a cheap controller effort, although the norm $\|\mathbf{G}_c\|_2^2$ is higher. Case C (expensive controller) is the only configuration where the perturbation energy does not decay monotonically downstream of the actuators. When the noise corruption degree is considered as a parameter (cases D-G), an improvement is noticed - as expected - when smaller values of α are considered.

Figure 15(a) shows the behaviour of the controlled case A (red line) compared to the reference case, when the perturbation is excited with a stochastic white-noise forcing; the location of the actuators is indicated by a blue region, whereas the gray region indicates the location of the sensors. In the streamwise interval $[390, 460]$, in the vicinity of the actuators, the r.m.s. value of the streamwise velocity component, after a small overshoot, begins to decay and at the end of the domain, it is nearly one order of magnitude smaller than the uncontrolled flow. The behaviour of the disturbance energy in time is shown in figure 15(b); the mean values indicate a reduction of one order of magnitude of the energy amplitude and a significant reduction of the fluctuation (*i.e.* variance) is observed for the controlled case.

6.3. *Influence of the number of sensors and actuators*

The norm $\|\mathbf{G}_c\|_2^2$ and the energy amplification for cases D-F are reported in table 1. It can be concluded that controllers with a lower number of actuators than case A ($m = 9$) are still able to reduce the norm $\|\mathbf{G}_c\|_2^2$ significantly,

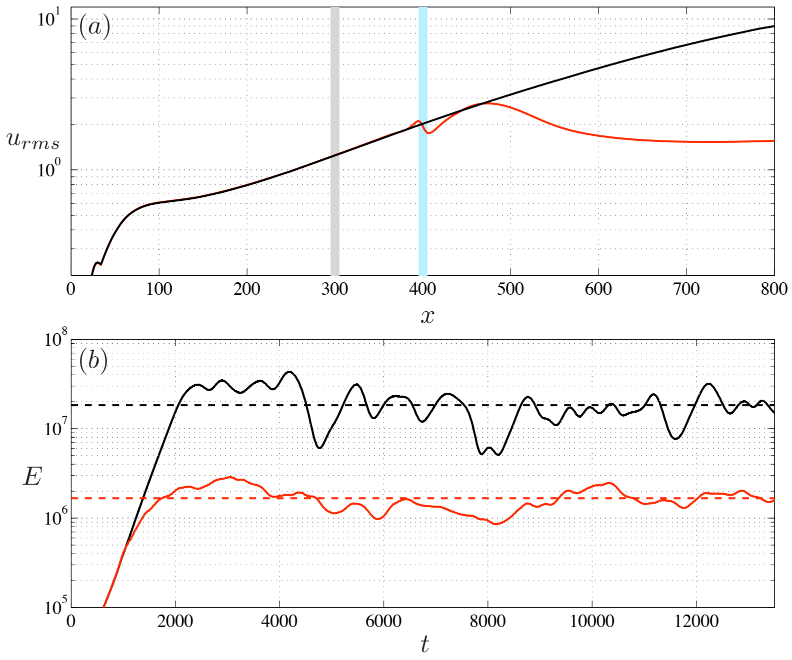

FIGURE 15. (a), The r.m.s. values of the uncontrolled system (black line) and the controlled system A (red line). The location of the actuators and sensors is indicated by a blue region and a gray region, respectively. (b), Perturbation energy vs time for a case forced by stochastic white-noise signal $w(t)$ for an uncontrolled case (black lines) and a controlled case (red lines); the dotted lines represent the mean of the energy in the interval $t \in [2500, 12500]$.

whereas there is a somewhat less efficient reduction in the perturbation energy amplification.

Figure 16(a) shows the energy behaviour for cases H-L in addition to the reference case A and the uncontrolled case. A gradual improvement of the performance is observed when the number of actuators is increased. Indeed, by increasing the number of the equidistant actuators, it is possible to cover a wider region in the spanwise direction. As a consequence, a considerable reduction of the energy growth is observed only when a sufficiently wide region in the spanwise direction is spanned by the actuator array. In particular, case H $(m = 3, p = 3)$ can be considered an example of insufficient actuation; in figure 16(a), we notice an initial overshoot of the energy in the interval $t \in [1000, 1200]$, when the controller begins to act, and a weak energy reduction. Moreover, the spatial evolution of the perturbation - not shown here - is similar

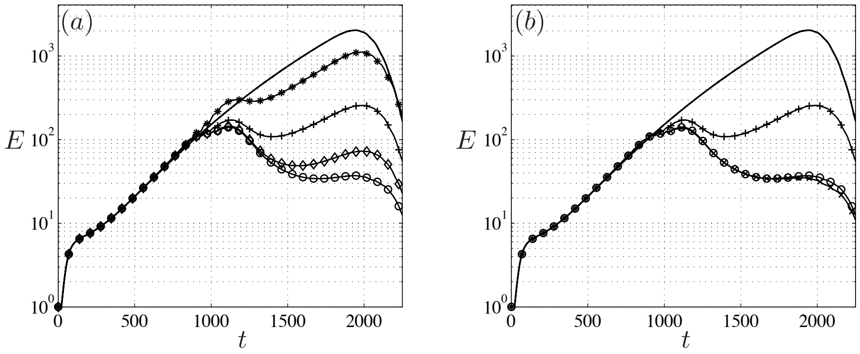

FIGURE 16. Kinetic energy as function of time. In (a) and (b), the solid line shows the energy of $\mathbf{B}_1$. In (a), case H ($-\star-$), I ($-+-$), L ($-\diamond-$) and A ($-\circ-$) are characterized by 3, 5, 7 and 9 actuators, respectively. In (b), the curves correspond to case I ($-+-$), M ($-\times-$) and A ($-\circ-$) with 5, 5 and 9 sensors, respectively.

to the uncontrolled case, indicating a weak influence of the actuator on the perturbation structure.

Figure 16(b) shows the influence of the number of sensors (case I and M). The energy curve for case A ($m = 9$), obtained with nine estimators, is hardly distinguishable from the curve obtained with the controller designed for case M, based only on five estimators. The array of sensors is located further upstream than the array of actuators, where the spanwise extension of the TS wavepacket is smaller. Therefore, the sensors located on the flanks have a nearly insignificant contribution to the estimation of the disturbance.

7. Control of streaks

The performance of the closed-loop system in the case of streaks is investigated considering three different configurations, see table 2. In all cases the rows of actuators and sensors consist of 8 localized Gaussian elements, equally spaced in the spanwise direction ($\Delta_z = 4$). More details are sketched in figure 1, where the location of the elements is depicted. The parametric investigation is carried out considering three different control penalties l: the reference case N is a cheap controller with $l = 50$; case O is an intermediate case with $l = 100$, whereas case P is the expensive case, with $l = 150$. The description of the results closely follows the steps considered previously for the TS control, using: (i) the impulse response (time signals), (ii) the 2-norm of the system and (iii) the perturbation energy in the full domain.

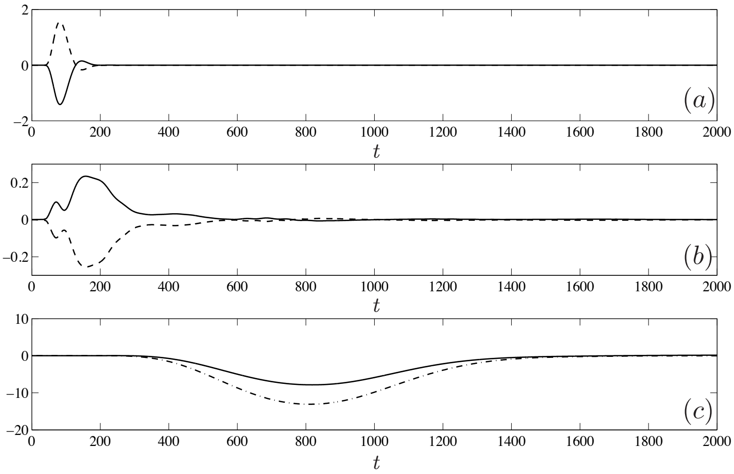

FIGURE 17. Input and output signals of the closed-loop system N excited by an impulsive forcing. (*a*) Output signals extracted from $\mathbf{C}_{2,1}$, located in $(x, z) = (100, 4)$ (dashed line), and $\mathbf{C}_{2,-1}$, placed in $(x, z) = (100, -4)$ (solid line). (*b*) The controller signals fed in $\mathbf{B}_{2,1}$ and $\mathbf{B}_{2,-1}$ are, respectively indicated with a solid line and a dashed line. (*c*) Measurements extracted by the first sensor $\mathbf{C}_{1,1}$ for case N (solid) and uncontrolled (dashed-dotted line).

7.1. *Input-output analysis and disturbance evolution*

Figure 17($a - c$) shows measurements extracted from the system and actuator signals $\phi(t)$ for the reference case N. In particular, figure 17(a) reports the signals extracted for the estimation from the sensors $\mathbf{C}_{2,+1}$ and $\mathbf{C}_{2,-1}$, depicted with a dashed line and a solid line, respectively. The signals are opposite in phase, since the perturbation is anti-symmetric with respect of the xy-plane ($z = 0$). The sensors register the disturbance at $t \approx 100$, in accordance with the estimated velocity of propagation of a streak in a boundary layer ($\approx 0.80 - 0.85 U_\infty$). The signal amplitude reaches its maximum at $t \approx 150$, after which it decays. The actuators $\mathbf{B}_{2,+1}$ and $\mathbf{B}_{2,-1}$ are fed with the signals shown in figure 17(b) with a solid and dashed line, respectively. The actuation is activated as soon as the sensors detect the incoming perturbation. It is interesting to note that the actuator signal has a sign opposite to the corresponding sensor measurement: a positive measurement extracted by the sensor coincides with a negative actuation signal further downstream and vice versa, similar to the so-called opposition control (Hammond *et al.* 1998).

Finally, figure 17(c) shows the measurements extracted from the sensor $\mathbf{C}_{1,+1}$ for both the controlled case (solid line) and the reference uncontrolled

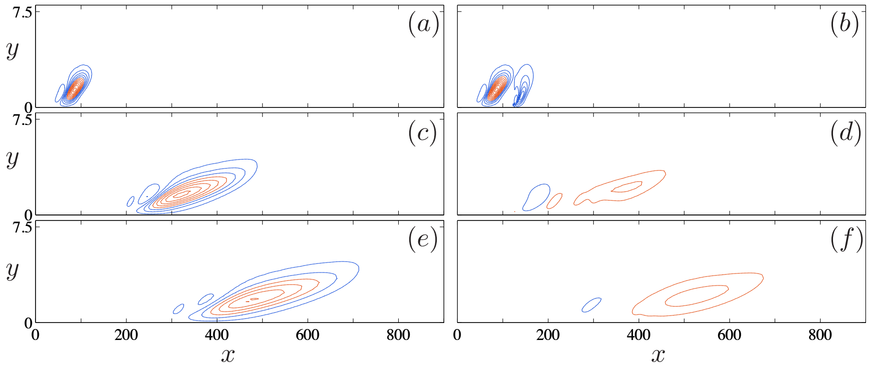

FIGURE 18. Impulse response to a localized initial condition triggering the lift-up effect at $t = 100, 500, 750$. The iso-contours of the streamwise component are shown in the xy-plane at $z = 4$ without control (left column) and with control (right column). Positive velocity is indicated with red contours, while blue contours indicate negative velocity; all the plots have the same isocontour range $[-0.65, 0.65]$.

case (dashed-dotted line). A reduction of the signal amplitude is observed, although the overall performance is worse than for the TS case. Figure 18 shows the streamwise velocity component for the uncontrolled case (left column) and the controlled case H (right column); the iso-contours display the flow field in the xy-plane at $z = 1.5$ for three instants of time, $t = 100, 500, 750$. The same isocontour levels are considered for each instant of time. As previously noticed, the controller action starts as soon as the perturbation reaches the estimation sensors location at $x = 75$; indeed, it is possible to notice at $t = 100$ the action of the controller in $x = 125$. At $t = 500$, the perturbation has travelled further downstream, while being reduced by the controller. The structure of the perturbation, show in figure 18*d*, is similar to the uncontrolled case in figure 18*c*, although of lower amplitude. Final decay due to the viscous effects is observed at $t = 750$ in both the cases. The streak is disrupted by the actuation at the wall. The effect of the control on the evolving perturbation is similar to the reactive controller implemented by Lundell (2007) and the modulated blowing/suction used by the same author in a previous work, (Lundell 2003).

In table 2, the performance of the controllers with various control penalties is quantified by the 2-norm of the transfer function $\mathbf{G}_c$. A reduction of about 66%, 30% and 16% of the 2-norm of the transfer function $\mathbf{G}_c$ is reported for the cheap (case N), intermediate (case O), and the expensive controller (case P), respectively.

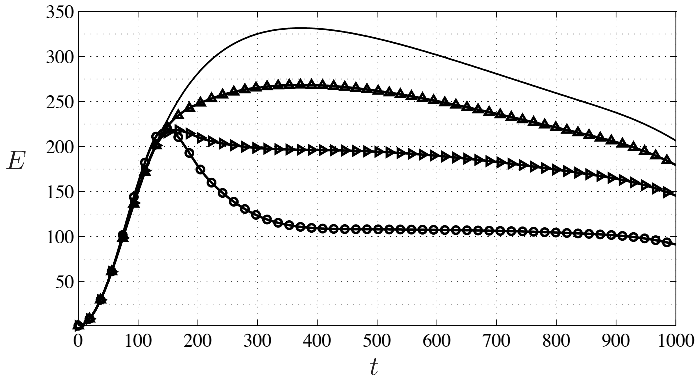

FIGURE 19. Disturbance energy as function of time for the streaks. The uncontrolled reference case $St0$ is represented by a solid line. The closed-loop configurations listed in table 2 are shown: the cheap case N, $(-\circ-)$, the intermediate case O, $(-\triangleright-)$, and the expensive case P $(-\triangle-)$.

7.2. *Perturbation energy*

Figure 19 shows the kinetic energy of the streak disturbance in the full domain Ω as a function of time. The uncontrolled case is indicated with a solid line and it is characterized by an energy amplification $E(t_{max})/E(0) = 3 \times 10^2$, occurring at $t \approx 350$. The cheap controller ($l = 50$) and the intermediate controller ($l = 100$) give an initial peak at $t \approx 180$, followed by the decay of the perturbation amplitude; in both cases, a reduction of about 33% of the energy peak is observed. Although the energy peaks are almost comparable for the controller N and O, the first one is more aggressive and shows a stronger damping of the energy amplitude for $t \approx 200$.

Figure 20 shows the behaviour of the controlled cases N and Q compared with the reference case, when the perturbation is excited with a stochastic force (white noise); the r.m.s of the streamwise velocity is considered along the streamwise direction. The aim of this analysis is twofold: understanding how the controller behaves along the x-coordinate, and providing some insights about the influence of a different location of the arrays. In all the cases a quick drop of the r.m.s. values is observed at the location of the actuators, where the controller starts to act on the perturbation. Actuators located upstream, as in case N, allow a larger reduction of the maximum u_{rms}. However, simulations performed with actuators further upstream show a worsening of the performance due to an increase of energy at the actuators locations. Downstream of the actuation, at $x \geq 150$, the r.m.s values slowly decay.

The control performance subject to stochastic excitations indicates that the controller is able to continuously react to different temporal scales, which is encountered for example in the presence of free-stream turbulence (FST).

8. Discussion and remarks

In this section we discuss the results presented above in the context of practical implementation and future development of our investigation. The fully three-dimensional set-up makes the present controller close to possible experimental implementation, where localized actuators and sensors are used. It is possible to use numerical studies to gain valuable information about the experimental set-up beforehand and to compute the control gains that will be implemented. The sensors and the actuators ($\mathbf{C}_2$ and $\mathbf{B}_2$, respectively) can be modeled as localized volume forcing. The objective function $\mathbf{C}_1$ can be defined either numerically or using an array of sensors. In particular, the first choice relies on the possibility of reproducing a POD approach as the one we followed in the control design once the upstream disturbance $\mathbf{B}_1$ is modelled. Here, optimal initial conditions were used to show the feasibility of the control, but - in general - the choice of the upstream disturbance $\mathbf{B}_1$ is closely related to the enviroment that one desires to reproduce. For instance, the perturbation arising from free stream turbulence (FST) can be modeled using a projection over a finite number of optimal modes (Tempelmann *et al.* 2010). Conversely, in a low-noise environment, where TS waves dominate, localized initial conditions distributed in the spanwise direction can spontaneously generate packets of TS waves. Once the inputs and outputs are modeled, the LQG compensator can be easily designed following the explained procedure; moreover, numerical tests can help determining the most efficient form of actuation, provided these are correctly modeled in the simulations. The location and number of sensors and actuators is also easier to test in a simulation than in a laboratory. Useful information can be obtained in this case by examining the spatial structure of the direct and adjoint balanced modes. In this respect, our results suggest that, for an effective implementation of feedback control of a three-dimensional wavepacket in a boundary layer, actuation may be more crucial than sensing and estimation of incoming disturbances. This is in agreement with the recent empirical observations in Monokrousos *et al.* (2010*b*).

A further strategy directly applicable in experiments relies on a system identification algorithm, known as the Eigensystem Realization Algorithm (ERA). This represents an approach formally equivalent to the model reduction procedure discussed here; for more details, we refer to Ma *et al.* (2009). This technique allows the identification of a model for the system from the input/output analysis and is thus particularly well-suited to experimental setup. Once the model is identified from the experimental data, it is possible to design an appropriate LQG controller for the experiment. However, information about balanced modes, sensitivity and spatial structures of the most amplified perturbations are not accessible in this way.

The choice of actuators/sensors and their placement was decided mainly by following physical arguments based on the knowledge of the instabilities. To control TS wavepackets, the array of actuators was placed in the center of the

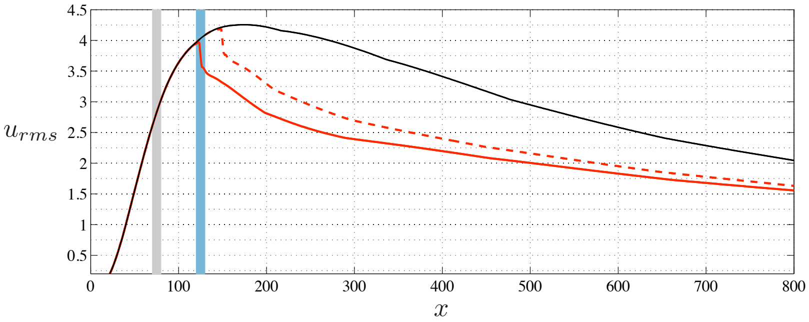

FIGURE 20. The r.m.s. values of the uncontrolled system (black line), the controlled system N (red line) and the controller system Q (dashed red line). For case N, the location of the actuators and sensors is indicated with a blue and grey region, respectively.

box. Indeed, after the actuation, the perturbation recovers the spanwise coherence and experiences new energy growth, similar to the one achieved during the first stage (see figure 14f). However, this behaviour clearly suggests the need of introducing a repeated streamwise actuation, as shown in Sturzebecher & Nitsche (2003). The introduction of multi-stage actuation can improve the overall performance of the device, moving the transition location further downstream. Moreover, using successive arrays it is possible to target instabilities of different frequency growing at different Reynolds numbers (different streamwise regions), or perturbations that arise in the presence of adverse pressure gradients.

To control streaks, two different setups located in different streamwise positions were tested; an improvement of the overall performance (around $\approx 15\%$) was observed when the sensors and actuators were further upstream. Note that in the case streaks are induced by FST, there is a longer upstream region of streak growth; moreover, the streaks we introduced are optimal and characterized by a fast energy growth. Therefore, in presence of external FST, the estimation/control can be more effective. As shown before, and in agreement with the experimental results by Lundell (2007), streaks are damped at the location of actuators. However, streaks can be regenerated early with the presence of FST, see Monokrousos *et al.* (2008). Thus repeated control can be also exploited here by introducing a number of arrays acting at different position in the streamwise direction.

The possibility of placing more than one actuation array and their interaction was also investigated. We performed numerical tests - not reported here - where the TS-controller and the streak controller were simultaneously active, in presence of a TS-wave, streaks or a linear combination of the two optimal initial conditions. We observed that the streaks controller damped only the

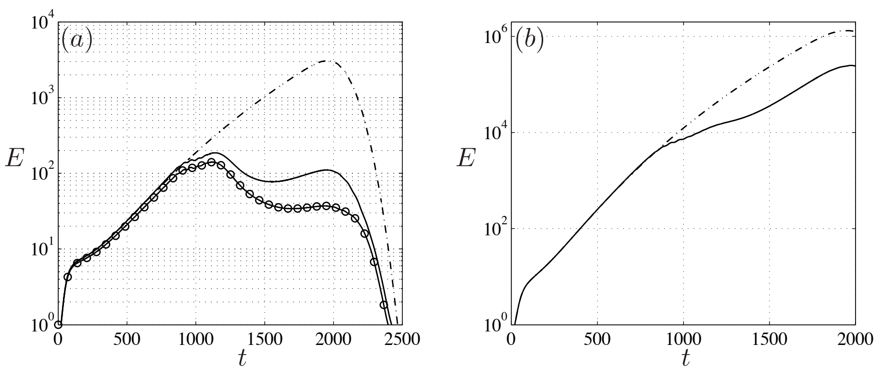

FIGURE 21. Perturbation energy as function of time for TS wavepackets at two off-design conditions. The controlled cases are obtained using the controller A. Left panel: kinetic energy vs time for the TS-wave propagating at $Re = 1050$ is represented by a dashed-dotted line. A black line indicates the behaviour of the controller in off-design condition, whereas the dotted-line is related to the same controller acting at design conditions. Right panel: perturbation energy evolution for a wavepacket evolving in presence of an adverse gradient pressure (m=-0.025). The black line is the controlled case.

streaky structures, while the setup further downstream quenched only the TS-waves. The behaviour can be interpreted considering the POD-based objective function, which is completely different in the two cases, so that one type of disturbance is transparent to the controller designed for the other type. In other words, the TS controller did not react in the presence of streaks, whereas it was effective when TS-packets were introduced, and, vice versa, the streak controller did not react in presence of TS. Note that this framework allows building of a reduced-order model able to act on disturbances that have different time- and length-scales.

Finally, for a practical implementation, we have to account for unavoidable modeling errors; in the present paper, we assumed a perfect knowledge of the flow parameters, but, in general, a practical implementation of the control needs to guarantee robust performance when uncertainties are present as well. The optimal control framework used here does not account explicitly for uncertainties; however, it is important to note that the behaviour of the controller can nonetheless be robust enough to small deviation of the flow parameters. Using numerical simulations, it is possible to verify the robustness of the controller. In figure 21, two examples are shown: deviation from the design-Reynolds number (*a*), and behaviour in presence of adverse pressure gradient (*b*). In the first case, for a deviation of ±5% of the nominal Reynolds number, it is still possible to achieve good performance. Further investigation at higher Reynolds number revealed a progressive worsening of the performance, analogous to what we observed with fewer actuators. The presence of an adverse pressure gradient introduces a strong change in the propagation of the wavepackets, both in terms of amplification and propagation speed; a Falkner-Skan-Cooke (FSC) boundary layer is considered, with $m = -0.025$, see Schlichting & Gersten (2000). As expected from linear stability theory, the disturbance energy shows a larger amplification, $E_{max}/E_0 \approx 1.3 \times 10^6$, figure 20*b*. In this case the controller used for case A is still able to reduce the magnitude of the energy peak by almost one order of magnitude, but the result is overall less satisfactory than for the nominal pressure gradient. The difference in the performance is mainly attributed to the different speed of the traveling unstable waves, which makes the actuation slightly out of phase. In addition, since the estimator is expecting lower amplifications, the control signal is weaker than necessary. To conclude, it is worthwhile to point out that a more robust controller can be included in this framework. An example is given by the $\mathcal{H}_\infty$ approach (Dullerud & Paganini 1999).

9. Conclusion

Using systematic methods from control theory in combination with localized sensing/actuation, it is possible to reduce the growth of small-amplitude three-dimensional disturbances in the boundary layer. To this end, we have built low-dimensional models ($r = 60$) that capture the input-output behavior of the flat-plate boundary layer, and used these models for the optimal feedback control design. The initial conditions considered provide the maximum energy growth for a given final time; in particular, we demonstrated that the energy of three dimensional Tollmien-Schlichting wavepacket, obtained for long-time optimization, is damped by two orders of magnitude using 9 sensors for estimation and 9 actuators. The control performance was also investigated with a reduced number of sensors and actuators in the configuration; it was found that a smaller number of actuators decreases significantly the effectiveness of the controller, whereas a reduced number of sensors has a smaller impact on the performance. When a short time of optimization is considered, an initial condition triggering a streaky wavepacket is obtained; in this case, the perturbation energy can be damped using 8 sensors for the estimation and 8 sensor for the actuation.

Although the significant reduction of perturbation energy for transition control remains to be tested, such a drastic energy reduction is likely to result in a delay of the initial stages of the transition process. If the actuators and sensors represent realistic models of physically feasible devices, it is possible to use the low-dimensional controller designed numerically in laboratory experiments. The fact that we have modeled the inputs and outputs as volume forcing does not mean that they cannot be implemented experimentally. It is the effect of an actuator that is important to model, and not the actuator itself. Another issue that needs to be taken into account for a real application is control robustness. If the numerically designed controller is used in laboratory experiments, it is unavoidable that some parameters, such as Reynolds number and pressure gradients, will vary. We showed that the controllers are robust to a strong deviation of the Reynolds number, whereas the performance was less satisfactory at an off-design pressure gradient. Fortunately, modern developments in robust control theory may be used to rigorously incorporate uncertainties that may be present in the design process. The method for optimal control presented in this paper, can be incorporated into such a robust control framework.

The authors would like to thank Antonios Monokrousos, for providing the optimal initial conditions and for fruitful discussions, and Miloš Ilak, for the detailed comments on the manuscript. Computer time provided by SNIC (Swedish National Infrastructure for Computing) is gratefully acknowledged. This work was partially sponsored by the Air Force Office of Scientific Research, through the European Office EOARD, under grant/contract number FA8655-10-M-4006. The authors also aknowledge financial support from the Swedish Research Council (VR).

Appendix A. Analytical expressions of actuators and sensors

Each element of the arrays $\mathbf{B}_2$ and $\mathbf{C}_2$ is a localized Gaussian function

$$\mathbf{h}\left(\mathbf{x},\mathbf{x}_0\right) = \begin{pmatrix} \sigma_x \hat{y} \\ -\sigma_y \hat{x} \\ 0 \end{pmatrix} \exp\left(-\hat{x}^2 - \hat{y}^2 - \hat{z}^2\right) \tag{20}$$

where

$$\hat{x} = \frac{x - x_0}{\sigma_x} \qquad \hat{y} = \frac{y}{\sigma_y} \qquad \hat{z} = \frac{z - z_0}{\sigma_z}.$$

The scalar quantities appearing in the denominator define the size of the Gaussian spatial distribution close to the wall and are equal for all the elements; for the TS-waves, we considered $(\sigma_x, \sigma_y, \sigma_z) = [5, 1.5, 6]$, whereas for the streaks we used $(\sigma_x, \sigma_y, \sigma_z) = [1.75, 2, 2]$. All the elements of the arrays have the same spatial shape; the position in the plane xz is given by $\mathbf{x}_0$ and is contained for all the test-cases in the tables 1 and 2. From this definition, we obtain

$$\mathbf{B}_2 = \left[\mathbf{h}\left(\mathbf{x},\mathbf{x}_{\phi,1}\right), \mathbf{h}\left(\mathbf{x},\mathbf{x}_{\phi,2}\right), \ldots, \mathbf{h}\left(\mathbf{x},\mathbf{x}_{\phi,m}\right)\right] \tag{21}$$

and

$$\mathbf{C}_2\mathbf{u} = \int_\Omega \begin{pmatrix} \mathbf{h}\left(\mathbf{x},\mathbf{x}_{\mathrm{v},1}\right)\mathbf{u} \\ \ldots \\ \mathbf{h}\left(\mathbf{x},\mathbf{x}_{\mathrm{v},p}\right)\mathbf{u} \end{pmatrix} \mathrm{d}x\mathrm{d}y\mathrm{d}z \tag{22}$$

where, m and p indicate the number of actuators and sensors, respectively. Each element of $\mathbf{B}_2$ and $\mathbf{C}_2$ is denoted with a second subscript. The actuators mimic a manipulation on the flow close to the wall; the measurements are extracted by averaging the velocity field using the Gaussian function as weights.

Denoting with $\mathbf{p}(\mathbf{x},t)=(u^*,v^*,w^*)$ the adjoint velocity field, the adjoint of the input and output operators $\mathbf{B}_2$ and $\mathbf{C}_2$, associated with the inner product $\langle\cdot,\cdot\rangle_\Omega$, are

$$\mathbf{B}_2^*\mathbf{p}=\int_\Omega\begin{pmatrix}\mathbf{h}\left(\mathbf{x},\mathbf{x}_{\phi,1}\right)\mathbf{p}\\ \dots\\ \mathbf{h}\left(\mathbf{x},\mathbf{x}_{\phi,m}\right)\mathbf{p}\end{pmatrix}\mathrm{d}x\mathrm{d}y\mathrm{d}z \tag{23}$$

and

$$\mathbf{C}_2^*=\left[\mathbf{h}\left(\mathbf{x},\mathbf{x}_{\mathsf{v},1}\right),\mathbf{h}\left(\mathbf{x},\mathbf{x}_{\mathsf{v},2}\right),\dots,\mathbf{h}\left(\mathbf{x},\mathbf{x}_{\mathsf{v},p}\right)\right]. \tag{24}$$

Hereinafter, the notation adopted in the next sections will denote the continuous operator; the discretized operators will be indicated by hat. Note that the hat is omitted in the article.

Appendix B. Adjoint Navier–Stokes equations

In this section, the adjoint Navier Stokes equations are given for the sake of completeness. A detailed derivation is provided by Bagheri *et al.* (2009*a*).

The adjoint velocity field and the adjoint pressure field are denoted by $\mathbf{p}(\mathbf{x},t)=(u^*,v^*,w^*)$ and $\sigma(\mathbf{x},t)$, respectively. Considering the boundary conditions 2 used for $\mathbf{u}$ and requiring that $\mathbf{p}=(u^*,v^*,w^*)$, p and σ satisfy

$$\mathbf{p}\left(0,y,-L_z/2\right)=\mathbf{p}\left(x,y,L_z/2\right) \tag{25a}$$
$$\mathbf{p}\left(0,y,z\right)=\mathbf{p}\left(L_x,y,z\right) \tag{25b}$$
$$\mathbf{p}\left(x,0,z\right)=\mathbf{p}\left(x,L_y,z\right)=0, \tag{25c}$$

$$p\left(0,y,-L_z/2\right)=p\left(L_x,y,L_z/2\right) \tag{26a}$$
$$\sigma\left(0,y,-L_z/2\right)=\sigma\left(L_x,y,L_z/2\right) \tag{26b}$$

the adjoint of the linearized Navier–Stokes equations 5 associated with the inner product $\langle\cdot,\cdot\rangle_\Omega$ is given by

$$-\frac{\partial\mathbf{p}}{\partial t}=\left(\mathbf{U}\cdot\nabla\right)\mathbf{p}-\left(\nabla\mathbf{U}\right)^T\mathbf{p}+\nabla\sigma+Re^{-1}\nabla^2\mathbf{p}+\lambda_f(x)\mathbf{p} \tag{27a}$$
$$0=\nabla\cdot\mathbf{p} \tag{27b}$$
$$\mathbf{p}=\mathbf{p}_T \qquad at \quad t=T. \tag{27c}$$

The code described in Chevalier *et al.* (2007), based on a Chebyshev-Fourier series approximation, is used for both the forward and adjoint simulations. Using this approximation, the discrete operators $\hat{\mathbf{A}}$, $\hat{\mathbf{B}}$ and $\hat{\mathbf{C}}$ and the respective adjoint operators can be defined. As in the case of the forward system, the adjoint equations 27 can be casted as an initial value problem

$$-\dot{\mathbf{p}}(t)=\hat{\mathbf{A}}^*\mathbf{p}(t) \qquad \mathbf{p}(T)=\mathbf{p}_T, \tag{28}$$

where the action of $\hat{\mathbf{A}}^*$ corresponds to evaluate the right hand side of the equation 27, including the boundary conditions. The evolution operator $\mathbf{T}^*$

associated to $\hat{\mathbf{A}}^*$ is defined as

$$\mathbf{p}(-t) = \mathbf{T}^*(t)\mathbf{p}(T). \tag{29}$$

Given an initial condition, the adjoint evolution operator $\mathbf{T}^*$ provides the resulting flow field at time $-t$.

Appendix C. Balanced truncation for model reduction

In this section ,the basic concepts for balanced truncation – controllability, observability and the *Hankel operator* – are briefly recapitulated in a simplified discrete form; for more details, we refer to Bagheri *et al.* (2009*a*), where the Hilbert spaces and the norms used are introduced for the definition of the continuous operators and the related adjoint operators.

The relation among the inputs and the outputs of the system can be described by considering the formal solution of the input-output system 5. Introducing the input vector $\mathsf{f}(t) = (\mathsf{w}, \mathsf{g}, \phi)^T \in \mathbb{R}^{(m+2)}$ and the output vector $\mathsf{y}(t) = (\mathsf{z}, \mathsf{v})^T \in \mathbb{R}^{(p+k)}$, we can rewrite the system 5 in the standard state-space form

$$\begin{aligned} \dot{\mathbf{u}}(t) &= \hat{\mathbf{A}}\mathbf{u}(t) + \hat{\mathbf{B}}\mathsf{f}(t) && (30a)\\ \mathsf{y}(t) &= \hat{\mathbf{C}}\mathbf{u}(t) + \hat{\mathbf{D}}\mathsf{f}(t) && (30b) \end{aligned}$$

where $\hat{\mathbf{B}} = (\hat{\mathbf{B}}_1, 0, \hat{\mathbf{B}}_2)$, $\hat{\mathbf{C}} = (\hat{\mathbf{C}}_1, \hat{\mathbf{C}}_2)^T$ and $\hat{\mathbf{D}} \in \mathbb{R}^{(p+k)\times(m+2)}$

$$\hat{\mathbf{D}} = \begin{pmatrix} 0 & 0 & I_l \\ 0 & I_\alpha & 0 \end{pmatrix}. \tag{31}$$

The solution of the system 30 is given by

$$\mathsf{y}(t) = \hat{\mathbf{G}}\mathsf{f}(t) = \hat{\mathbf{C}}\int_{-\infty}^{t} \mathbf{T}(t-s)\hat{\mathbf{B}}\mathsf{f}(s)ds, \tag{32}$$

assuming both the initial condition $\mathbf{u}_0$ and the term $\hat{\mathbf{D}}$ to be zero. The linear mapping $\hat{\mathbf{G}} : L^2(-\infty,\infty) \to L^2(-\infty,\infty)$ between the inputs $\mathsf{f}(t)$, and the outputs $\mathsf{y}(t)$ is a causal input-output operator. Both the signals and the system $\hat{\mathbf{G}}$ can be represented in the frequency domain. A Laplace transform of 32 results in a transfer function matrix

$$\mathsf{y}(s) = \tilde{\mathbf{G}}(s)\mathsf{f}(s) = (\hat{\mathbf{C}}(s\mathbf{I} - \hat{\mathbf{A}})^{-1}\hat{\mathbf{B}})\mathsf{f}(s) \tag{33}$$

with $s \in \mathbb{C}$. Henceforth the tilde on $\tilde{\mathbf{G}}$ is omitted since it is related to $\mathbf{G}$ by a linear transformation.

The mapping $\hat{\mathbf{G}}$ is not a finite rank operator: thus, a second finite-rank mapping is introduced. For the given system $\hat{\mathbf{G}}$, the *Hankel operator* $\hat{\mathbf{H}} : L^2(-\infty, 0] \to L^2[0, +\infty)$ is defined as

$$\mathsf{y}(t) = \hat{\mathbf{H}}\mathsf{f}(t) = \hat{\mathbf{C}}\int_{-\infty}^{0} \mathbf{T}(t-s)\hat{\mathbf{B}}\mathsf{f}(s)ds. \tag{34}$$

The Hankel operator is closely related to the *controllability* and *observability* operators. In particular, the controllability operator $\hat{\mathbf{L}}_c : L^2(-\infty, 0] \rightarrow \mathbb{U}$ is defined as

$$\mathbf{u}_0 = \hat{\mathbf{L}}_c \mathsf{f}(t) = \int_{-\infty}^{0} \mathbf{T}(-s)\hat{\mathbf{B}}\mathsf{f}(s)\,\mathrm{d}s, \tag{35}$$

and maps past input signals $\mathsf{f}(t)$ to an initial state $\mathbf{u}_0$. The action of $\hat{\mathbf{L}}_c$ is numerically approximated by the time-stepper that computes the response of the system governed by the linearized Navier-Stokes equations forced by $\mathsf{f}(t)$ with a zero initial condition. The second operator, the observability operator $\hat{\mathbf{L}}_o$, provides a dual action and maps the state $\mathbf{u}_0$ to future outputs, $\hat{\mathbf{L}}_o : \mathbb{U} \rightarrow L^2[0, +\infty)$; it is defined as

$$\mathsf{y}(t) = \hat{\mathbf{L}}_o \mathbf{u}_0 = \hat{\mathbf{C}}\mathbf{T}(t)\mathbf{u}_0 \qquad t \geq 0. \tag{36}$$

Using the above definitions, the Hankel operator can be seen as the combination of the two operators

$$\hat{\mathbf{H}} = \hat{\mathbf{L}}_o \hat{\mathbf{L}}_c. \tag{37}$$

Note that the operator $\hat{\mathbf{H}}$ has at most rank n for a state space of order n. Indeed, an input is driven via $\hat{\mathbf{L}}_c$ to an initial state $\mathbf{u}_0$ and each output can be determined from the knowledge of the state $\mathbf{u}_0$. Since each state $\mathbf{u}_0$ is determined uniquely from an input, two linearly independent states will produce two linearly independent future outputs; thus, the rank of the operator $\hat{\mathbf{H}}$ cannot exceed the dimension of the state space n.

C.1. *Adjoint operators*

Using the adjoint of the inputs and outputs introduced in 23 and 24, respectively, it is possible to define the adjoint of the controllability operator $\hat{\mathbf{L}}_c : L^2(-\infty, 0] \rightarrow \mathbb{U}$ and the observability operator $\hat{\mathbf{L}}_o : \mathbb{U} \rightarrow L^2[0, \infty)$. To this end, we introcuce the inputs vector $\mathsf{t} = (\mathsf{z}^*, \mathsf{v}^*) \in \mathbb{R}^{(p+k)}$, and the outputs vector $\mathsf{e} = (\mathsf{w}^*, \phi^*, \mathsf{g}^*) \in \mathbb{R}^{(m+2)}$. The adjoint of the controllability operator $\hat{\mathbf{L}}_c^* : \mathbb{U} \rightarrow L^2(-\infty, 0]$ maps an initial adjoint state $\mathbf{p}_0 \in \mathbb{U}$ to a signal e at time $-t$

$$\mathsf{e}(-t) = \hat{\mathbf{L}}_c^* \mathbf{p}_0 = \hat{\mathbf{B}}^* \mathbf{T}^*(-t)\mathbf{p}_0 \tag{38}$$

The adjoint of the observability operator $\hat{\mathbf{L}}_o^* : \hat{L}^2[0, \infty) \rightarrow \mathbb{U}$ drives the input signal t to the reference state $\mathbf{p}_0$

$$\mathbf{p}_0 = \hat{\mathbf{L}}_o^* \mathsf{t}(t) = \int_{0}^{\infty} \mathbf{T}^*(s)\hat{\mathbf{C}}^* \mathsf{t}(s)\,\mathrm{d}s \tag{39}$$

The direct mapping from the inputs t to the outputs e can be obtained combining $\hat{\mathbf{L}}_o^*$ and $\hat{\mathbf{L}}_c^*$; the adjoint Hankel $\hat{\mathbf{H}}^* : L^2[0, \infty) \rightarrow L^2(-\infty, 0]$ operator is thus defined as

$$\mathsf{e}(-t) = \hat{\mathbf{H}}^* \mathsf{t}(t) = \hat{\mathbf{L}}_c^* \hat{\mathbf{L}}_o^* \mathsf{t}(t) = \int_{0}^{\infty} \hat{\mathbf{B}}^* \mathbf{T}^*\left(s - t\right)\hat{\mathbf{C}}^* \mathsf{t}(s)\,\mathrm{d}s \tag{40}$$

Finally, introducing $\hat{\mathbf{B}}^*$ and $\hat{\mathbf{C}}^*$ in the initial value problem 28, the dual input-output system can be defined as

$$
\begin{aligned}
-\dot{\mathbf{p}} &= \hat{\mathbf{A}}^*\mathbf{p} + \hat{\mathbf{C}}^*\mathsf{t} && (41)\\
\mathsf{e} &= \hat{\mathbf{B}}^*\mathbf{p}. && (42)
\end{aligned}
$$

In the adjoint system, the roles of $\hat{\mathbf{B}}$ and $\hat{\mathbf{C}}$ have been exchanged: the system is now forced by the outputs t, while the inputs are extracted as measurements.

C.2. *Balanced modes*

Using the Hankel operator and the related adjoint operator, we can quantify the output energy obtained from a past input $\mathsf{f}(t)$, by

$$
\|\mathsf{y}\|^2_{L^2[0,\infty)} = \langle \hat{\mathbf{H}}\mathsf{f}, \hat{\mathbf{H}}\mathsf{f}\rangle_{L^2[0,\infty)} = \langle \mathsf{f}, \hat{\mathbf{H}}^*\hat{\mathbf{H}}\mathsf{f}\rangle_{L^2(-\infty,0]}. \tag{43}
$$

If a given input forcing $\mathsf{f}_i(t)$ is a unit-norm eigenvector of $\hat{\mathbf{H}}^*\hat{\mathbf{H}}$, then the output energy will be given by the square of the corresponding Hankel Singular Value (HSV) σ_i

$$
\hat{\mathbf{H}}^*\hat{\mathbf{H}}\mathsf{f}_i(t) = \sigma_i^2\mathsf{f}_i(t). \tag{44}
$$

The HSVs are real and positive; thus, they can be ranked according to the associated energy amplification. Multiplying 44 from left with $\hat{\mathbf{L}}_c$, we get

$$
\hat{\mathbf{L}}_c\hat{\mathbf{H}}^*\hat{\mathbf{H}}\mathsf{f}_i(t) = \underbrace{\hat{\mathbf{L}}_c\hat{\mathbf{L}}_c^*}_{\mathbf{P}}\underbrace{\hat{\mathbf{L}}_o^*\hat{\mathbf{L}}_o}_{\mathbf{Q}}\underbrace{\hat{\mathbf{L}}_c\mathsf{f}_i}_{\sigma_i\boldsymbol{\phi}_i} = \sigma_i^2(\sigma_i\boldsymbol{\phi}_i) \tag{45}
$$

where we have defined the balanced mode $\boldsymbol{\phi}_i$ associated with σ_j as

$$
\boldsymbol{\phi}_i = \frac{1}{\sigma_i}\hat{\mathbf{L}}_c\mathsf{f}_i \tag{46}
$$

and the controllability Gramian $\mathbf{P}$ and the observability Gramian $\mathbf{Q}$ as

$$
\begin{aligned}
\mathbf{P} &= \hat{\mathbf{L}}_c\hat{\mathbf{L}}_c^* = \int_0^\infty \mathbf{T}(\tau)\hat{\mathbf{B}}\hat{\mathbf{B}}^*\mathbf{T}^*(\tau)\mathrm{d}\tau && (47a)\\
\mathbf{Q} &= \hat{\mathbf{L}}_o^*\hat{\mathbf{L}}_o = \int_0^\infty \mathbf{T}^*(\tau)\hat{\mathbf{C}}^*\hat{\mathbf{C}}\mathbf{T}(\tau)\mathrm{d}\tau. && (47b)
\end{aligned}
$$

The balanced modes are thus the eigenvectors of the product of the observability $\mathbf{Q}$ and controllability Gramians $\mathbf{P}$, written in matrix form,

$$
(\mathbf{PQ})\boldsymbol{\Phi} = \boldsymbol{\Phi}\Sigma^2, \tag{48}
$$

$\boldsymbol{\Phi} = (\boldsymbol{\phi}_1, \boldsymbol{\phi}_2, \ldots, \boldsymbol{\phi}_r)$ and $\Sigma^2 = \mathrm{diag}\{\sigma_1^2, \ldots, \sigma_r^2\}$. The set of left eigenvectors of $\mathbf{PQ}$ represents the adjoint balanced modes set, hereinafter denoted by $\boldsymbol{\Psi}$.

Two main reasons make the model reduction obtained by projection onto balanced modes particularly convenient:

1. the reduced-order system is guaranteed to be asymptotically stable if $\sigma_j \neq \sigma_{j+1}$ for all j (Pernebo & Silverman 1982);

2. tight error bounds exist (Glover 1984)

$$\sigma_{r+1} \leq \|\hat{\mathbf{G}} - \hat{\mathbf{G}}_r\|_\infty \leq 2 \sum_{j=r+1}^{n} \sigma_j, \tag{49}$$

where $\hat{\mathbf{G}}$ and $\hat{\mathbf{G}}_r$ are the input-output systems associated with 5 and 9, respectively, and $\|\hat{\mathbf{G}} - \hat{\mathbf{G}}_r\|_\infty$ is the infinity norm. More details about the operators introduced in the identification of the balanced mode are given by Glover (1984) or Dullerud & Paganini (1999).

C.3. *Snapshot method*

An essential ingredient in the computation of the balanced modes is the identification of the Gramians **P** and **Q**, usually evaluated as solution of Lyapunov equations, (Green & Limebeer 1995). Unfortunately, the solution of the Lyapunov equations involves a computational complexity $O(n^3)$ and a storage requirement $O(n^2)$ making it unfeasible for high-dimensional systems (Laub *et al.* 1987). An alternative is given by the *snapshot method* (Rowley 2005), where empirical Gramians are computed using the following quadratures

$$\hat{\mathbf{P}} \approx \sum_{j=1}^{n_t} \mathbf{T}(t_j)\hat{\mathbf{B}}\hat{\mathbf{B}}^*\mathbf{T}^*(t_j)\delta_j = \mathbf{X}\mathbf{X}^* \tag{50a}$$

$$\hat{\mathbf{Q}} \approx \sum_{j=1}^{n_t} \mathbf{T}^*(t_j)\hat{\mathbf{C}}^*\hat{\mathbf{C}}\mathbf{T}(t_j)\delta_j = \mathbf{Y}^*\mathbf{Y}. \tag{50b}$$

Here δ_j are the time quadrature weights, n_t the number of samplings, $\mathbf{X} \in \mathbb{R}^{n\times n_t m}$ and $\mathbf{Y} \in \mathbb{R}^{n\times n_t p}$ are the Cholesky factors

$$\mathbf{X} = [\mathbf{T}(t_1)\hat{\mathbf{B}}\sqrt{\delta_1}, \mathbf{T}(t_2)\hat{\mathbf{B}}\sqrt{\delta_2}, \ \ldots, \mathbf{T}(t_k)\hat{\mathbf{B}}\sqrt{\delta_{n_t}}] \tag{51a}$$

$$\mathbf{Y} = [\mathbf{T}^*(t_1)\hat{\mathbf{C}}^*\sqrt{\delta_1}, \mathbf{T}^*(t_2)\hat{\mathbf{C}}^*\sqrt{\delta_2}, \ \ldots, \mathbf{T}^*(t_k)\hat{\mathbf{C}}^*\sqrt{\delta_{n_t}}]. \tag{51b}$$

Each element of the Cholesky factor **X** contains snapshots of the flow field computed by the impulse response to each input $\hat{\mathbf{B}}_i$ at a given time t_j. Similarly, the Cholesky factor **Y** can be obtained by gathering the snapshots computed by marching backward in time with the adjoint system 27. Please note that the number of collected snapshots is n_t times the number of inputs (m) and output (p).

Using the low-rank Cholesky factors, the approximate direct and adjoint balanced modes can be computed as follows. As a first step, the singular values decomposition (SVD) of $\mathbf{Y}^*\mathbf{X}$ is formed,

$$\mathbf{Y}^*\mathbf{X} = \mathbf{U}\mathbf{\Sigma}\mathbf{V}^*. \tag{52}$$

The size of $\mathbf{Y}^*\mathbf{X}$ is $n_t p \times n_t m$; as long as the number of degree of freedom n is smaller than the number of collected snapshots, the method is cheaper than the standard method (using full Cholesky factors of size $n \times n$) . The diagonal matrix $\mathbf{\Sigma}$ contains the approximate HSVs. The direct and adjoint balanced modes are then given by

$$\mathbf{\Phi}_r = \mathbf{X}\mathbf{V}\mathbf{\Sigma}^{-1/2} \qquad \mathbf{\Psi}_r = \mathbf{Y}^*\mathbf{U}\mathbf{\Sigma}^{-1/2}. \tag{53}$$

Here, only time quadrature weights were considered; however, note that spatial integral weights are introduced when inner product are computed, see (Bagheri *et al.* 2009*a*). In general, numerical tests (Ilak & Rowley 2008; Ahuja 2009; Bagheri *et al.* 2009*a*) have shown that the approximate balanced modes are a good approximation to exact balancing modes and that Σ_r are close to the true HSVs. This can be attributed to the low numerical rank of the Gramians, when $m, p \ll n$.

References

Ahuja, S. 2009 Reduction methods for feedback stabilization of fluid flows. PhD thesis, Princeton University, New Jersey.

Ahuja, S. & Rowley, C. W. 2010 Feedback control of unstable steady states of flow past a flat plate using reduced-order estimators. *J. Fluid Mech.* **645**, 447–478.

Åkervik, E., Ehrenstein, U., Gallaire, F. & Henningson, D. S. 2008 Global two-dimensional stability measures of the flat plate boundary-layer flow. *Eur. J. Mech. B/Fluids* **27**, 501–513.

Anderson, B. & Moore, J. 1990 *Optimal control: Linear Quadratic Methods*. Prentice Hall, New York.

Bagheri, S., Åkervik, E., Brandt, L. & Henningson, D. S. 2009*a* Matrix-free methods for the stability and control of boundary layers. *AIAA J.* **47**, 1057–1068.

Bagheri, S., Brandt, L. & Henningson, D. S. 2009*b* Input-output analysis, model reduction and control design of the flat-plate boundary layer. *J. Fluid Mech.* **620**, 263–298.

Bagheri, S., Hœpffner, J., Schmid, P. J. & Henningson, D. S. 2009*c* Input-output analysis and control design applied to a linear model of spatially developing flows. *Appl. Mech. Rev.* **62** (2).

Bamieh, B., Paganini, F. & Dahleh, M. 2002 Distributed control of spatially invariant systems. *IEEE Trans. Automat. Control* **47** (7), 1091–1107.

Barbagallo, A., Sipp, D. & Schmid, P. J. 2009 Closed-loop control of an open cavity flow using reduced-order models. *J. Fluid Mech.* **641**, 1–50.

Bewley, T. R. 2001 Flow control: New challenges for a new renaissance. *Progr. Aerospace. Sci.* **37**, 21–58.

Bewley, T. R. & Liu, S. 1998 Optimal and robust control and estimation of linear paths to transition. *J. Fluid Mech.* **365**, 305–349.

Bewley, T. R., Moin, P. & Temam, R. 2001 DNS-based predictive control of turbulence: An optimal benchmark for feedback algorithms. *J. Fluid Mech.* **447**, 179–225.

Butler, K. & Farrell, B. F. 1992 Three-dimensional optimal perturbations in viscous shear flow. *Phys. Fluids A* **4**, 1637–1650.

Chevalier, M., Hœpffner, J., Åkervik, E. & Henningson, D. S. 2007*a* Linear feedback control and estimation applied to instabilities in spatially developing boundary layers. *J. Fluid Mech.* **588**, 163–187.

Chevalier, M., Hœpffner, J., Bewley, T. R. & Henningson, D. S. 2006 State estimation in wall-bounded flow systems. Part 2: Turbulent flows. *J. Fluid Mech.* **552**, 167–187.

Chevalier, M., Schlatter, P., Lundbladh, A. & Henningson, D. S. 2007*b* A pseudo spectral solver for incompressible boundary layer flows. Trita-Mek 7. KTH Mechanics, Stockholm, Sweden.

Choi, H., Moin, P. & Kim, J. 1993 Direct numerical simulation of turbulent flow over riblets. *J. Fluid Mech.* **255**, 503–539.

Chomaz, J. M. 2005 Global instabilities in spatially developing flows: Non-normality and nonlinearity. *Ann. Rev. Fluid Mech.* **37**, 357–392.

Cortelezzi, L., Speyer, J. L., Lee, K. H. & Kim, J. 1998 Robust reduced-order control of turbulent channel flows via distributed sensors and actuators. *IEEE 37th Conf. on Decision and Control* pp. 1906–1911.

Curtain, R. & Zwart, H. 1995 *An introduction to infinite-dimensional linear systems theory*. New York: Springer Verlag.

Doyle, J. C. 1978 Guaranteed margins for LQG regulators. *IEEE Trans. Automat. Control* **23**, 756–757.

Doyle, J. C., Glover, K., Khargonekar, P. P. & Francis, B. A. 1989 State-space solutions to standard H_2 and H_∞ control problems. *IEEE Trans. Automat. Control* **34**, 831–847.

Dullerud, E. G. & Paganini, F. 1999 *A course in robust control theory. A convex approach*. Springer Verlag, New York.

Glover, K. 1984 All optimal Hankel-norm approximations of linear multivariable systems and the l^∞-error bounds. *Int. J. Control* **39**, 1115–1193.

Green, M. & Limebeer, J. N. 1995 *Linear Robust Control*. Prentice Hall, New Jersey.

Grundmann, S. & Tropea, C. 2008 Active cancellation of artificially introduced Tollmien–Schlichting waves using plasma actuators. *Exp. Fluids* **44** (5), 795–806.

Hammond, E. P., Bewley, T. R. & Moin, P. 1998 Observed mechanisms for turbulence attenuation and enhancement in opposition-controlled wall-bounded flows. *Phys. Fluids* **10** (9), 2421–2423.

Ho, C. M. & Tai, Y. 1998 Micro-electro-mechanical systems MEMS and fluid flows. *Ann. Rev. Fluid Mech.* **30**, 579–612.

Högberg, M. & Bewley, T. R. 2000 Spatially localized convolution kernels for feedback control of transitional flows. *IEEE 39th Conf. on Decision and Control* **3278-3283**.

Högberg, M., Bewley, T. R. & Henningson, D. S. 2003*a* Linear feedback control and estimation of transition in plane channel flow. *J. Fluid Mech.* **481**, 149–175.

Högberg, M., Bewley, T. R. & Henningson, D. S. 2003*b* Relaminarization of $re_tau = 100$ turbulence using gain scheduling and linear state-feedback control flow. *Phys. Fluids* **15**, 3572–3575.

Holmes, P., Lumley, J. & Berkooz, G. 1996 *Turbulence Coherent Structuresm Dynamical Systems and Symmetry*. Cambridge University Press.

Ilak, M., Bagheri, S., Brandt, L., Rowley, C. W. & Henningson, D. 2010 Model reduction of the nonlinear complex Ginzburg-Landau equation. *SIAM J. Applied Dynamical Systems* In press.

Ilak, M. & Rowley, C. W. 2008 Modeling of transitional channel flow using balanced proper orthogonal decomposition. *Phys. Fluids* **20**, 034103.

Joshi, S. S., Speyer, J. L. & Kim, J. 1997 A systems theory approach to the feedback stabilization of infinitesimal and finite-amplitude disturbances in plane poiseuille flow. *J. Fluid Mech.* **332**, 157–184.

Kalman, R. E. 1960 A new approach to linear filtering and prediction problems. *Trans. ASME, Ser. D. J. Basic Eng.* **82**, 24–45.

Laub, A. 1991 Invariant subspace methods for the numerical solution of riccati equations. In *The Riccati equation* (ed. W. Bittaini, Laub), pp. 163–96. Berlin: Springer.

Laub, A., Heath, M., Paige, C. & Ward, R. 1987 Computation of system balancing transformations and other applications of simultaneous diagonalization algorithms. *IEEE Trans. Automat. Control* **32** (2), 115–122.

Lewis, F. L. & Syrmos, L. V. 1995 *Optimal Control*. John Wiley & Sons, New York.

Lundell, F. 2003 Pulse-width modulated blowing/suction as a flow control actuator. *Experiments in Fluids* **35**, 502–504.

Lundell, F. 2007 Reactive control of transition induced by free-stream turbulence: An experimental demonstration. *J. Fluid Mech.* **585**, 41–71.

Ma, Z., Ahuja, S. & Rowley, C. W. 2009 Reduced order models for control of fluids using the Eigensystem Realization Algorithm. *Theoret. Comput. Fluid Dyn.* In press.

Milling, W. 1981 Tollmien–Schlichting wave cancellation. *Phys. Fluids* **24** (5), 979–981.

Monokrousos, A., Åkervik, E., Brandt, L. & Henningson, D. S. 2010*a* Global optimal disturbances in the blasius boundary-layer flow using time-steppers. *J. Fluid Mech.* **650**, 181–214.

Monokrousos, A., Brandt, L., Schlatter, P. & Henningson, D. S. 2008 DNS and LES of estimation and control of transition in boundary layers subject to free-stream turbulence. *Int. J. Heat Fluid Flow* **29** (3), 841–855.

Monokrousos, A., Lundell, F. & Brandt, L. 2010*b* Feedback control of boundary layer bypass transition: comparison of a numerical study with experiments. To appear.

Moore, B. 1981 Principal component analysis in linear systems: Controllability, observability, and model reduction. *IEEE Trans. Automat. Control* **26** (1), 17–32.

Nordström, J., Nordin, N. & Henningson, D. S. 1999 The fringe region technique and the fourier method used in the direct numerical simulation of spatially evolving viscous flows. *SIAM J. Sci. Comput.* **20** (4), 1365–1393.

Pang, J. & Choi, K.-S. 2004 Turbulent drag reduction by lorentz force oscillation. *Phys. Fluids* **16** (5), L35–L38.

Pernebo, L. & Silverman, L. 1982 Model reduction via balanced state space representations. *IEEE Trans. Automat. Control* **27**, 382–387.

Quadrio, M. & Ricco, P. 2004 Critical assessment of turbulent drag reduction through spanwise wall oscillations. *J. Fluid Mech.* **521**, 251–271.

Rempfer, D. & Fasel, H. 1994 Evolution of three-dimensional coheren structures in a flat-plate boundary layer. *J. Fluid. Mech.* **260**, 351–375.

Rowley, C. W. 2005 Model reduction for fluids using balanced proper orthogonal decomposition. *Int. J. Bifurc. Chaos* **15** (3), 997–1013.

Schlichting, H. & Gersten, K. 2000 *Boundary-Layer Theory*. Springer Verlag, Heidelberg.

Semeraro, O., Bagheri, S., Brandt, L. & Henningson, D. S. 2010 Linear control of 3D disturbances on a flat-plate. In *Seventh IUTAM Symposium on Laminar-Turbulent Transition* (eds. P. Schlatter & D. S. Henningson), , vol. 18. Springer.

Skogestad, S. & Postlethwaite, I. 2005 *Multivariable Feedback Control, Analysis to Design*, 2nd edn. Wiley.

Smith, B. L. & Glezer, A. 1998 The formation and evolution of synthetic jets. *Phys. Fluids* **10** (9), 2281–2297.

Sturzebecher, D. & Nitsche, W. 2003 Active cancellation of Tollmien–Schlichting waves instabilities on a wing using multi-channel sensor actuator systems. *Int. J. Heat Fluid Flow* **24**, 572–583.

Tempelmann, D., Hanifi, A. & Henningson, D. S. 2010 Optimal disturbances and receptivity in three-dimensional boundary layers. In *5th European Conference on Computational Fluid Dynamics*. Lisbon, Portugal.

White, E. & Saric, W. 2000 Application of variable leading-edge roughness for transition control on swept wings. *AIAA Paper 2000-283, 38th AIAA Aerospace Sciences Meeting and Exhibit* .

Zhou, K., Doyle, J. C. & Glover, K. 2002 *Robust and Optimal Control*. Prentice Hall, New Jersey.

Zhou, K., Salomon, G. & Wu, E. 1999 Balanced realization and model reduction for unstable systems. *Int. J. Robust Nonlinear Control* **9**, 183–198.

Paper 2

Transition delay in boundary layer flow using feedback control

By Onofrio Semeraro, Shervin Bagheri, Luca Brandt & Dan S. Henningson

Linné Flow Centre, KTH Mechanics
SE-100 44 Stockholm, Sweden

To be submitted - Journal of Fluid Mechanics

We apply feedback control to delay laminar-turbulent transition in boundary-layer flows. The dynamics of the flow is analysed from the input-output point of view: spatially localized sensors and actuators are distributed near the wall in arrays spanning the homogeneous span-wise direction. Reduced-order models of the linearized Navier-Stokes equations, including the inputs and outputs, are built via balanced truncation and used to design an LQG controller. The controller provides an optimal signal that minimizes the amplitude of the perturbation downstream. Using a limited number of sensors and actuators (10 to 20 elements), the controller quenches packets of Tollmien-Schilchting waves and reduces substantially their energy growth. We demonstrate that using a linear controller the laminar-turbulent transition is delayed for realistic amplitudes of the initial perturbation, such that transition occurs for $Re_x = 1.5 - 2 \times 10^6$. Effect of the actuation on the disturbances and the effort of the controller is characterized in the nonlinear regime.

---

1. Introduction

Transition from laminar to turbulent flow originating from the growth of Tollmien-Schlichting (TS) wavepackets is considered; this scenario - usually referred as classical transition - is usually observed in clean environments characterized by low levels of free stream turbulence (smaller than 1%). Higher values of free-stream turbulence involve other mechanisms and the classical scenario is by-passed. However, the TS scenario is still of remarkable interest from the technological point of view, for instance in aerodynamic flows around a wing, typically characterized by clean environment and low turbulence level. In that sense, the control of wall-bounded transitional flows has high potential benefits and outcomes; any reduction of aerodynamic drag - for instance - can lead to relevant reduction of the operational cost of cargo ships or commercial aircraft (Kim & Bewley 2007). The large sensitivity of wall bounded transitional and turbulent flows allows to manipulate the global flow using local perturbation acting on only small parts of it with a small amount of energy.

Moreover, it is now well established that under certain conditions the initial phase of the laminar-turbulent transition in wall-bounded flows is largely governed by linear mechanisms (Schmid & Henningson 2001). Thus, the tools of linear control theory may provide efficient, robust and feasible controllers to delay transition to turbulence.

The majority of experimental flow control studies have used control laws based on physical intuition and trial-and-error basis, while in recent years flow control has progressively developed toward more systematic approach. The application of the control theory as a tool for flow control emerged in the works by Joshi *et al.* (1997), Cortelezzi *et al.* (1998) and Bewley & Liu (1998), who paved the way for future researchers. Several groups have applied the control theory to simplified models (Lauga & Bewley 2003, 2004; Cohen *et al.* 2005; Bagheri *et al.* 2009) and wall-bounded shear flows using direct numerical simulations (DNS) (Joshi *et al.* 1997; Bewley & Liu 1998; Högberg & Henningson 2002; Högberg *et al.* 2003). For a thorough review of the applications, the reader is also referred to the reviews by Bewley (2001) and Kim & Bewley (2007).

As suggested by Bewley (2001), the only requirement to achieve the desired flow behavior is that suitable control signals are determined based on filtered information delivered from the sensor. Thus, it is necessary to describe the relation among the inputs and the outputs *time signals* for an efficient control design. A general input-output framework was developed in Bagheri *et al.* (2009*a*), where the disturbance and actuators were considered as inputs, and the objective function and sensors were considered as outputs. The approach is based on approximating the complex high-dimensional system that arise from discretization of the Navier-Stokes equations with a low-order model. Using approximate balanced truncation (Rowley 2005), a low-order system preserving the dynamics between the actuators and sensors is built; finally, the design of the controller is based on the resulting simpler model. Semeraro *et al.* (2010) extended the analysis to a fully three-dimensional (3D) configuration and demonstrated that the perturbation energy can be substantially mitigated using localized actuation and sensing; indeed, the control setup was based on a set of localized actuators and sensors distributed near the wall resembling actual experimental setups (see for instance Lundell (2007); Sturzebecher & Nitsche (2003)).

Although successful, these previous investigations considered perturbations governed by linearized equations. In the present work we examine the effect of linear feedback control in the full nonlinear regime with finite-amplitude perturbations effectively leading to transition to turbulence. The same configuration as in Semeraro *et al.* (2010) is now used in nonlinear simulations. The remarkable energy reduction results in a delay of the initial stages of the laminar-turbulent transition. We investigate the effects of the actuation on the flow, when a stronger actuation is employed and the initial perturbation amplitude is increased. The localization of the actuators and sensors, together with a more detailed analysis of the manipulated flow is essential for an experimental application. Numerical investigations can be useful for wind-tunnel experiments, providing valuable information beforehand: experiments can be designed after evaluating a large number of numerical simulations.

This paper is organized as follows. In section 2 the problem is introduced with a short description of the configuration. The input-output system, the model reduction problem and the feedback control are briefly summarized. In section 3, the transition delay is discussed considering the results achieved in the simulations performed for this paper. A short parametric analysis is also introduced. The effects of the actuation are further discussed in section 4, where the energy spectra are analysed. The paper finalizes with conclusions in section 5.

2. Input-output system, model reduction, feedback control: an overview

The dynamics and control of finite-amplitude perturbation in a viscous, incompressible flow over a flat plate are considered. The velocity field is denoted with $\overline{\mathbf{u}}(\mathbf{x},t) = (\overline{u},\overline{v},\overline{w})^T$ and is governed by the Navier–Stokes equations; x, y and z denote the stream-wise, cross-stream and span-wise coordinates, respectively. The Reynolds number is defined as $Re = U_\infty \delta_0^*/\nu$, where δ_0^* is the displacement thickness at the inflow position, U_∞ is the uniform free-stream velocity and ν is the kinematic viscosity. All the simulations considered in the paper were performed at $Re_{\delta_0^*} = 1000$, corresponding to $Re_x \approx 3 \times 10^5$ at the computational inlet. For all the simulations, Dirichlet conditions enforce zero perturbations velocity in the freestream ($y = L_y$) and at the wall ($y = 0$). Finally, periodicity is assumed in the span-wise direction and enforced in the stream-wise direction in a fringe region at the outlet of the domain (Nordström *et al.* 1999).

The results presented in this paper were computed with a pseudo-spectral code (Chevalier *et al.* 2007). Large eddy simulation (LES) were performed using the ADM-RT subgrid-scale model for the simulation of transition; ADM-RT model proved to be accurate and robut in predicting transitional and turbulent flows with spectral methods (Schlatter *et al.* 2004, 2006). Note, however, that the subgrid-scale model (SGS) term is effectively active only when the flow becomes turbulent. An application of LES in flow control, using the same numerical method, is discussed by Monokrousos *et al.* (2008), where comparison with full DNS are carried out.

The action of the actuators and the dynamics of the controlled and uncontrolled flows were first analysed in a short box $[L_x, L_y, L_z] = (1000, 30, 256)$; for those tests, a resolution of $768 \times 101 \times 256$ was deemed sufficient for getting converged results. Finally, the transition delay was studied in a longer box $[L_x, L_y, L_z] = (2000, 30, 256)$, with a resolution $1536 \times 101 \times 256$.

A linear feedback control based on the linearized Navier-Stokes system is designed to quench the perturbations growing in the boundary layer. In Semeraro *et al.* (2010), control of three-dimensional (3D) disturbances in a

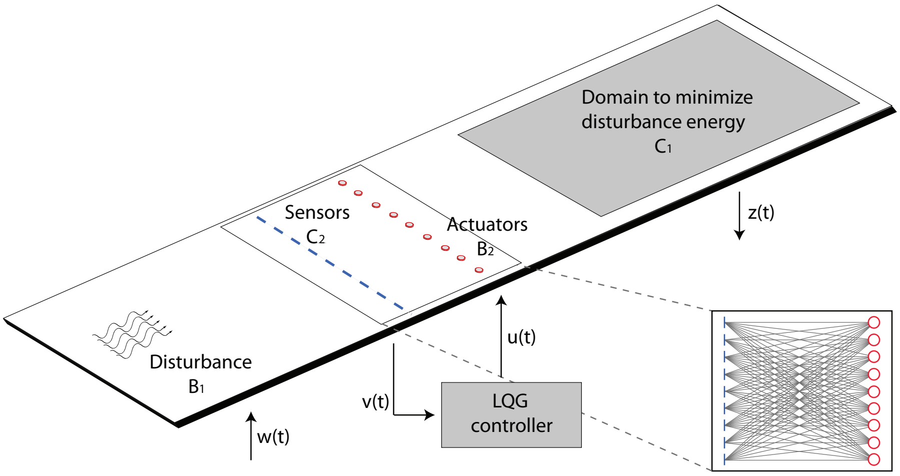

FIGURE 1. Sketch of the configuration. The initial condition $\mathbf{B}_1$ is optimal and triggers packets of TS-wave. The control action is provided by the input $\mathbf{B}_2$, constituted by a row of actuators located at $x = 400$. The output $\mathbf{C}_2$ at $x = 300$ contains an array of sensors used for flow estimation. The effect of the controller is quantified in a region spanned by 10 POD modes (here indicated with a darker grey region). All the estimation sensors are connected to all the actuators, as sketched in the inset (*centralized control*).

boundary layer flow is examined within a linear framework. Similar strategy is now employed for the transition delay.

2.1. *Input-output system*

The first step is the linearization of the Navier-Stokes equations around a steady state $\mathbf{U}(\mathbf{x},t) = (U(x,y), V(x,y), 0)$. Indicating the inputs with $\mathbf{B}_1$ and $\mathbf{B}_2$, and the outputs with $\mathbf{C}_1$ and $\mathbf{C}_2$, the system can be rewritten as

$$\begin{aligned}\dot{\mathbf{u}}(t) &= \mathbf{A}\mathbf{u}(t) + \mathbf{B}_1\mathsf{w}(t) + \mathbf{B}_2\phi(t) && (1a)\\ \mathsf{z}(t) &= \mathbf{C}_1\mathbf{u}(t) + I_l\phi(t) && (1b)\\ \mathsf{v}(t) &= \mathbf{C}_2\mathbf{u}(t) + I_\eta\mathsf{g}(t). && (1c)\end{aligned}$$

where $\mathbf{A}$ is obtained from the discretization of the linearized Navier-Stokes including the boundary conditions, governing the perturbation velocity field $\mathbf{u} = (u, v, w)$.

In figure 1 a sketch of the configuration is provided; the disturbance is introduced upstream by a localized initial condition $\mathbf{B}_1$. This optimal initial condition is obtained in Monokrousos *et al.* (2010) and consists of a packet of TS waves. The second input $\mathbf{B}_2 \in \mathbb{R}^{n\times m}$ consists of an array of $m = 9$ actuators placed at $x = 400$. Each element is equidistant each other ($\Delta_z = 20$) and described by an analytical Gaussian function. The temporal forcing of the inputs is provided by the time signals $\mathsf{w} \in \mathbb{R}$, $\mathsf{g} \in \mathbb{R}$ and $\phi \in \mathbb{R}^m$.

The measurements extracted from the sensors provide us information about the flow; the signal $\mathsf{v}(t) \in \mathbb{R}^p$ is extracted by $p = 9$ sensors, $\mathbf{C}_2$, located a short distance upstream of the actuators, at $x = 300$; the configuration of the sensors array is the same as that characterizing the actuators line. The resulting measurement signal $\mathsf{v}(t)$ is the spatial integral of the velocity field $\mathbf{u}$ weighted with the Gaussian function that spatially describes the sensor. The vector $I_\eta \in \mathbb{R}^p$ contains the *noise contamination* parameter η, which accounts for the accuracy of the measurements.

Finally, the signal $\mathsf{z}(t) \in \mathbb{R}^k$ – measured by $\mathbf{C}_1 \in \mathbb{R}^{k\times n}$ – provides information on the controller performance; all the entries of the matrix $I_l \in \mathbb{R}^{k\times m}$ are represented by the parameter l, related to the effort of the controller. Large values of l indicate higher control costs and therefore weaker actuation. The final goal is to determine a control signal $\phi(t)$ using the noisy measurements $\mathsf{v}(t)$ so that the perturbation energy of the flow is minimized in the region defined by $\mathbf{C}_1$. The criterion is expressed by the following objective function

$$\|\mathsf{z}\|^2_{L^2(0,T)} = \int_0^T \|\mathbf{C}_1\mathbf{u}\|^2_\Omega + \phi^T I_l^T I_l \phi \,\mathrm{d}t. \tag{2}$$

The basis for $\mathbf{C}_1$ is a sequence of proper orthogonal decomposition (POD) modes, generated by a dataset of snapshots collected from the impulse response to the initial condition $\mathbf{B}_1$. The first 10 modes are able to capture about the 93% of the total flow energy and were deemed sufficient to characterize $\mathbf{C}_1$.

2.2. *Model reduction and feedback control design*

Among all the possible flow disturbances, only a portion can be excited by the inputs and observed by the outputs; in literature, these states are referred as *controllable* and *observable*. With a limited number of inputs and outputs most part of the states is scarcely controllable and observable. Since the control design is based on the dynamics among actuators and sensors, one way to proceed is to disregard uncontrollable/unobservable states. In such a way, the entire input-output behaviour of the system can be accurately reproduced by a reduced number of states. Balanced truncation, first proposed by Moore (1981), represents a systematic way to perform this reduction. We refer to Glover (1984) and Bagheri *et al.* (2009*a*) for more details. For our application, an approximate basis of balanced modes - and the related adjoint set - is computed using a snapshot-based method, see Rowley (2005). For this configuration, a set composed by 60 modes was deemed sufficient for reconstruct properly the entire input-output behaviour of the system, as shown by Semeraro *et al.* (2010).

The reduced order model allows us to easily access the tools of linear control for the compensator design. The controller is designed using the linear

Case	Amplitude	Control pen.	Tran. delay.	Reynolds Num.
	$u_{max}\|_{t=0}$	l	Δx	ΔRe_x
A	3.2×10^{-4}	150	$\approx$465	4.7×10^5
B	3.2×10^{-4}	250	$\approx$545	5.4×10^5
C	3.2×10^{-4}	300	$\approx$580	5.8×10^5
D	4.3×10^{-4}	150	$\approx$180	1.8×10^5
E	4.3×10^{-4}	250	$\approx$295	3.0×10^5
F	4.3×10^{-4}	300	$\approx$355	3.6×10^5
G	5.4×10^{-4}	150	No	No
H	5.4×10^{-4}	250	$\approx$140	1.4×10^5
I	5.4×10^{-4}	300	$\approx$210	2.1×10^5

Table 1. Test cases for the parametric analysis of the transition delay; the parameters used are the control penalty l and the initial amplitude. The performance is compared considering the achieved transition delay in terms of Δx and ΔRe_x. In all the uncontrolled cases related to these amplitudes we observed transition to turbulence.

quadratic Gaussian (LQG) approach and is of the same order of the model. The so-called compensator consists of an estimator, that provides an estimation of the flow, and the controller that feeds the actuators. For a derivation of the LQG solution, please refer to e.g. Lewis & Syrmos (1995) or Doyle *et al.* (1989) and Dullerud & Paganini (1999) for a more "modern" robust control framework. Here, we just mention that the spatial localization of the actuators and the sensors requires a proper multi-input-multi-output (MIMO) approach for the controller design. Here a *centralized control* is adopted, where all the actuators are connected to all the sensors. This configuration results in a stable closed-loop. Since the perturbation propagates in the span-wise direction, while travelling downstream Monokrousos *et al.* (2010), it has a strong correlation in this direction. Thus, a controller where each sensor is connected only to the actuator farther downstream is unfeasible since the coupling in the span-wise direction is disregarded.

3. Transition delay

As already introduced, the classical transition scenario is usually observed in clean environments characterized by low levels of free stream turbulence. The transition is here triggered by the growing of three dimensional wavepacket with realistic amplitudes; indeed, all the uncontrolled simulations related to the three initial amplitudes listed in table 1 allow to obtain transition in the end of the computational box. At this location, the TS amplitude is about 0.03% of the free stream velocity and $Re_x \approx 1.6-2.0 \times 10^6$. In table 1, 9 cases are reported; a parametric analysis is performed using different controllers (varying the penalty l) and three different initial amplitudes. The controllers used for the transition

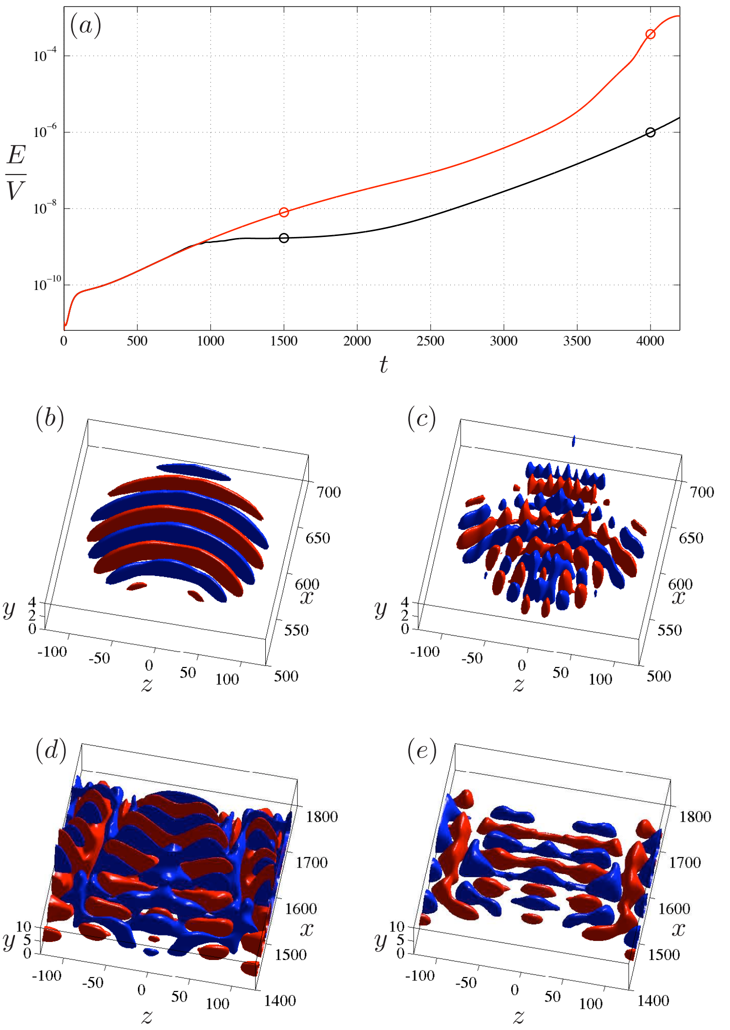

FIGURE 2. Evolution of the energy-density, (*a*). With a red line the uncontrolled case is indicated, while the black line indicates the controlled case. The circles denote the position of the leading edge of the disturbance. Snapshots for the streamwise velocity are shown at $t = 1250$, (*b*) and (*c*), and at $t = 3750$, (*d*) and (*e*), for the uncontrolled case and the controlled case, respectively; the surface contour corresponds to the 30% of the maximum perturbation velocity for each case.

delay are designed in the shorter box, $L_x = 1000$; their performance is presented in Semeraro *et al.* (2010) for linear perturbations, where the best performance achieved was a reduction of 93% of the peak energy. To investigate transition delay, a longer box is now used, where the controller acts when the flow is still laminar but weakly non-linear. However, this computational domain is still characterized by the same width; in principle, due to the spanwise elongation of the TS-wavepacket, a large domain should be introduced. However, little changes are observed in the physical behaviour of the propagating disturbance although interaction due to the periodicity in z is observed. Moreover, in a realistic case, a random distribution of disturbances is expected interaction, leading to an interaction between the disturbance spots.

The transition delay obtained for case F is shown in figure 2(a), where the energy evolution in time is depicted and compared with the corresponding uncontrolled case. The energy is scaled with the total volume of the computational domain. Initially, the disturbance extracts energy from the mean flow via the Orr-mechanism: the initial condition is tilted in the upstream direction. During the early stage, the structure rotates until it is aligned with the shear. Farther downstream, the wavepacket propagates spreading progressively along the span-wise direction and growing in size; the resulting structure is nearly two-dimensional, as shown in figure 2*b*, where a snapshot of the stream-wise component is depicted at $t = 1250$. When the control is active, the perturbation has already experienced the effects of the actuation at $t = 1250$: the original nearly two-dimensional structure is distorted into a more complicated three-dimensional pattern, see figure 2*c*. The span-wise coherence of the disturbance is disrupted and the perturbation energy is roughly one order of magnitude lower than in the uncontrolled case.

However, farther downstream of the actuation array, the perturbation recovers its span-wise coherence. This leads to renewed growth of the TS-wavepacket; indeed, the slope of the energy curve (see figure 2*a*) corresponds roughly that obtained for the uncontrolled case. Thus, it seems reasonable to evaluate the transition delay by extrapolating the transition location from the disturbance energy at this stage; the following disturbance evolution can be assumed to be the same for the two cases, only small differences due to higher Reynolds numbers in the uncontrolled case. To relate time to stream-wise location of transition, we assume that the leading edge of the wavepacket has a propagation velocity $c_e = 0.47$, see Monokrousos *et al.* (2010). Using this value, the delay is here provided in terms of Δx and ΔRe_x. For case F, $\Delta x \approx 355$, corresponding to a transition delay of $\Delta Re_x \approx 3.6 \times 10^5$. Table 1 summarizes the transition delay for all test cases.

At a later stage, the uncontrolled flow starts the transition to turbulence. The structure is now completely three-dimensional, as shown in figure 2*d*, and the energy curve strongly deviates from the linear behaviour previously observed, showing a rapid growth; conversely, the behaviour of the controlled

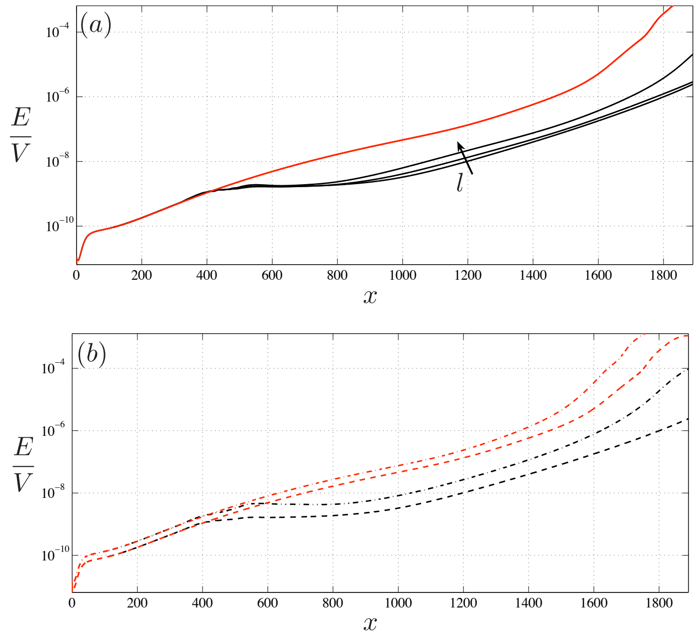

FIGURE 3. Energy-density evolution as function of x. In a the uncontrolled case (red line) is compared with cases D, E and F; the arrow indicates increasing values of l. In b, cases F (black, dashed line) and I (black, dashed-dotted line) are compared with the respective controlled case (red lines).

case is still essentially linear as confirmed by the energy growth and the analysis of the structure shown in figure 2e.

The localization of the actuators and sensors, the control penalties and the initial amplitudes provide a broad range of parameters for the analysis of the performance. The control penalty l and the initial amplitude of the disturbance are analysed in figure 3a and 3b, respectively, where the evolution of the energy-density is reported. The controller configuration – sketched in figure 1 – is fixed and the noise contamination $\eta = 0.01$. This configuration provides best performance in the linear simulations; we expect worsening of the controller behaviour when higher noise contamination is introduced.

The performance differs from the linear prediction when the control penalty l is changed. Indeed, a reduced control effort provides improved performance (see fig. 3a); in particular, cases E and D are characterized by a delay of the transition $\Delta x \approx 295$ (corresponding to $\Delta Re_x \approx 3.0 \times 10^5$) and $\Delta x \approx 180$

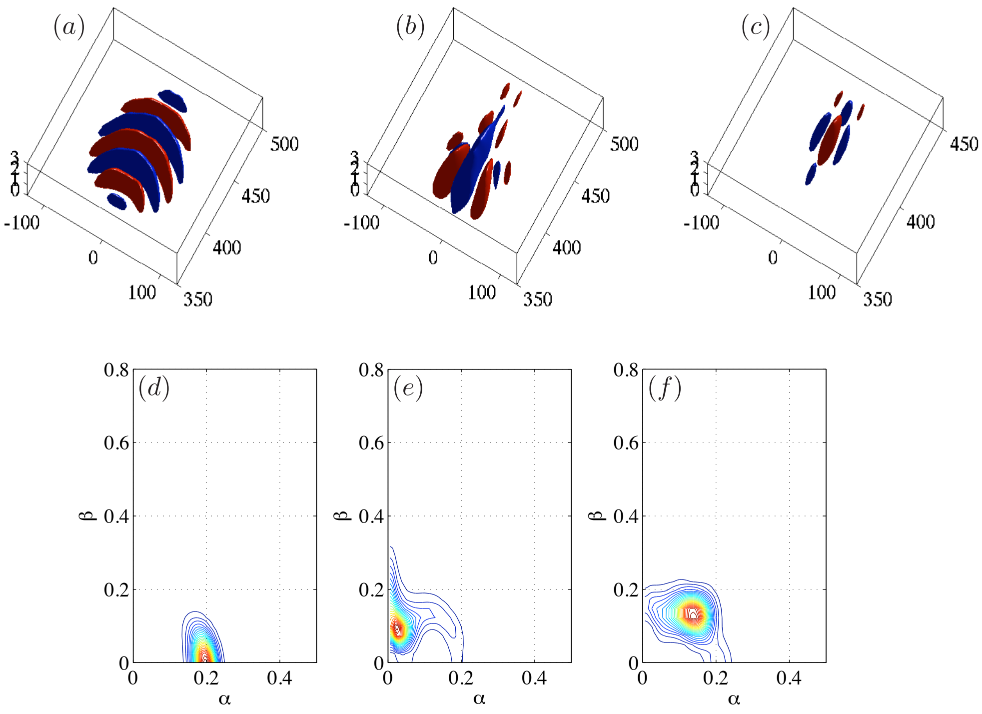

FIGURE 4. Amplitude expansion analysis at $t = 1000$ for the uncontrolled case. The stream-wise velocity is shown for the first (a), the second (b) and third order (c); the corresponding energy spectra are shown in $(d - f9$

$(\Delta Re_x \approx 1.8 \times 10^5)$, respectively. This is in contrast with the results obtained for the linear case, where improvements are observed when l is decreased. Higher actuation amplitude triggers nonlinear effects quickly; thus, the efficiency of the controller deviates from the behaviour of the linear model.

We also vary the amplitude of the initial condition, see table 1. Higher values for the amplitudes introduce stronger non-linearity that leads to worse performance; in particular, we do not observe transition delay for the largest amplitudes (case G), while in case I a reduction of the control effort enhances the performance of the device. In figure 3*b* case F and case I are compared.

Thus, the parametric analysis clearly shows the importance of the nonlinear effects and how they affect the overall performance of the controller. A more detailed analysis of the flow features is introduced in the following section, where the actuation and its influence on the flow are discussed.

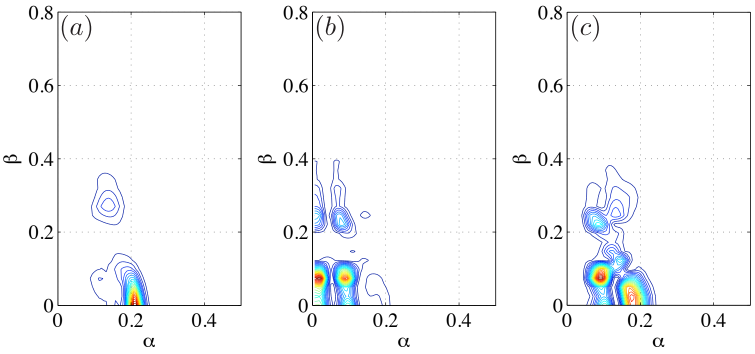

FIGURE 5. Amplitude expansion analysis at $t = 1000$ for the controlled case. The energy spectra for the first order (a), second order (b) and third order (c) are shown.

4. Analysis of the controlled flow

The analysis of the actuation can be performed using an amplitude expansion where the following expansion is applied to the perturbation velocity

$$u(\epsilon) = \sum_{k=1}^{n} u_k \epsilon^k + O\left(\epsilon^{n+1}\right). \tag{3}$$

Here, ϵ represents the initial amplitudes, u_k the perturbation velocity fields, and $n = 3$ for our application. The first order, $n = 1$, corresponds to the linear solution, while $n > 1$ indicates perturbations triggered by nonlinear interactions. The u_k components are computed from velocity fields obtained with several values of ϵ in 3, see Henningson *et al.* (1993) for more details.

First, the uncontrolled flow is considered at $t = 1000$. The linear, the quadratic and the cubic terms of the stream-wise component are shown in figure 4($a - c$) whereas the energy spectra are shown in 4($d - f$) versus the stream-wise wavenumber ($\alpha = \frac{2\pi N_x}{Lx}$) and the span-wise wavenumber ($\beta = \frac{2\pi N_z}{Lz}$). The nonlinear terms, $n = 2$, introduce structures elongated in the stream-wise direction and characterized by $\beta \approx 0.1$. At the third order, the energy peak is obtained from the interaction between the linear term and the quadratic term. It is important to note that the low-order model is based on the linearized Navier–Stokes equations and therefore nonlinear interactions are not included; thus, these modes are those that need to be modeled to increase the performance at higher amplitudes.

A qualitative analysis of the actuation was already introduced in figure 2d, where the flow is shown at $t = 1250$. The amplitude expansion, at $t = 1000$,

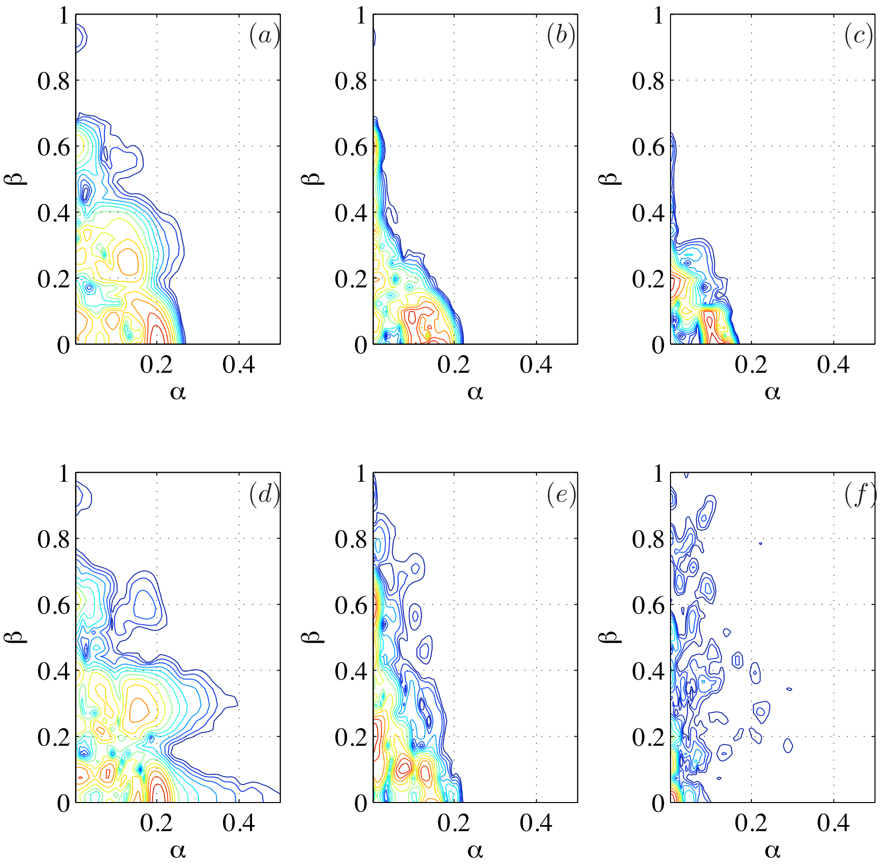

FIGURE 6. Full energy spectra for case F at $t = 1000$ (a), $t = 2000$ (b) and $t = 3000$ (c). Case G is shown for the same instants in the insets ($d - e$). The contour are depicted using the logarithmic scale.

reveals more quantitative data about the flow field. In figure 5a, the spectrum of the first order expansion shows a clear damping of the energy at the frequency related to the TS-waves and the appearance of three-dimensional modes due to the localization of the actuation. The quadratic term is characterized by two peaks at $\beta \approx 0.1$ (see figure 5b); the first is characterized by a lower value of α and is related to the nonlinearities of the uncontrolled flow. The second peak is related to the interaction between the action of the controller and the uncontrolled flow and is found also in the cubic term (see figure 5c). Moreover, in the nonlinear terms $n > 1$, higher-order span-wise modes $\beta > 0.2$ appear.

Thus, the propagation of energy to smaller span-wise scales appears due to the interaction between the controller and the uncontrolled flow; worsening of the performance of the controller for larger amplitudes of the initial disturbance is connected to the excitation of these scales. To investigate this behaviour we compare a satisfactory test-case with one inefficient; in figure 6 the full energy spectra of the controlled case F, $(a-c)$, are compared with the controlled case G, $(d-f)$; logarithmic contours are used to magnify energy-containing scales. At $t = 1000$, the excited frequencies are essentially the same in both cases. However, the evolution for the two cases is different due to the higher energies involved in case G. The amplitudes for the two cases are comparable: in case F, at $t = 1000$, the amplitude is about ≈ 0.002, whereas $a =\approx 0.004$ for case G.

In (b), at $t = 2000$, two peaks appear; one corresponds to the renewed packet of TS-waves, appearing, as already noticed previously, after the actuation. The second peak is localized around $\beta \approx 0.6$; the amplitude is still of the same order, $a = 0.002$. Later, as shown in figure (c), except for a second peak along the span-wise wavenumbers in $\beta = 0.2$, the frequency appears damped. The comparison with the same instant of time for case G, instead, reveals the excitation of the smaller scales triggering the transition to turbulence. In figure 6(e), all the modes active at $t = 1000$ are now characterized by higher energy and higher amplitudes appear; further, small scales are excited along the span-wise wavenumber. Finally, at $t = 3000$, the spectrum reveals clearly the transition to turbulence; the amplitude is $a \approx 0.03$ and results of one order of magnitude larger than the corresponding case in (c).

5. Conclusion

We demonstrated the possibility to delay the transition process using a feedback controller based on localized sensors/actuators. Three dimensional TS wavepacket with realistic amplitudes of the initial perturbation are considered; a reduced order model, capturing the entire input-output behaviour of the flat-plate boundary layer, is built and used for the control design. The controller quenched the disturbances during the early stage of the propagation, when the flow is still laminar; the action of the controller resulted in a significant reduction of the perturbation energy of the disturbance and - later - in a delay of the transition process.

To verify the robustness of the device, a parametric analysis was carried out, considering the controller effort and different finite-amplitudes for the initial conditions. A stronger controller effort resulted in a worsening of the performance: this behaviour of the device is in contrast with the linear prediction; however the delay of the transition was still remarkable. Also, higher amplitudes of the initial condition – generating stronger deviation from the linear behaviour – affected the device, resulting in worst performance.

The analysis of the actuation clearly revealed the excitation of higher order harmonics; the excitation is related to the three-dimensionality of the controller action, combined to the non-linearities of the uncontrolled flow. Starting from this knowledge, a further improvement of the device can be achieved; modern developments in robust control theory may be used to rigorously incorporate uncertainties that may be present in the design process. Moreover, the nonlinear effects can be explicitly accounted during the modeling process.

This work was partially sponsored by the Air Force Office of Scientific Research, through the European Office EOARD, under grant/contract number FA8655-10-M-4006. Computer time provided by SNIC (Swedish National Infrastructure for Computing) and financial support from the Swedish Research Council (VR) are gratefully acknowledged.

References

Bagheri, S., Brandt, L. & Henningson, D. S. 2009*a* Input-output analysis, model reduction and control design of the flat-plate boundary layer. *J. Fluid Mech.* **620**, 263–298.

Bagheri, S., Hœpffner, J., Schmid, P. J. & Henningson, D. S. 2009*b* Input-output analysis and control design applied to a linear model of spatially developing flows. *Appl. Mech. Rev.* **62** (2).

Bewley, T. R. 2001 Flow control: New challenges for a new renaissance. *Progr. Aerospace. Sci.* **37**, 21–58.

Bewley, T. R. & Liu, S. 1998 Optimal and robust control and estimation of linear paths to transition. *J. Fluid Mech.* **365**, 305–349.

Chevalier, M., Schlatter, P., Lundbladh, A. & Henningson, D. S. 2007 A pseudo spectral solver for incompressible boundary layer flows. Trita-Mek 7. KTH Mechanics, Stockholm, Sweden.

Cohen, K., Siegel, S., McLaughlin, T., Gillies, E. & Myatt, J. 2005 Closed-loop approaches to control of a wake flow modeled by the ginzburg-landau equation. *Comp. & Fluids* **34**, 927–949.

Cortelezzi, L., Speyer, J. L., Lee, K. H. & Kim, J. 1998 Robust reduced-order control of turbulent channel flows via distributed sensors and actuators. *IEEE 37th Conf. on Decision and Control* pp. 1906–1911.

Doyle, J. C., Glover, K., Khargonekar, P. P. & Francis, B. A. 1989 State-space solutions to standard H_2 and H_∞ control problems. *IEEE Trans. Automat. Control* **34**, 831–847.

Dullerud, E. G. & Paganini, F. 1999 *A course in robust control theory. A convex approach*. Springer Verlag, New York.

Glover, K. 1984 All optimal Hankel-norm approximations of linear multivariable systems and the l^∞-error bounds. *Int. J. Control* **39**, 1115–1193.

Henningson, D. S., Lundbladh, A. & Johansson, A. V. 1993 A mechanism for bypass transition from localized disturbances in wall-bounded shear flows. *J. Fluid Mech.* **250**, 169–207.

Högberg, M., Bewley, T. R. & Henningson, D. S. 2003 Linear feedback control and estimation of transition in plane channel flow. *J. Fluid Mech.* **481**, 149–175.

Högberg, M. & Henningson, D. S. 2002 Linear optimal control applied to instabilities in spatially developing boundary layers. *J. Fluid Mech.* **470**, 151–179.

Joshi, S. S., Speyer, J. L. & Kim, J. 1997 A systems theory approach to the feedback stabilization of infinitesimal and finite-amplitude disturbances in plane poiseuille flow. *J. Fluid Mech.* **332**, 157–184.

Kim, J. & Bewley, T. R. 2007 A linear systems approach to flow control. *Ann. Rev. Fluid Mech.* **39**, 383–417.

Lauga, E. & Bewley, T. R. 2003 The decay of stabilizability with reynolds number in a linear model of spatially developing flows. *Proc. R. Soc. Lond. A.* **459**, 2077–2095.

Lauga, E. & Bewley, T. R. 2004 Performance of a linear robust control strategy on a nonlinear model of spatially developing flows. *J. Fluid Mech.* **512**, 343–374.

Lewis, F. L. & Syrmos, L. V. 1995 *Optimal Control*. John Wiley & Sons, New York.

Lundell, F. 2007 Reactive control of transition induced by free-stream turbulence: an experimental demonstration. *J. Fluid Mech.* **585**, 41–71.

Monokrousos, A., Åkervik, E., Brandt, L. & Henningson, D. S. 2010 Global optimal disturbances in the blasius boundary-layer flow using time-steppers. *J. Fluid Mech.* **650**, 181–214.

Monokrousos, A., Brandt, L., Schlatter, P. & Henningson, D. S. 2008 DNS and LES of estimation and control of transition in boundary layers subject to free-stream turbulence. *Int. J. Heat Fluid Flow* **29** (3), 841–855.

Moore, B. 1981 Principal component analysis in linear systems: Controllability, observability, and model reduction. *IEEE Trans. Automat. Control* **26** (1), 17–32.

Nordström, J., Nordin, N. & Henningson, D. S. 1999 The fringe region technique and the fourier method used in the direct numerical simulation of spatially evolving viscous flows. *SIAM J. Sci. Comput.* **20** (4), 1365–1393.

Rowley, C. W. 2005 Model reduction for fluids using balanced proper orthogonal decomposition. *Int. J. Bifurc. Chaos* **15** (3), 997–1013.

Schlatter, P., Stolz, S. & Kleiser, L. 2004 LES of transitional flows using the approximate deconvolution model. *Int. J. Heat Fluid Flow* **25** (3), 549–558.

Schlatter, P., Stolz, S. & Kleiser, L. 2006 LES of spatial transition in plane channel flow. *J. Turbulence* **7** (33), 1–24.

Schmid, P. J. & Henningson, D. S. 2001 *Stability and Transition in Shear Flows*. Springer Verlag, New York.

Semeraro, O., Bagheri, S., Brandt, L. & Henningson, D. S. 2010 Feedback control of three-dimensional optimal disturbances using reduced-order models. Under review.

Sturzebecher, D. & Nitsche, W. 2003 Active cancellation of Tollmien–Schlichting waves instabilities on a wing using multi-channel sensor actuator systems. *Int. J. Heat Fluid Flow* **24**, 572–583.

Paper 3

Analysis of time-resolved PIV measurements of a confined co-flowing jet using POD and Koopman modes

By Onofrio Semeraro, Gabriele Bellani & Fredrik Lundell

Linné Flow Centre, KTH Mechanics
SE-100 44 Stockholm, Sweden

Internal Report

Modal analysis by proper orthogonal decomposition (POD) and dynamic mode decomposition (DMD) of experimental data from a fully turbulent flow is presented. The flow case is a turbulent confined jet with co-flow, with Reynolds number based on the jet thickness of Re=10700. Experiments are performed with time-resolved PIV. The jet is created on a square channel with the confinement ratio is 1:5. Statistics of the flow are presented in terms of mean and *r.m.s.* fields. Analysis of spatial spectra and temporal spectra reveal the presence of dominant wavelengths and frequencies embedded in broad-band turbulent spectrum. Frequencies in the shear layer migrate from $St \approx 1$ near the jet inlet to $St < 0.1$ at 18 jet thickness downstream.

This flow case provides an interesting and challenging benchmark for testing POD and DMD and discuss their "efficiency" in a fully turbulent case. At first, issues related to convergence and physical interpretation of the modes are discussed, then the results are analyzed and compared. POD analysis reveals the most energetic spatial structures are related to the flapping of the jet; a low frequency peak ($St = 0.02$) is found when the associated temporal mode is analysed. Higher order modes revealed the presence of faster oscillating shear flow modes combined to a recirculation zone near the inner jet. The flapping of the inner jet is sustained by this region. A good agreement is found between DMD and POD; however, DMD is able to rank the modes by frequencies, isolating structures associated to harmonics of the flow.

1. Introduction

While until the last decade investigations of turbulent flow fields were mainly performed based on a local approach – *e.g.* hot-wire or laser doppler velocimetry (LDV) single point measurements – recent advances in experimental techniques – *e.g.* high-speed stereo and tomographic particle image velocimetry (PIV) – and direct numerical simulations (DNS) have provided access to simultaneously spatially and temporally resolved flow data. This also changed the

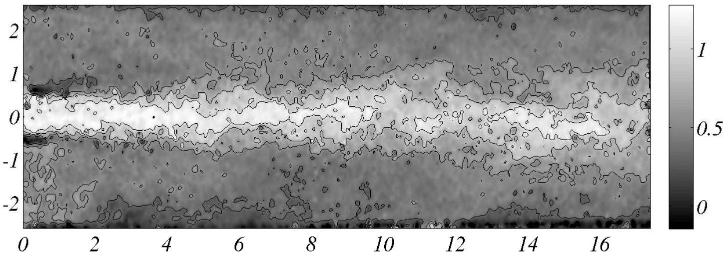

FIGURE 1. Example of PIV snapshots. The contours show the streamwise velocity component.

approach to data analysis. Local analysis of temporal spectra and autocorrelations have been very useful tools to investigate coherent structures (Hussain 1986) from local time series, but with the advent of PIV and similar techniques that introduced spatially resolved data many other methods could be applied. For example one of the classical problem of the analysis of local time series is to convert from temporal to spatial scales. Very often Taylor hypothesis of frozen turbulence is used to go from the former to the latter. Having temporally and spatially resolved data from DNS, Álamo & Jiménez (2009) uses spatio-temporal spectra and correlations to measure directly convection velocities in wall bounded turbulent flows and correct Taylor hypothesis.

However, in order to fully exploit the potential of these techniques, it is becoming increasingly important to develop tools that have "global" view, which can give an insight not only on the topology of the coherent structures but also on the dynamics. This is of great importance for understanding complex natural or industrial flows, such as, for example, atmospheric and environmental flows, combustion chambers, etc. One possible approach to simultaneously make use of the temporal and spatial resolution is to use snapshots of the flow field obtained by time-resolved PIV (see figure 1) or DNS to build a matrix that somehow contains information about the dynamics of the system. Understanding what are the most relevant dynamic structures in a flow is extremely important from a physical point of view to study the instability mechanisms that lead to transition to turbulence or the coherent structures hidden in chaotic turbulent flows, but also, from an engineering point of view, to help building reduced order models that can be used in the design and optimization of complex flow systems (Ilak & Rowley 2008; Bagheri *et al.* 2009).

1.1. *Snapshot-based modal analysis*

Among the snapshot-based methods, one of the most commonly used is the proper orthogonal decomposition (POD) (see, e.g., Holmes *et al.* 1996; Sirovich 1987). POD ranks the modes based on the most energetic structures as solution of the eigenvalue problem related to the cross-correlation matrix computed from the snapshots. The most energetic modes often (but not necessarily) correspond to the most relevant coherent structures of the flow. The temporal information can be recovered using the bi-orthogonal decomposition (BOD), (Aubry 1991). Two sets of modes are computed, related to the two alternative ways of computing the cross-correlation matrix; indeed, the eigenvectors of the temporal-averaged cross-correlation matrix are the spatial modes, while the eigenvectors of the spatial-averaged cross-correlation matrix provide the temporal modes. Following the literature, we refer to the temporal structures as *chrono*-modes (*Chronos*) and to the spatial structures as *topo*-modes (*Topos*).

The spectral analysis of the *chronos* provides the temporal frequencies characterizing the *topos*, whereas the analysis in time domain can reveal the presence of temporal periodicities or limit cycles. However, a first drawback of the technique has to be mentioned here: in general, these structures are associated to more than one frequency; thus, the only possible way to rank POD modes is energy-based. Unfortunately, this criterion is not always a correct measure: low-energy structures associated to instabilities can be relevant (Noack *et al.* 2008). Moreover, this is a statistical method, so the results obtained are intrinsically connected to the conditions in which the snapshots were obtained.

Recently, the dynamic mode decomposition (DMD) has also been applied to the analysis of experimental data and the results have been encouraging (Schmid *et al.* 2010). The DMD algorithm belongs to the category of the Arnoldi methods, widely used for the computation of the eigenvalues and related eigenvectors for linearized flow system, (Ruhe 1984). In Schmid (2010), an improvement of the method is introduced and applied to nonlinear flows, also for experimental cases. From the mathematical point of view, the theoretical background relies on the spectral analysis of the Koopman operator (Mezić 2005); indeed, as shown in Rowley *et al.* (2009), the DMD algorithm approximates the Koopman modes, which can be seen as the averaged harmonic components of the flow, oscillating at certain frequencies given by the eigenvalues of the operator. From the physical point of view, it can be shown that the Koopman modes coincide with the global modes for linearized flows, and with the Fourier modes for periodic flows (see Bagheri 2010).

1.2. *Aim of the paper*

In this paper we focus on the analysis of time-resolved PIV measurements of a turbulent co-flowing jet confined in a square channel. The flow case has been chosen not only because it is relevant for several practical applications (papermaking, combustion engines, etc.) but also for its complexity, since it is a fully turbulent flow that also contains periodic structures as, for example, the flapping of the inner jet due to the interaction with recirculating areas on its side (Maurel *et al.* 1996; Davidson 2001; Goldschmidt & Bradshaw 1973). These periodic structures can be hard to identify with spectral analysis, since they are often "hidden" by the random turbulent fluctuations, however here we try to identify them by the analysis of POD and DMD. Issues concerning the choices of the snapshots and convergence are addressed and the results obtained with two methods are discussed.

1.3. *Structure of the paper*

The paper is organized as follows. In section 2, a brief theoretical overview of the modal analysis is proposed. The experimental setup is briefly described in section 3; details of the measurement technique and the flow quality are provided. Section 4 is devoted to the spectral analysis of the flow; spatial distribution of the dominant frequencies are discussed. The analysis of the coherent structure using POD is proposed in section 5, while the Koopman analysis is carried out in section 6. The paper ends with a summary of the main conclusions (section 7).

2. Theoretical background

The aim of the section is providing a brief theoretical background of the modal decompositions used in this paper. First, proper orthogonal decomposition is introduced. In the second part, Koopman modes analysis is summarized; the focus of the section is mainly on the DMD that provides an approximation of the modes; for a detailed description of the numerical methodology we refer to Schmid (2010), while more theoretical details are provided by Mezić (2005), Rowley *et al.* (2009) and Bagheri (2010).

2.1. *Proper Orthogonal Decomposition*

Proper orthogonal decomposition (POD) is a well known method for extracting coherent structures of a flow from a sequence of flow-field realizations. Given a dataset of flow realizations $\{u(t_1), u(t_2), \dots, u(t_m)\}$ stacked at m discrete times – usually referred as snapshots or *strobes* – POD ranks the most energetic structures of the flow, computed as solution of the eigenvalue problem

$$\int_X R^*\left(x, x'\right) \varphi_k dx' = \lambda_k \varphi_k\left(x\right), \tag{1}$$

where the integral is defined on the spatial domain and

$$R^*\left(x, x'\right) = \int_T u\left(x, t\right) u\left(x', t\right)^T dt \tag{2}$$

is the time-average cross-correlation; the integral is performed in time domain. By definition, the function R^* is positive semidefinite. The eigenfunctions $\mathbf{\Phi} = \{\varphi_1, \varphi_2, \dots, \varphi_m\}$ are orthogonal and real-valued, while each eigenvalue λ_k contains the energy associated to each mode.

The technique was originally proposed as a statistical tool by Loève (1978); in this context, it is usually referred in literature as Karhunen-Loève decomposition (KL). According to the related theorem, a random function can be expanded as a series of deterministic functions with random coefficient. In such a way, the deterministic part – represented by the POD modes – is separated from the random part. Successively, Lumley (1970) applied the method to turbulence analysis; the flow field is expanded using the spatial eigenfunctions obtained from the KL decomposition, where the statistical ensemble employed for the decomposition is represented by a dataset of snapshots.

The temporal information can be recovered projecting back the entire sequence of snapshots on the obtained basis; the projection results in time coefficients series related to the spatial structures. An alternative way to proceed is formalized by Aubry (1991), where bi-orthogonal decomposition (BOD) is introduced. Essentially, a second eigenvalue problem related to the temporal cross-correlation function

$$R^{**}(t,t') = \int_X u(\mathbf{x},t)\, u(\mathbf{x},t')^T d\mathbf{x} \tag{3}$$

is cast. Denoting the eigenvectors obtained from the diagonalization of (3) as $\mathbf{\Psi} = \{\psi_1, \psi_2, \ldots, \psi_m\}$, it can be shown that the following correspondence between spatial and temporal modes holds

$$\psi_k = \lambda_k^{-1} X_t \varphi_k, \tag{4}$$

where $X_t : X \rightarrow T$ is a mapping between the temporal and spatial domain; this decomposition allows to split the space and the time dependence in the form

$$u(x,t) = \sum_{k=1}^{m} \lambda_k \varphi_k(x)^T \psi_k(t) \tag{5}$$

It can be shown that a projection onto the space spanned by m POD modes provides an optimal finite-dimensional representation of the initial data-set of dimension m (Holmes *et al.* 1996).

Hereafter – following the literature – the spatial modes will be referred as *topo*-modes and the temporal modes as *chrono*-modes. The temporal structures give access to the analysis of the frequencies dominating each modes; in general, more then a frequency is identified for each structure.

2.2. *Approximating Koopman modes: dynamic modal decomposition*

As already noticed, although frequencies are captured by the *chrono*-modes, we cannot identify structures related to only one frequency using POD. Moreover, the correlation function provides second-order statistics ranked according to the energy content; in general, low-energy structures can be relevant for a detailed flow analysis. Koopman modes analysis is a promising, novel technique that can tackle these drawbacks. The method was recently proposed by Rowley *et al.* (2009) and is also available for experimental measurements.

In order to describe this technique, we need to introduce the definition of *observable.* An observable is a function that associates a scalar to a flow field; in general, we don't have access to the full flow field in experiments: the velocity - or the other physical quantities are probed at a point, using hot wires, or in a plane, using PIV. However, considering a fully nonlinear flow, the analysis of the observable for a statistically long interval of time is sufficient to reconstruct the phase space and investigate the flow dynamics. By definition, the Koopman operator U is a linear mapping that propagates forward in time the observable $a(\mathbf{u})$

$$Ua(\mathbf{u}) = a(\mathbf{g}(\mathbf{u})) \tag{6}$$

and is associated to the nonlinear operator $\mathbf{g}$. The spectral analysis of the operator provides information on nonlinear flows; in particular, the technique allows to compute averaged harmonic components of the flow, oscillating at certain frequencies given by the eigenvalues of the operator, hereafter indicated with μ. In particular, the phase of the eigenvalue $\arg(\mu)$ determines the oscillating frequency.

The DMD algorithm proposed by Schmid (2010) provides modes that approximate the Koopman modes, as shown by Rowley *et al.* (2009) and Bagheri (2010); the complete demonstration is beyond the scope of this paper, however it is relevant to outline briefly the main steps of the DMD algorithm.

Essentially, the DMD algorithm enters the category of the Arnoldi methods for the computation of the eigenvalues and related eigenvectors of a system. A projection of the system is performed on a basis; the best - and computationally more involved - choice is represented by an orthonormal basis. In the classical Arnoldi method the basis is computed via a Gram-Schmidt orthogonalization (Arnoldi 1951; Saad 1980), that requires a model of the system. A second possibility is given by forming the projection basis simply using a collection of samples or snapshots (Ruhe 1984). This alternative represents the most ill-conditioned among the possible choices, but can be applied in cases when a model of the system is not available.

Given a snapshot at time t_j, the successive snapshot at a later time t_{j+1} is given by

$$\mathbf{u}_{j+1} = \mathbf{A}\mathbf{u}_j \tag{7}$$

The resulting sequence of snapshots $\mathbf{X}_r = [\mathbf{u}_1 \quad \mathbf{A}\mathbf{u}_1 \quad \mathbf{A}\mathbf{u}_2 \quad \ldots \quad \mathbf{A}\mathbf{u}_r]$ will become gradually ill-conditioned; indeed, the last columns of it will align along the dominant direction of the operator $\mathbf{A}$. This observation motivates the possibility of expand the last snapshot r on a basis formed by the previous $r-1$ ones, as

$$\mathbf{u}_{r+1} = c_1\mathbf{u}_1 + c_2\mathbf{u}_2 + \ldots + c_r\mathbf{u}_r + \tilde{\mathbf{u}}_{r+1}. \tag{8}$$

Here, $\tilde{\mathbf{u}}_{r+1}$ indicates the residual error. The aim is to minimize the residual such that $\tilde{\mathbf{u}}_{r+1} \perp \mathbf{X}_r$; a least square problem is cast, such that the elements c_j are given as a solution of it. Introducing the companion matrix

$$\mathbf{M} = \begin{pmatrix} 0 & 0 & \cdots & 0 & c_1 \\ 1 & 0 & \cdots & 0 & c_2 \\ 0 & 1 & \cdots & 0 & c_3 \\ \vdots & & \ddots & & \vdots \\ 0 & 0 & \cdots & 1 & c_r \end{pmatrix} \tag{9}$$

the equation (8) is re-written in matrix-form as

$$\mathbf{A}\mathbf{X}_r = \mathbf{X}_r\mathbf{M} + \tilde{\mathbf{u}}_{r+1}\mathbf{e}_r^T \tag{10}$$

The action of the companion matrix is clear: it propagates one step forward in time the entire sequence of snapshots, whereas the last snapshot is reconstructed using the coefficients c_j. Moreover, the equivalence represented by (8) shows that the operator $\mathbf{A} \in \mathbb{R}^n$ is now substituted by $\mathbf{M} \in \mathbb{R}^r$, with $r \ll n$. It results that the eigenvalues of $\mathbf{M}$ – usually referred as Ritz values – approximate the eigenvalues of the real system. The related eigenvectors are given by $\tilde{\mathbf{\Phi}} = \mathbf{X}_r\mathbf{T}$, where $\mathbf{T}$ are the eigenvectors of the companion matrix $\mathbf{M}$. As observed by Schmid (2010), this algorithm can be used for extract Ritz values and the related vectors from experimental data or sequence of snapshots of nonlinear simulations.

It is a worth mentioning two features of the algorithm, here: first, the modes are characterized by a magnitude that can be easily computed as the norm of the modes $|\tilde{\phi_j}|$. The resulting amplitudes are essential for separating the wheat from the chaff: as shown by Rowley *et al.* (2009), high-amplitude modes are related to the most important - and convergent - eigenvectors. Moreover, (10) allows to estimate the norm of the residual error as $\|\tilde{\mathbf{u}}\| = \|\mathbf{A}\mathbf{X}_r - \mathbf{X}_r\mathbf{M}\|$. The analysis of the residuals is helpful for the identification of the snapshots dataset; indeed, the selection of the Δt_s of sampling and of the proper time windows of investigation are related to the residual analysis.

The linear dependency of the dataset, necessary for identifying the last snapshot, makes this method prone to convergence issues and ill-conditioness. An improvement is proposed by Schmid (2010), where a self-similar transformation of the companion matrix $\mathbf{M}$ is obtained as results of the projection of the dataset on the subspace spanned by the POD generated from it. To this aim, a preliminary singular value decomposition (SVD) of $\mathbf{X}_r$ is performed; the SVD allows to disregard the redundant states and the transformed companion matrix is now a $full$ matrix: both these features make the eigenvalues problem better conditioned.

3. Experimental setup

The experiments are performed in a square channel whose dimension D is of 50 mm. The first 300 mm of this square channel are divided into three sections of dimensions 19, 10 and 19 mm by means of two horizontal walls that span the entire width, see figure 2*c*. The end of the splitter walls corresponds to the beginning of a planar co-flowing jet, which is our measurement domain, see figure 2*a*. The thickness d of the inner jet is of 10 mm, which gives a confinement ratio d/D of 1:5. The flow in the three jets is supplied by two independent pumps through two radial distributors, one connected to the inner and one to the two outer channels, see figure 2*d*. This configuration allows to control the flow rates of the inner and the outer sections independently, therefore two non-dimensional parameters can be varied in the present setup: the velocity

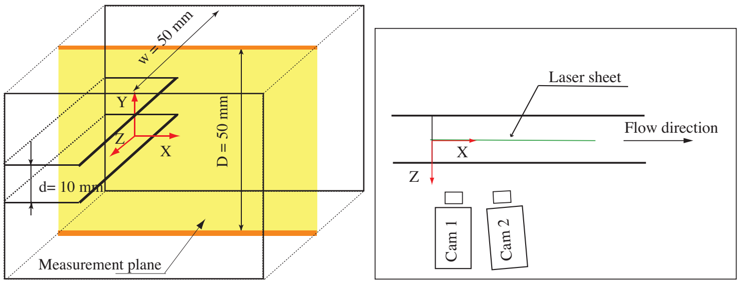

(a) Geometry and coordinate system (b) Light sheet and cameras arrangement

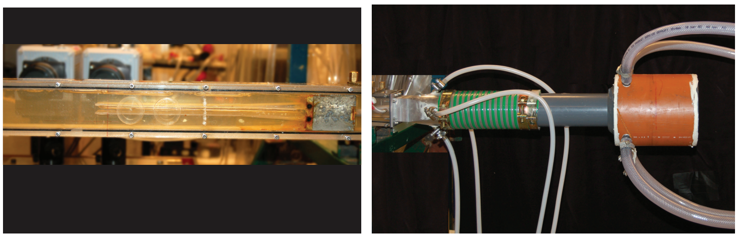

(c) Test section (d) Flow distributor

Figure 2. Experimental setup.

ratio $\lambda_r = U_j/U_s$, where U_j and U_s are the centerline velocities of the inner and the outer jets respectively, and the Reynolds number $\mathrm{Re} = U_j d/\nu$, where d is the inner duct thickness and ν is the kinematic viscosity of the fluid.
In this work we show results for $\lambda_r = 2.1$ and $Re = 10700$.

3.1. *Measurement technique*

The time-resolved measurements of the flow were done by high-speed Particle Image Velocimetry (PIV). The PIV system used in this work consists of a double cavity 10mJ Nd:YLF laser (repetition rate 2-20000 Hz) as a light source, and two high-speed cameras (up to 3000 fps at full resolution) with resolution of 1024x1024 pixels.
The arrangement of the cameras and the laser-sheet is shown in figure 2*b*. The two cameras were used to acquire two 2-D velocity fields, each of them of 50x100 mm^2. The second camera was tilted by 5° in order to reach an overlap between the two fields of about 20 mm, so that the total measurement area is of about 180 mm.
The two cameras were calibrated by taking images of a calibration plate with known reference points *in situ*, and the calibration parameters were extracted using a pinhole-based model (see Willert 2006).
The flow was seeded with 10μm silver-coated tracer particles, and a series of double-frame, single-exposure images were acquired at a rate of 1500Hz

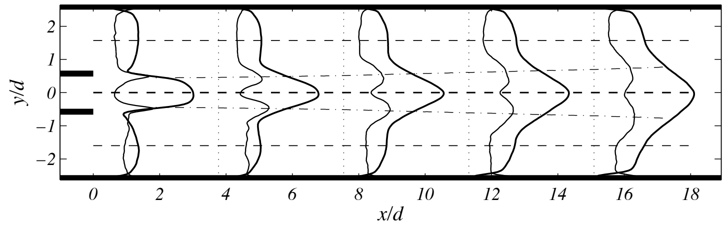

FIGURE 3. Streamwise evolution of the mean (thick line) and *r.m.s.* (thin line) profiles of U are at the channel centerline (z/d=0). The profiles are scaled to fit the figure.

for a total time of 4 seconds. The velocity fields were calculated using the commercial PIV software *DaVis 7.2* from *LaVision GmbH.* The algorithm used is a multi-pass correlation with continuous windows deformation and shift, which allowed to achieve a final interrogation window size of 8x8 pixels. The size of the interrogation window is of about 0.75x0.75 mm^2 in physical space, which sets the lower limit for the spatial resolution. The window overlap was 50%. For detailed information about the performance of the PIV algorithm, see Stanislas *et al.* (2008).

3.2. *Flow quality*

In order to establish the characteristics of the flow in the channel, we measured cross-stream profiles at 5 spanwise stations including the channel centerline, and spanwise profiles at the centerline of the three jets. In this paper we refer to the direction parallel to the x-coordinate as the streamwise direction, the direction parallel to y as the cross-stream and the one parallel to z as the spanwise direction. The streamwise and cross-stream velocity components are U and V, respectively.

Figure 3 shows the streamwise development of the time average of U ($\langle U\rangle$) and the root mean square ($r.m.s$) of the streamwise turbulent fluctuations u' ($\langle u'^2\rangle$) at the channel centerline ($z = 0$). The profiles are scaled to fit the figure, and the x and y coordinates are normalized by the inner jet thickness d. Two main features can be observed in the mean velocity profiles: the boundary layers developing at the channel walls and the two wakes generated by the blunt end of the splitter walls on the profiles near the inlet. The *r.m.s.* profiles show the characteristic local maxima at the two shear layers. The dashed lines show the centerlines of the three jet regions. The dashed-dotted lines follow the development of the jet half width L, defined as the point where $(U - U_s)/(U_j - U_s) = 0.5$.

The spanwise evolution of the velocity profiles have also been investigated to asses to what extent the flow can be considered two-dimensional. Figures 4(a) and (b) show the cross-stream profiles of $\langle U\rangle$ at 5 spanwise stations

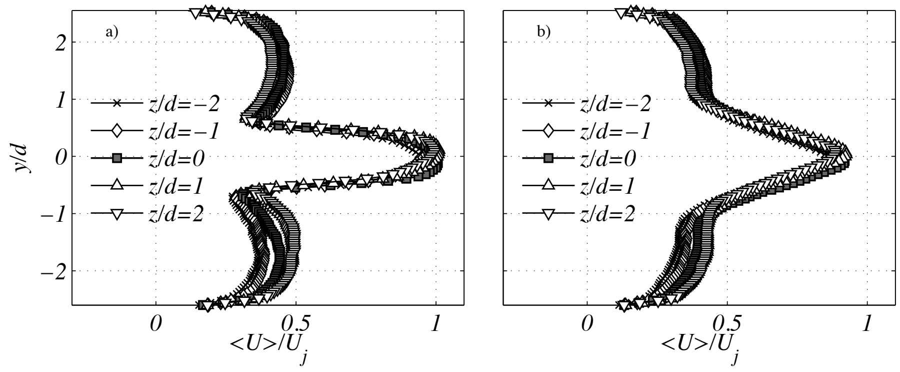

FIGURE 4. Cross-stream profiles at $x/d = 0$ (a) and $x/d = 7.5$ (b)

$(Z/d = -2, -1, 0, 1, 2)$, whereas figures 5(a) and (b) show the spanwise profiles. The latter has been measured by rotating the channel 90° around the x-axis, so that the light sheet was parallel to the z-axis.

These figures show that although the inlet profiles are not perfectly *top-hat*, the flow rates on upper and lower channel are quite the same and the boundary layer at the side walls never reaches the center of the channel. Therefore we can consider the flow as *quasi*-2D.

Normalized mean, *r.m.s.* and Reynolds stress profiles profiles are shown in figure 6. The normalizing scales are the local velocity excess $U_0 = U_j - U_s$ for the mean velocity, and the jet half width L for the y coordinate. From figure 6(a) we can see that the mean velocity profiles are still affected by the wake behind the walls splitter but self similarity is reached already at $x/d = 5$, see figure 6(b). From these figures we can also see the growth of the boundary layers from the channel walls, which however do not reach the self-similar region at the core of the jet. Figures 6(f) and 6(d) show that *r.m.s* and Reynolds stresses reach self similarity later than the mean flow, at around $x/d = 10$, as reported by Chua & Lua (1998) in a similar flow case. It is interesting to note that the typical saddle shape of the *r.m.s* profiles is not symmetric and seem to be inclined so that the *r.m.s* values on the lower part of the channel are higher than in the upper part. This might be an indication of a recirculation zone induced by the confinement due to a slight asymmetry of the experimental setup. Recirculation zones around a jet due to confinement has been observed by (Maurel *et al.* 1996; Davidson 2001; Goldschmidt & Bradshaw 1973). In these works it has been shown that the re-circulation zone can induce self-sustained oscillation of the jet. The frequency of the oscillations are dependent on the geometry and the confinement ratio but in general they have low frequency and are characterized by Strouhal numbers based on the jet thickness of $St \approx 0.01$.

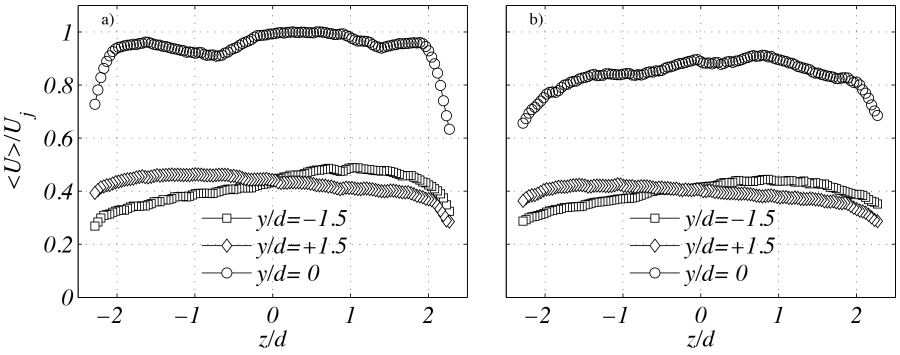

Figure 5. Spanwise profiles at $x/d = 0$ (a) and $x/d = 7.5$ (b)

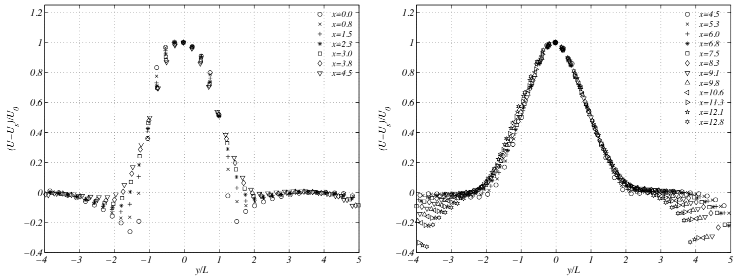

(a) $x/d < 5$ (b) $x/d > 5$

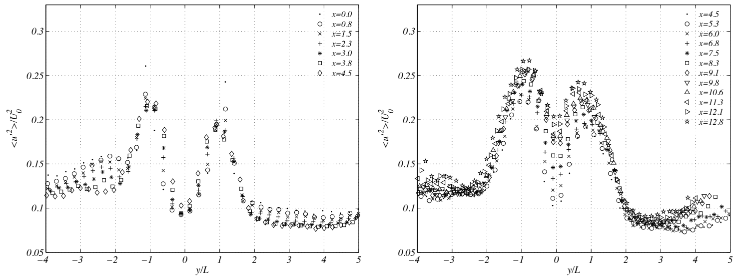

(c) $x/d < 5$ (d) $x/d > 5$

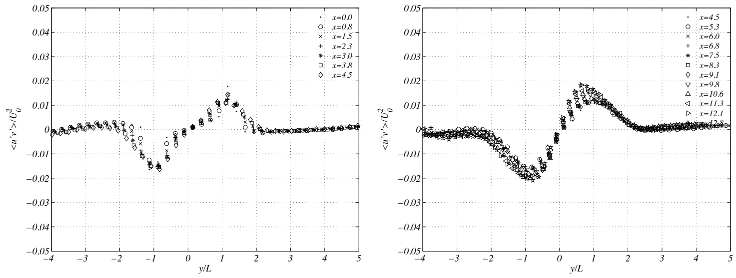

(e) $x/d < 5$ (f) $x/d > 5$

FIGURE 6. Self similar profiles of Mean Streamwise velocity, Normal and shear stresses $\langle u' \rangle$ and $\langle u'v' \rangle$.

4. Spectral analysis

4.1. *Computational procedure*

Time resolved PIV measurements were done at the symmetry plane of the channel. As an output of the PIV measurements, for each point of the measurement domain ($0 < x/d < 18$) we obtained a time signal made of 6000 samples for a total sampling time of 4 seconds. We therefore have spatially and temporally resolved data from which we can detect the presence of dominant wavelength and frequencies by the analysis of the Power Spectral Density (PSD). Temporal spectra are calculated using the Welch method seeking a compromise between smoothness and good resolution low frequencies. For the spatial spectra we followed a similar approach, but in this case the maximum length of the signal was determined by the physical length of the measurement domain, and the final PSD estimate was obtained by averaging the spectra at different time steps.

Examples of temporal and spatial spectra (Φ_u and Θ_u, respectively) can be seen in figure 7. Figure 7(a) shows the normalized PSD of the streamwise velocity fluctuations at 5 streamwise stations ($x/d = 0, 1.5, 7, 10, 15$) along the jet centerline. It can be seen that the slope of the spectra approaches the value of -5/3 as we move downstream, where we expect to have nearly isotropic turbulence in the jet core. Peaks might also be present in some regions of the spectra but it is hard to distinguish it from the noise, since the time series relatively short due to the limited capabilities of PIV to acquire long time series do not allow us further smoothing.

Therefore, in order to get an idea of the dominant scales in the different regions of the flow we can plot the contours of the spectra as a function of y as shown in figure 8. The normalized spectra here are presented on a logarithmic scale, thus they and premultiplied by the frequency or wavelength vector. Figure 7(a) shows the temporal spectra computed at the jet outlet, whereas figure 7(b) shows the distribution of spatial spectra. In the latter, it can be seen that much of the energy is contained in the two regions corresponding to the shear layer, with a maximum peak located at $d/\lambda_x \approx 0.3 - 0.4$, which corresponds to about half of the channel width $D/2$ in physical terms. In the same region we can observe two peaks in the temporal spectra at $St = 1$, where St indicates the Strouhal number and is defined as $St = \frac{f(d/2)}{U_j - U_s}$, with f being the dimensional frequencies. In the rest of the domain instead, most of the energy is contained at low St, in particular in the co-flow region peaks appear at $St < 0.1$. This is another evidence of low-frequency structures, like a re-circulation zone due to the jet confinement, even if the St is higher than the one reported in previous studies. This can be explained by the fact that the limited length of the time series and the windowing used to compute the spectra, the resolution of the low frequencies is poor.

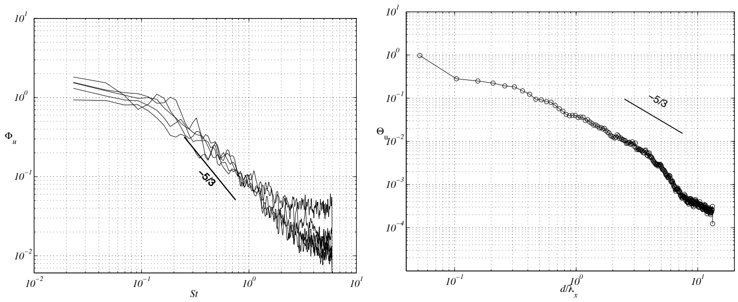

(a) $y = 0$ (b) $y = 0$

FIGURE 7. Φ_u and Θ_u at $y = 0$

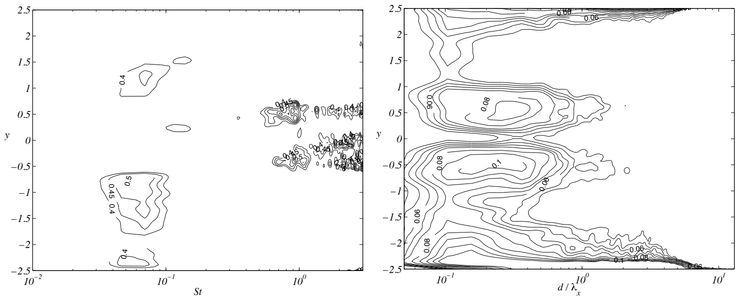

(a) $x/d = 0$ (b) $x/d = 0$

FIGURE 8. Φ_u and Θ_u at $x/d = 0$

4.2. *Spatial distribution of dominant frequencies*

The spectra shown in figure 7(*a*) are computed at the jet outlet. However it is interesting to analyze what happens further downstream. This is shown in figure 9, where the y distribution of Φ_u is show at 8 streamwise stations: $x/d = 0.38, 0.75, 1.13, 1.50, 3.40, 7.16, 10.90$ and 15.80. What it can be observed from this sequence is that the two high-frequency peaks in the shear layer tend to "migrate" towards lower frequencies as we move downstream, to approach the value of $St = 0.1$ for $x/d > 10$, *i.e.* in the self-similar region. This can be explained by the fact that in the region $x/d < 5$ we still have small scale/high-frequency structures due to the wake behind the splitter walls, which can influence the dynamics of the shear layer, as reported in Örlu *et al.* (2008). However, further downstream the most dominant structures are large/low frequency due to the flapping of the inner jet (Maurel *et al.* 1996; Davidson 2001; Goldschmidt & Bradshaw 1973).

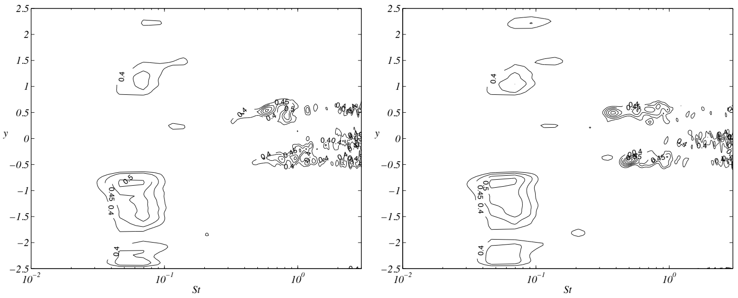

(a) $x/d = 0.38$ (b) $x/d = 0.75$

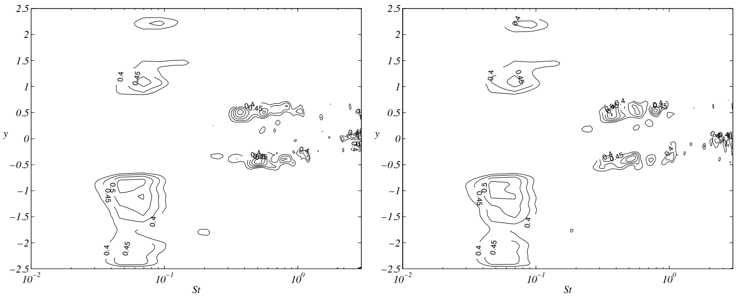

(c) $x/d = 1.13$ (d) $x/d = 1.50$

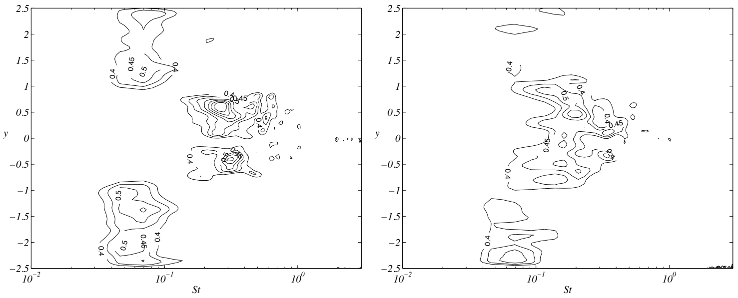

(e) $x/d = 3.40$ (f) $x/d = 7.16$

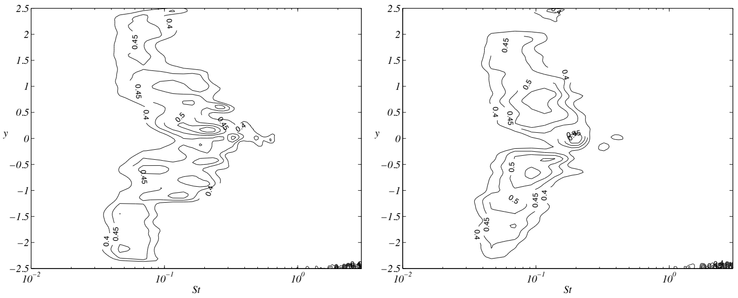

(g) $x/d = 10.9$ (h) $x/d = 15.8$

FIGURE 9. Contours of premultiplied spectra $St\Phi_u$. The contour lines are drawn at: 0.4, 0.45, 0.50, 0.55, 0.60, 0.65, 0.70.

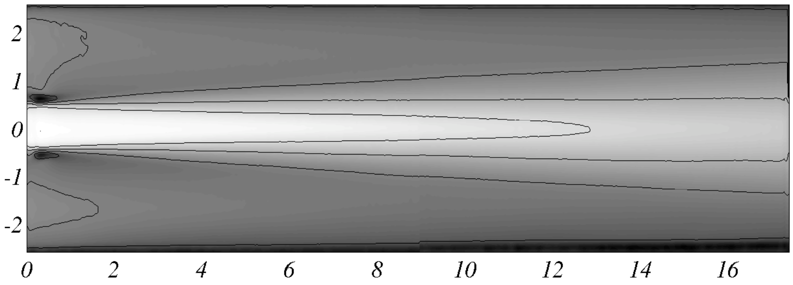

FIGURE 10. U-component of the first *topo*-modes (mean-flow).

5. Analysis of coherent structures I: POD

5.1. *Choice of the snapshots*

The mapping X_t provides a relation between the space and time domains; thus, the diagonalization of the (3) provides temporal modes, while the spatial modes can be evaluated using (4). A discrete form of this procedure was introduced by Sirovich (1987). Here the author shows that the corresponding discrete form of the operator X_t can be built by stacking N_t snapshots of the flow field to form a matrix of dimensions $n \times N_t$, where n is the number of grid points in space and N_t is the number of snapshots. Therefore this method is known as *snapshot method.* The advantages of the techniques relies on the dimensions of the eigenvalue problems associated with the two alternative cross-correlations; indeed, the number of snapshots stacked in time is usually smaller than the number of spatial degrees of freedom; thus, the eigenvalue problem associated to the spatial cross-correlation matrix is more expensive than diagonalizing the temporal cross-correlation; however, the relation (4) provides a mean for recovering the spatial modes from the temporal modes using the mapping X_t. Note that the same results can be achieved performing a singular value decomposition (SVD); in this case, the temporal structures and the spatial structures are obtained simultaneously, see Schmid (2010). The two procedures are equivalent, and the former method was used in our calculations.

When choosing the snapshots, there are two important choices to be made: the total number of snapshots N_t and the time interval between two consecutive snapshots Δt_s. In fact, as already mentioned, the modes obtained by POD are always the optimal (in a least square sense) representation of the snapshots used to compute the cross-correlation matrix, but it has to be kept in mind that this modes are representative of the flow just as much as the cross-correlation matrix is. Therefore if we want to extract physically relevant information of the flow structures, N_t has to be chosen so that there are a sufficient number of independent samples to ensure a converged statistics, and that the time spanned by the snapshots is long enough to contain the slowest scales of the flow. Provided the above conditions, the *topos*-mode (*i.e.* the spatial modes)

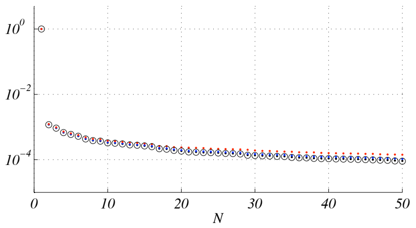

(a) Distribution of λ_k

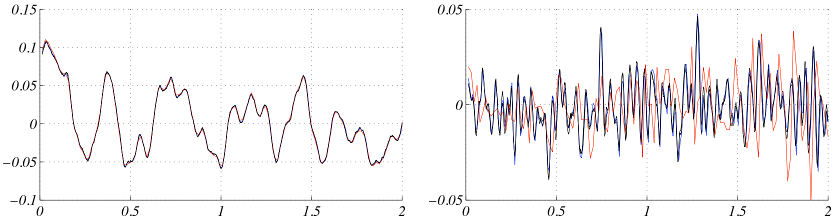

(b) *Chrono*-mode n=1 (c) *Chrono*-mode n=29

FIGURE 11. Eigenvalues and temporal modes for $\Delta_t = 1/750$ (black), 1/250 (blue) and 1/125 (red).

do not seem to depend at all on the time of sampling Δt_s. However, when recovering the temporal information by (4), it is clear that this parameter determines the temporal resolution of the *chronos*-modes; thus, if Δt_s is too large, the *chronos*-modes associated with high frequencies do not converge. An example of this is idea is shown in figures 9.11(b) and 9.11(c), where we see the *chronos*-modes corresponding to mode number 1 and 29 respectively. It can be seen that the time series of mode 1, which shows mainly low-frequency quasi-periodic fluctuations is well captured for every Δt_s, whereas for mode 29 the time series obtained with the largest Δt_s does not follow the ones obtained with smaller time interval between the snapshots. Differences appears also in the eigenvalues, see figure 9.11(a). The spectra obtained with Δt_s=1/750 and 1/250 are basically the same, whereas the spectrum computed with the largest interval diverges as the number of modes, N, increases.

5.2. *Spatial and temporal modes*

From the first convergence analysis of the previous section we conclude that a Δt_s of 1/250 is adequate to temporally resolve the structures of our flow case.An acquisition time of 3.3sec is chosen, corresponding to $N_t = 834$ is fixed which is on the order of about three times the slowest time scale of the flow. As a convergence test, we take three sets of 5000 snapshots which differ from a time offset of $\approx$ 0.2sec from each other. The convergence is directly analyzed by comparing the POD eigenvalues obtained from each set. A relative error of order $O(10^{-4})$ is obtained among the set; this value is deemed sufficient to

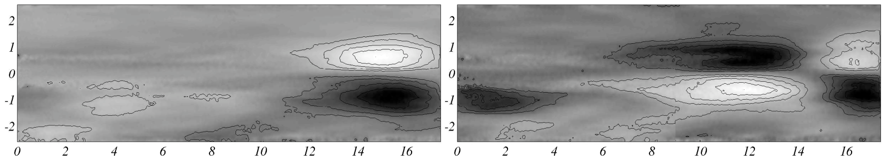

(a) First *topo*-mode

(b) Second *topo*-mode

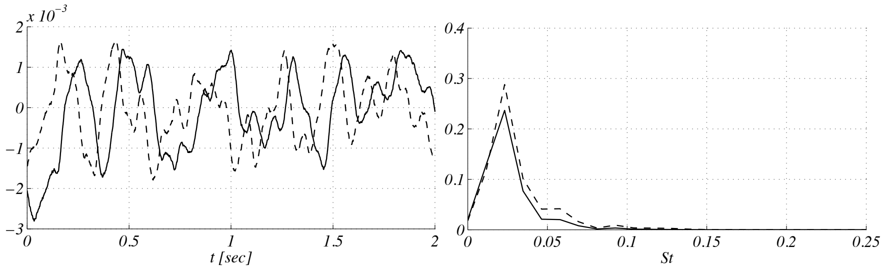

(c) *Chrono*-modes: time domain

(d) *Chrono*-modes: frequency domain

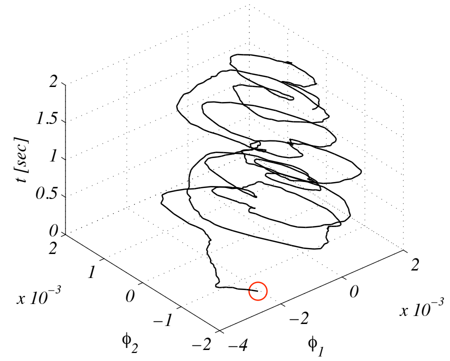

(e) Temporal orbit in the subspace spanned by φ_1 and φ_2

FIGURE 12. The first and second POD modes are analysed. The streamwise component of the *topo*-modes is shown. The first *chrono*-mode is indicated with a solid line, the second one with a dashed line.

guarantee convergence of the results. A further numerical test is related to the orthogonality of the modes. The condition is satisfied down to $O\left(10^{-13}\right)$ for all the modes.

In figure 9.11(a), the eigenvalues related to the POD modes are shown; the portrait obtained is rather typical: the first mode contains 97% and is related to the meanflow of the jet, figure 9.11(a). Hereafter, we will denote it as 0-mode. As expected, the corresponding *chrono*-mode is constant.

The remaining modes are related to the fluctuating part of the flow field, and the sum of their eigenvalues represents the turbulent kinetic energy (TKE). A first eye-inspection of the *topo*-modes reveals that some of the modes come in pairs. This is evident for example for mode 1 and 2, as shown in figures 12$(a-b)$. Here we can see that the structure of the two modes is the same, except for a shift in phase: they are both anti-symmetric with respect to the x-axis, and they both present two large lobes located downstream. The analysis of the corresponding *chrono*-modes confirms the similarities between the two structures: they both show periodicity with similar amplitude of the peaks. This is an evidence that the modes represent a wave-like periodic structure of the flow. In fact, since the POD modes are real, two modes are needed to describe a flow structure traveling as a wave (see e.g Rempfer & Fasel 1994). From a physical point of view this structure represent the flapping of the jet, which is the most energetic feature of the flow. A frequency analysis of the signal from the *chrono*-modes (see figure 12d) shows that there is a very clear peak at $St = 0.02$ for both mode 1 and 2. This is in line with the previous frequency measurements of flapping of confined turbulent jets mentioned in the earlier sections. It is remarkable that, although in general each POD mode can be associated with more than one frequency, the peak at $St = 0.02$ appears more clearly than in the spectral analysis of the time series. This is because the time series contains information about all the turbulent structures, whereas the considered modes isolate only one feature.

Finally, figure 12(e) shows the temporal orbit obtained by projecting the flow field onto the subspace spanned by φ_1 and φ_2. It is clear that the trajectory shows an attractor-like behavior, similar to what we would observe from the vortex shedding behind a cylinder. This confirms the impression that the modes represent a physical coherent structure and are important for the reconstruction of the dynamics of the flow system.

In figure 13$(a-c)$, the modes 3-5 are shown. These modes are characterized by smaller scales and higher frequencies (see figures 13d and 13e) than the previous ones, but they are also clearly associated with oscillations of the shear layer. One interesting feature emerging from these modes there is a structure in the lower part of the channel that seems to be associated with a recirculation zone. This recirculation might be responsible for the jet self-sustained oscillations, which is confirmed by the fact that this feature is coupled in the POD mode corresponding to shear layer oscillations. The analysis of the related *chrono*-modes in spectral space (figure 13e) reveals the presence of three well defined frequencies in all these modes; however, the peaks have different magnitudes in the three modes.

Note that the frequency increases as the energy associated to the modes decreases. This might be a consequence of the fact that lower energy is associated to smaller scales; indeed, an eye-inspection of the modes shows that, as the rank increases, the *topo*-modes is characterized by low-energy structures,

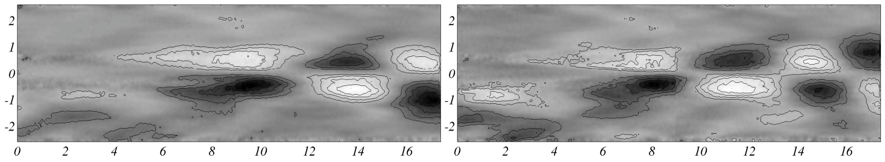

(a) Third *topo*-mode (b) Fourth *topo*-mode

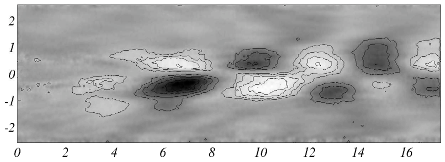

(c) Fifth *topo*-mode

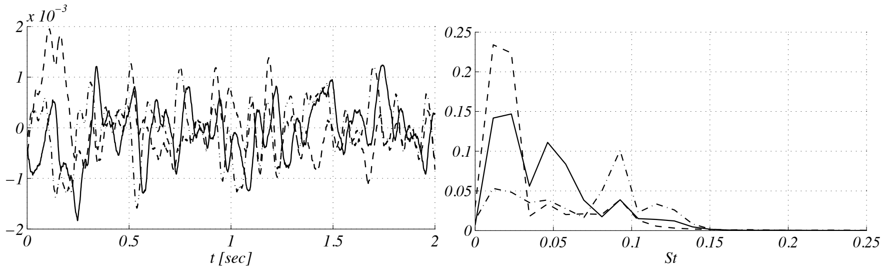

(d) *Chrono*-modes: time domain (e) *Chrono*-modes: frequency domain

FIGURE 13. The third, fourth and fifth POD modes are shown. The streamwise component of the *topo*-modes is shown. The first *chrono*-mode is indicated with a solid line, the second one with a dashed line and the third with a dashed-dotted line.

progressively smaller, while the corresponding *chrono*-modes are dominated by higher frequencies. This trend is confirmed by figure 14, where the normalized spectrum for each of the first $N = 100$ modes is depicted. In addition, it can be noticed that strong peaks occur for high-energy modes; moreover the number of peaks increase with the order of the modes; thus, modes containing high-energy, are also characterized by few and well distinguished frequencies (*i.e.* they are associated with periodic coherent structures).

6. Analysis of coherent structures II: Koopman modes

6.1. *Convergence tests and selection of the modes*

As mentioned in section 2.2, the linear dependency of the snapshots dataset allows to write (10); however, this feature makes the method prone to ill-conditioness. Thus, to ensure the effectiveness of the numerical procedure, we

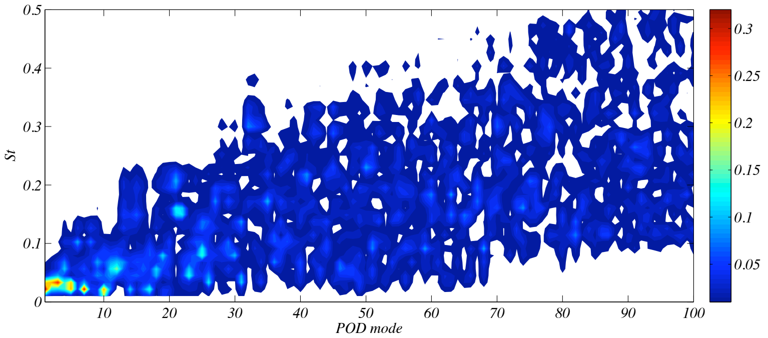

FIGURE 14. Spectral analysis of the first $N_m = 100$ *chrono*-modes.

carry out $ad - hoc$ tests. In particular, the choice of an adequate sample of snapshots turns out to be crucial; following the guidelines already discussed for the POD, we select as parameters for the choice, the number of snapshots N_t and the sampling time Δt_s, *i.e.* the distance between two successive snapshots. To this aim, we make use of the residuals $\tilde{\mathbf{u}}$ (see section 2.2), analysing their trend when changing N_t or Δt_s: the main idea is to select the set of parameters that guarantees the smaller residual.

Figure 15(a) reports the behaviour of the residual as function of time. Two different sampling-strides are considered: the dashed line indicates a stride $N_s = 20$, while for the continuous line $N_s = 10$. The overall trend shows a reduction of the residual value as the number of samples increases. In figure 15(b), the residual value is analysed as function of the number of snapshots spanning the sampling interval Δt_s for two datasets: the original PIV measurements (dashed lines) and a filtered set of snapshots (solid lines). The cut-off frequency of the filter is of 250Hz, which reduces the measurement noise but leaves unaltered all the relevant scales of the flow. The third parameter considered in the graph is the time-window of observation: the lines are darkened progressively according to the chosen final time of the time-window, from $t = 0.667$ to $t = 4.0$. We can summarize as follows the main results included in figure 15(b):

1. In all the case, a monotonic reduction of the value is obtained when reducing Δt_s.
2. Longer windows of observation guarantee better results.
3. Fixing the sampling parameters and using the filtered data, an improvement of about 20% is observed for the residual values.

However, we need to keep in mind also the physical point of view; clearly, longer sampling interval act as a filter; thus, high-frequency modes cannot be resolved if a too large Δt_s is chosen. The filtering of the dataset theoretically imposes the lower limit $\Delta t_S = 1/250$; however, the SVD pre-processing of the

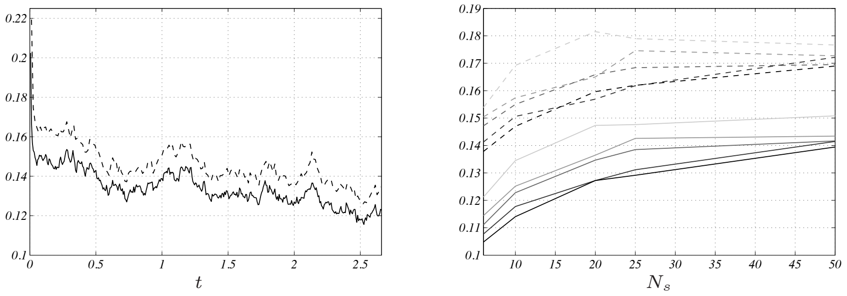

(a) Residuals vs time

(b) Residuals vs sampling-stride

FIGURE 15. Residual analysis - in (*a*) the dashed line indicates the residuals associated to the original data, while the solid line indicates the filtered data (250Hz). In (*b*) the same legend is adopted; darker lines are related to longer time windows of sampling.

dataset allows to circumvent the problem, disregarding the states numerically not relevant, usually related to linear dependencies. In more detail, denoting with σ the singular values computed for the shapshots dataset, the ratio σ_j/σ_1 provide an estimation of the condition number. A threshold can be selected: as a rule of thumb, one can consider the numerical precision – if DNS data are used – or the precision given by the experimental instrumentation. The states associated to the singular values that are below this threshold can be disregarded.

The amplitudes associated to the Koopman modes serve efficiently as parameter for the selection of the modes. Here a further convergence criterion is introduced due to the complexity of the analysed flow. In particular, three sets of snapshots are formed: each of them is characterized by $N_t = 700$ and a snapshots stride of $\Delta N_t = 8$: the resulting interval in time for each case is $\Delta t = 3.3$sec; the sets differ in the selected time-window, which slides forward with a small Δt. Since the investigation involves a flow fully developed after the transient, we expect that the most important features appear in all the considered sets: thus, our procedure relies on the comparison of the modes obtained applying the DMD to the three sets. We consider convergent the eigenvalues that for each set had a difference in frequency below a chosen tolerance. Moreover, the corresponding eigenvectors are compared via a cross-correlation, in order to ensure the physical correspondence among the modes picked in each set.

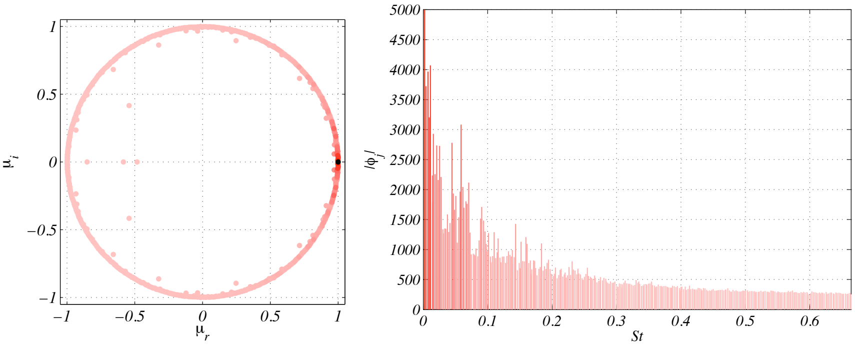

(a) Discrete spectrum (μ)

(b) Amplitudes associated to St

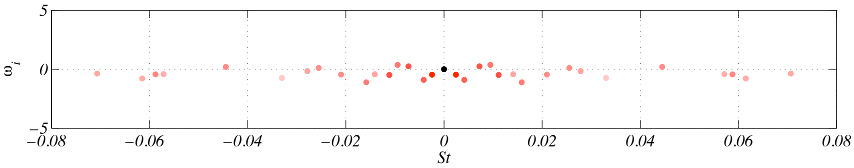

(c) Continous spectrum (ω) after the selection. The real frequency is reported as St.

FIGURE 16. The spectrum obtained from the DMD is shown in (a). In (b) the amplitudes associated to each eigenvalue are shown (except the first mode). The physical relevant ones are kept in (c).

6.2. *Spatial modes by DMD*

In figures 16(a), the discrete spectrum obtained for the first set – spanning the time interval $t = [0, 3.3sec]$ – is shown. As observed in Mezić (2005) and Bagheri (2010), for $t \to \infty$, the Koopman operator is unitary, thus all the eigenvalue will lie exactly on the unit circle. Indeed, we can observe that nearly all the eigenvalues lie close to the unit circle. The amplitudes related to each modes are depicted in 16(b) with the same colour; the darker is the colour, the higher is the amplitude of the mode. The peaks are still quite numerous and - although are quite well resolved - the result demonstrates the necessity of introducing the convergence method for the selection of the modes physically meaningful.

After the selection is performed, only a part of the eigenvalues is kept, as shown in figure 16(c) where the corresponding Strouhal number is reported for each of them; in the latter figure, the spectrum is in continuous form, obtained using the relation $\omega = \log \mu/(\Delta t_s)$. In particular, the selected modes approach the 0 growth limit; indeed, in a nonlinear flow we cannot expect growing/decaying structures. The presence of a growth rate is mainly related to the time-window of observation; in principle, due to the property of the Koopman operator referred above, infinite time of observation would lead to

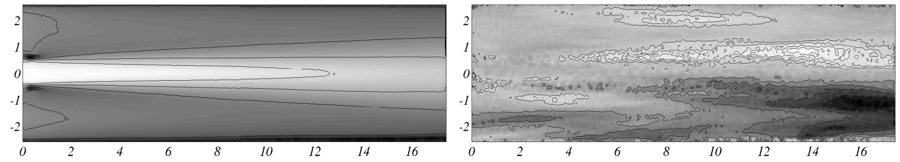

(a) Mean flow (b) $St < 0.01$

FIGURE 17. The streamwise component of the meanflow is shown in (*a*). In (*b*) the low frequency mode associated with the highest amplitude is shown.

eigenvalues characterized by null growth. The distance from the $\omega_i = 0$ can be also regarded as a convergence test: the more the eigenvalues are close, the more are convergent the modes, *i.e.* physically relevant.

The black dot indicates the mean-flow, appearing as the 0 frequency mode in the continuous spectrum and shown in figure 17(*a*). The first mode is characterized by a low Sthroual number (figure 17*b*); the structures is anti-symmetrical with the respect of the streamwise direction and mostly located downstream, where two elongated lobes dominate the structures. This mode – and the ones characterized by low frequency – closely resembles the POD modes shown in figure 12; indeed, from a physical point of view, these structure are related to the flapping of the jet, as confirmed by the St in line with the previous frequency measurements.

The DMD/Koopman mode analysis turns out particular fruitful for the analysis of the recirculation close to the jet-inlet. In figure 18*a*, the mode related to this feature is shown; an elongated lobe is observed in the lower, upstream region of the domain where the previous analysis showed the presence of recirculation. The corresponding St number is in agreement with the former measurements. Note that this region was highlighted also by POD analysis; however, the modes (figure 13) were characterized by the simultaneous presence of the shear flow and the recirculation phenomena, as confirmed by the analysis of the *chrono*-modes (figure 13$d-e$). Using the Koopman modes, is now possible to clearly distinguish the physical phenomena related to the frequency peaks (figure 13*e*). In particular, figures 18($b-d$) show the shear-flow structures associated to the Strouhal number obtained by the spectral analysis (13*e*). The modes are anti-symmetric; the finer structures located downstream in the domain are associated to higher frequencies and closely resemble the structure already observed with the POD analysis.

7. Conclusions

POD and DMD have been applied to experimental data from PIV measurements of a turbulent confined jet with co-flow. The jet is fully turbulent,

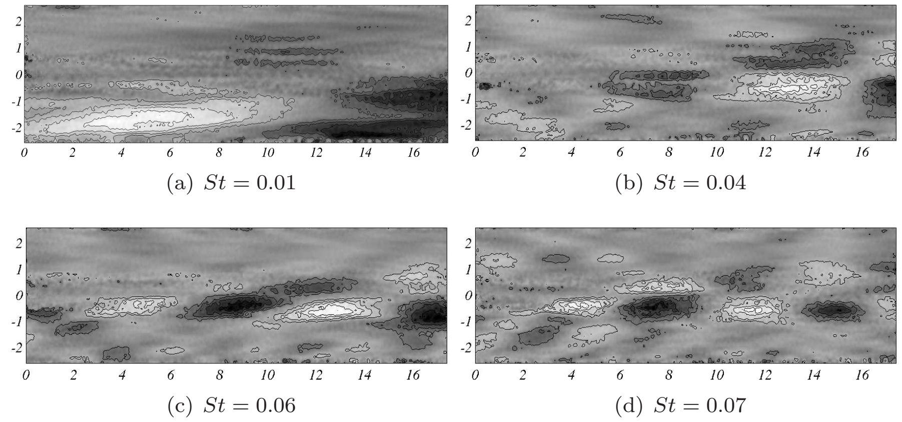

(a) $St = 0.01$ (b) $St = 0.04$

(c) $St = 0.06$ (d) $St = 0.07$

FIGURE 18. The streamwise component of four Koopman modes is shown. The associated Strohual number is reported in each label.

however the results from the spectral analysis have shown the presence of periodic features, arising from the flapping of the jet induced by a recirculation zone on the side of the inner jet.

Jet flapping appears as two large structures located downstream ($x/d > 10$) on the first two POD modes. These two modes appear to be coupled to each other, since they only differ from each other by a phase shift both in time (from the analysis of the *chrono*-modes) and in space. Frequency analysis of the *topo*-modes shows a clear peak at ($St = 0.02$), which is in line with previous experimental results. Modes 3, 4 and 5 show the coupling between the recirculation zone near the inlet and shear-layer oscillation, which is believed to be the leading sustaining mechanism for the jet flapping. Although the recirculation zone and the shear layer oscillations are characterized by different frequency, they appear coupled in the POD modes since the two structures are correlated. Instead, in the DMD modes the two structures appear in two separate modes; thus, the method efficiently isolates structures with a single frequency. The peaks found by spectral analysis of the *topo*-modes are in good agreement with the frequencies found by DMD.

DMD modes are selected with an iterative procedure that identify *consistent* modes by projecting the results of one iteration on the previous one obtained with another set of snapshots that have an offset origin in time, and retaining those whose projection is larger than a user defined threshold. We observed that the most consistent modes (*i.e.* those who *survive* increasing the threshold) are those whose growth rate is closer to 0; moreover, these modes are generally the ones characterized by high amplitude, in accordance with the theoretical results.

Gabriele Bellani and Fredrik Lundell thank the Swedish energy agency for fundings. Computer time was provided by SNIC (Swedish National Infrastructure for Computing). Prof. Hiroshi Higuchi is acknowledged for helping in the design and development of the experimental setup. Dr. Shervin Bagheri and Johan Malm are acknowledged for fruitful discussions.

References

Álamo, J. C. D. & Jiménez, J. 2009 Estimation of turbulent convection velocities and corrections to taylor's approximation. *J. Fluid Mech.* **640**, 5.

Arnoldi, W. E. 1951 The principle of minimized iterations in the solution of the matrix eigenvalue problem. *Quart. Appl. Math.* **9**, 17–29.

Aubry, N. 1991 On the hidden beauty of the Proper Orthogonal Decompositon. *Theoret. Comput. Fluid Dyn.* **2**, 339–352.

Bagheri, S. 2010 Analysis and control of transitional shear layers using global modes. PhD thesis, KTH Mechanics, Sweden.

Bagheri, S., Hœpffner, J., Schmid, P. J. & Henningson, D. S. 2009 Input-output analysis and control design applied to a linear model of spatially developing flows. *Appl. Mech. Rev.* **62** (2).

Chua, L. & Lua, A. 1998 Measurements of a confined jet. *Physics of fluids* **10**, 3137.

Davidson, M. 2001 Self-sustained oscillation of a submerged jet in a thin rectangular cavity. *Journal of Fluids and Structures* .

Goldschmidt, V. & Bradshaw, P. 1973 Flapping of a plane jet. *Physics of Fluids* **16**, 354–355.

Holmes, P., Lumley, J. & Berkooz, G. 1996 *Turbulence Coherent Structures, Dynamical Systems and Symmetry*. Cambridge University Press.

Hussain, F. 1986 Coherent structures and turbulence. *J. Fluid Mech.* **173**, 303–356.

Ilak, M. & Rowley, C. W. 2008 Modeling of transitional channel flow using balanced proper orthogonal decomposition. *Phys. Fluids* **20**, 034103.

Loève, M. 1978 *Probability theory II*, 4th edn., , vol. Graduate Texts in Mathematics. Springer Verlag.

Lumley, J. L. 1970 *Stochastic Tools in Turbulence*. Academic Press, New York.

Maurel, A., Ern, P., Zielinska, B. & Wesfreid, J. 1996 Experimental study of self-sustained oscillations in a confined jet. *Physical Review E* **54** (4), 3643–3651.

Mezić, I. 2005 Spectral properties of dynamical systems, model reduction and decompositions. *Nonlinear Dynamics* **41** (1), 309–325.

Noack, B., Schlegel, B., Ahlborn, B., Mutschke, G., Norzynski, M., Comte, P. & Tadmor, G. 2008 A finite-time thermodynamics formalism for unsteady flows. *J. Non-Equilib. Thermodyn.* **33**, 103–148.

Örlu, R., Segalini, A., Alfredsson, P. & Talamelli, A. 2008 On the passive control of the near-field of coaxial jets by means of vortex shedding. *Int. Conf. on Jets, Wakes and Separated Flows, ICJWSF-2008 September 16–19, 2008, Technical University of Berlin, Berlin, Germany* .

Rempfer, D. & Fasel, H. 1994 Evolution of three-dimensional coheren structures in a flat-plate boundary layer. *J. Fluid. Mech.* **260**, 351–375.

Rowley, C. W., Mezic, I., Bagheri, S., Schlatter, P. & Henningson, D. S. 2009 Spectral analysis of nonlinear flows. *J. Fluid Mech.* **641**, 115–127.

Ruhe, A. 1984 Rational Krylov sequence methods for eigenvalue computation. *Lin. Alg. Appl.* **58**, 391 – 405.

Saad, Y. 1980 Variations on Arnoldi's method for computing eigenelements of large unsymmetric matrices. *Lin. Alg. Appl.* **34**, 269–295.

Schmid, P. J. 2010 Dynamic Mode Decomposition. *J. Fluid Mech.* **656**, 5–28.

Schmid, P. J., Violato, D. & Scarano, F. 2010 Analysis of time-resolved tomographic PIV data of a transitional jet. *Bulletin of the APS* .

Sirovich, L. 1987 Turbulence and the dynamics of coherent structures i-iii. *Quart. Appl. Math.* **45**, 561–590.

Stanislas, M., Okamoto, K., Kähler, C. & Westerweel, J. 2008 Main results of the third international PIV challenge. *Experiments in Fluids* **45**, 27–71.

Willert, C. 2006 Assessment of camera models for use in planar velocimetry calibration. *Experiments in Fluids* **41**, 135–143.